STREAMER CHAMBER STUDY OF INTERMEDIATE-ENERGY NUCLEAR COLLISIONS WITH CCD CAMERAS

By

Silvana Patrizia Angius

A DISSERTATION

Submitted to
Michigan State University
in partial fulfillment of the requirements
for the degree of

DOCTOR OF PHILOSOPHY

Department of Physics and Astronomy

1987

ABSTRACT

STREAMER CHAMBER STUDY OF INTERMEDIATE-ENERGY NUCLEAR COLLISIONS WITH CCD CAMERAS

By

Silvana Patrizia Angius

A system of three charge-coupled device (CCD) cameras has been designed and built to record nuclear collisions in a streamer chamber.

This technical development significantly enhances the usefulness of streamer chambers as large solid angle (~4π sr) detectors for exclusive measurements in nuclear physics.

The system has been used in an experiment designed to study nearly-central collisions of Nb+Nb at 100 and 180 MeV/nucleon.

Computer codes have been developed that significantly reduce the amount of operator intervention in the data analysis.

π^- multiplicities are easily extracted by visually scanning the events. The values obtained are compared to the systematics found for different systems at higher energies.

Once magnetic rigidities and light intensities are extracted for each track in each event, the emitted fragments are identified by plotting the

rigidity,intensity point for each ion on a 2-dimensional (I vs. rig) plot.

One of the most interesting predictions of fluid-dynamical models and VUU calculations for heavy-ion collisions is the sideward emission of nuclear matter, due to the high compression created during the collision [Stö 80, Mol 85]. The transverse-momentum flow analysis introduced by Danielewicz and Odyniec [Dan 85] allows to calculate the amount of sideward momentum carried by the emitted fragments, while minimizing the distortions caused by finite-multiplicity effects.

This momentum flow analysis has been performed on our 180 MeV/nucleon data. The slope of the mean transverse momentum per nucleon vs. rapidity curve at mid-rapidity, or flow, was found to be 47.0±11.3 MeV/c/nucleon.

In order to compare our results to those obtained from other experiments, scale-invariant transverse momentum, $\tilde{p}^x$, and rapidity, $\tilde{y}$, have been introduced [Bal 84]. The $\tilde{p}^x$ vs. $\tilde{y}$ curve extracted from our data has been compared with the curves obtained for various systems in streamer chamber plus photographic film [Dan 85, Ren 84] and plastic ball experiments [Dos 85], and the shapes have been found to be very similar. The scale-invariant flow, $\tilde{F}$, for 180 MeV nucleon Nb+Nb is 0.16±0.04.

rigidity,intensity point for each ion on a 2-dimensional (I vs. rig) plot.

One of the most interesting predictions of fluid-dynamical models and VUU calculations for heavy-ion collisions is the sideward emission of nuclear matter, due to the high compression created during the collision [Stö 80, Mol 85]. The transverse-momentum flow analysis introduced by Danielewicz and Odyniec [Dan 85] allows to calculate the amount of sideward momentum carried by the emitted fragments, while minimizing the distortions caused by finite-multiplicity effects.

This momentum flow analysis has been performed on our 180 MeV/nucleon data. The slope of the mean transverse momentum per nucleon vs. rapidity curve at mid-rapidity, or flow, was found to be 47.0±11.3 MeV/c/nucleon.

In order to compare our results to those obtained from other experiments, scale-invariant transverse momentum, $\tilde{p}^x$, and rapidity, $\tilde{y}$, have been introduced [Bal 84]. The $\tilde{p}^x$ vs. $\tilde{y}$ curve extracted from our data has been compared with the curves obtained for various systems in streamer chamber plus photographic film [Dan 85, Ren 84] and plastic ball experiments [Dos 85], and the shapes have been found to be very similar. The scale-invariant flow, $\tilde{F}$, for 180 MeV/nucleon Nb+Nb is 0.16±0.04.

ACKNOWLEDGMENTS

I would like to thank my adviser, professor Gary Crawley, for giving me the opportunity to work on this project and for promptly reading the manuscript when time was pressing.

Among the members of my group, I especially wish to express my gratitude to prof. Robert Tickle for his help, encouragement, good humor, and unfailing optimism.

Richard Au and Ron Fox have provided essential contributions to the project, designing hardware, writing software, and cheerfully putting in long hours testing the system. I'd like to thank them for contributing their professional skills and for doing so in a friendly, good-humored way.

I wish to express my gratitude to prof. Laszlo Csernai for his help with the interpretation of the data and for his critical reading of the manuscript. He has provided much needed advice and direction. Thank you for caring.

The friendship and companionship of several of my fellow graduate students have made these years pleasant and have provided moral support. I especially wish to thank Kedarnath, for a friendship that has made even the Comprehensive exam tolerable (!); Marcia Torres, for being a pestiferous, warm, wonderful office-mate and friend; Anna Lampis, fellow

countrywoman and listening ear; and Dan Fox, for his friendship and his help during the experiment and with plotting routines.

Erich Ormand has supplied what long-distance help he could (thanks to BITNET and ATT, as well!).

A special thank you goes to Ms. Cesarina Belloni, who had confidence in a shy little girl, and let her know it.

Finally, many heartfelt thanks to my family. To my parents, for pushing, nagging, and encouraging. To my grandparents, for their unflinching love. To my sister, for believing in me no matter what.

TABLE OF CONTENTS

LIST OF TABLES

LIST OF FIGURES

Chapter One

INTRODUCTION

1.1 Review

The two main goals in the study of heavy-ion collisions in the range from intermediate to very high energies are the determination of the bulk properties of nuclear matter, or the nuclear equation of state, and the understanding of the collision processes, which may vary over the large range of energies available today. These two goals are related, and an improved insight into one can lead to a better understanding of the other.

Very little is known about the nuclear equation of state, beside its ground-state properties. It is well established that $E_c(\rho)$, the compressional energy, has a minimum for $\rho=\rho_0$ (normal nuclear density, ≈ 0.17 fm^{-3}), where it assumes a value of about -16 MeV (see figure 1.1.1). But the properties of nuclear matter at higher densities and high excitation energies are essentially unknown. Conjectures have been made about the possibility of exotic phases such as pion condensate, density isomer, and a quark-gluon plasma. At lower temperatures, $T<20$ MeV, and $\rho<\rho_0$, another critical phenomenon is predicted, namely a liquid-gas phase transition. This has been discussed both in terms of a fast mechanical instability [Ber 83] and a slower chemical instability [Cur 83]. Figure 1.1.2 shows a phase diagram of the various phenomena (exotic states and phase transitions) that have been predicted.

Knowledge of the properties of compressed or diluted nuclear matter is important to the understanding of diverse processes like the stability of neutron stars [Irv 81], the evolution of supernovae [Bet 79], and the

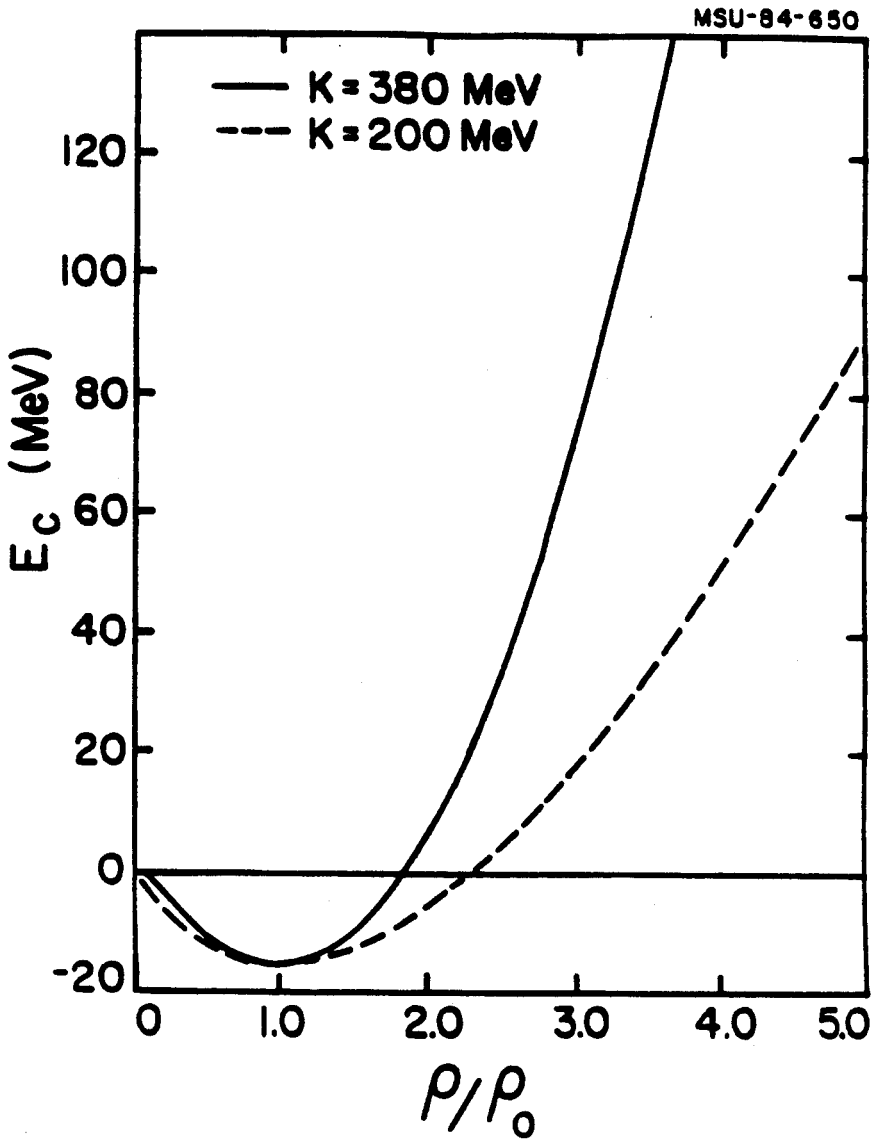

Figure 1.1.1 Nuclear equation of state for compressibility K=200 MeV and K=380 MeV (adapted from [Mol 85]).

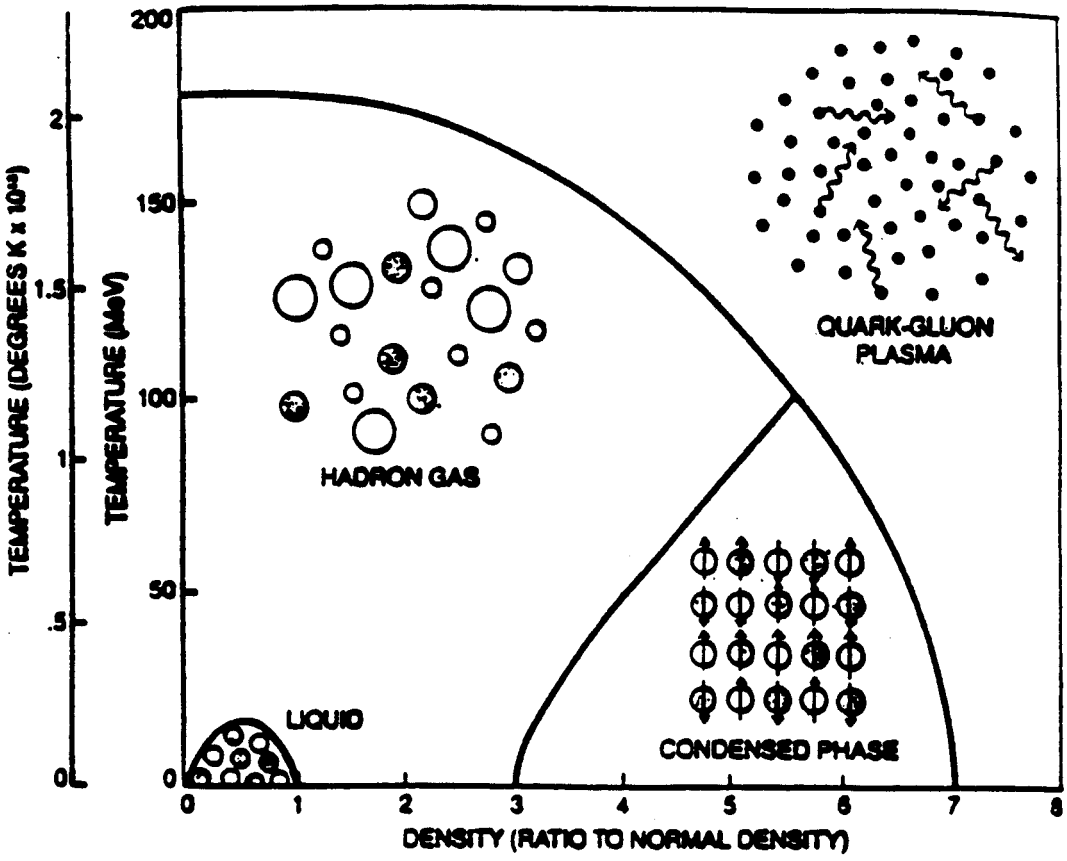

Figure 1.1.2 Phase diagram of nuclear matter. Various predicted exotic phases are shown (from [Mol 85]).

early stages of the universe, after the big bang and during the formation of stellar systems [Sch 81]. In these phenomena, nuclear densities ranging from 0.1 to 10 times ρ_0 are thought to occur, or have occurred. Unfortunately, these systems do not easily lend themselves to controlled experiments.

During the last ten years, an alternative way of producing and studying high-density, hot nuclear matter has become available with the development of heavy-ion accelerators. The process of a central, or nearly-central, collision between two energetic, heavy nuclei brings about the formation of a compressed and highly excited system, and a wide range of densities and temperatures are expected to occur. Naturally, these high densities are obtained for short lengths of time ($t \approx 10^{-22}$ sec), and global equilibrium cannot be reached [Mol 85]. Also, experimentally one does not measure the macroscopic variables directly related to the equation of state, such as density or compressibility. Rather, the momentum, mass, and charge of the individual particles emitted are measured. Furthermore, what is observed is only the final state of a reaction, i.e. the situation after the system has undergone compression, successive expansion, and has broken up into light fragments after freeze-out. If and how these fragments carry the information about the reaction dynamics and the characteristics of the short-lived dense nuclear system is a question which must be addressed if a comparison between theoretical models and experimental results is to be possible.

The progress made in the study of heavy-ion collisions at energies from ≈50 MeV/nucleon to a few GeV/nucleon has resulted from the interplay between theoretical interest in the properties of dense nuclear matter and the development of new accelerators and detectors. In the following

brief review, some of the results obtained in the last decade will be described, and an attempt will be made to show how the factors mentioned above (theoretical models and experimental results) have led to the need for more sophisticated experimental techniques.

Among the first experiments performed with heavy-ions are the measurements of single-particle inclusive spectra (e.g. Wes 76). One example of such double-differential cross sections, obtained for C+C at 50 MeV/nucleon, is shown in figure 1.1.3. One important feature, common to all these measurements, is that the high-energy tails of the spectra display an exponential slope characteristic of thermal emission. A 'temperature' of the emitting source is readily deduced from the slope of the energy distributions, and its velocity can be obtained from a fit of the spectra at different angles. Several models, from a simple geometrical description like the fireball model [Gos 77], to microscopic approaches such as the intra-nuclear cascade models [Cug 80,81,82], to a thermodynamical description [Stö 81], qualitatively explain various aspects of the data. But difficulties arise when one tries to verify the consequences of the different approaches, as will be described later. It is therefore apparent that inclusive measurements are not a satisfactory testing ground for the main differences between the various theories. The origin of this problem lies in the difficulty of separating the different reaction mechanisms in inclusive measurements. In other words, an integration over all impact parameters characterises inclusive data, and collisions at large impact parameters dominate the results.

If we are to study the response of dense nuclear matter, near-central collisions must be selected, where the collective phenomena are

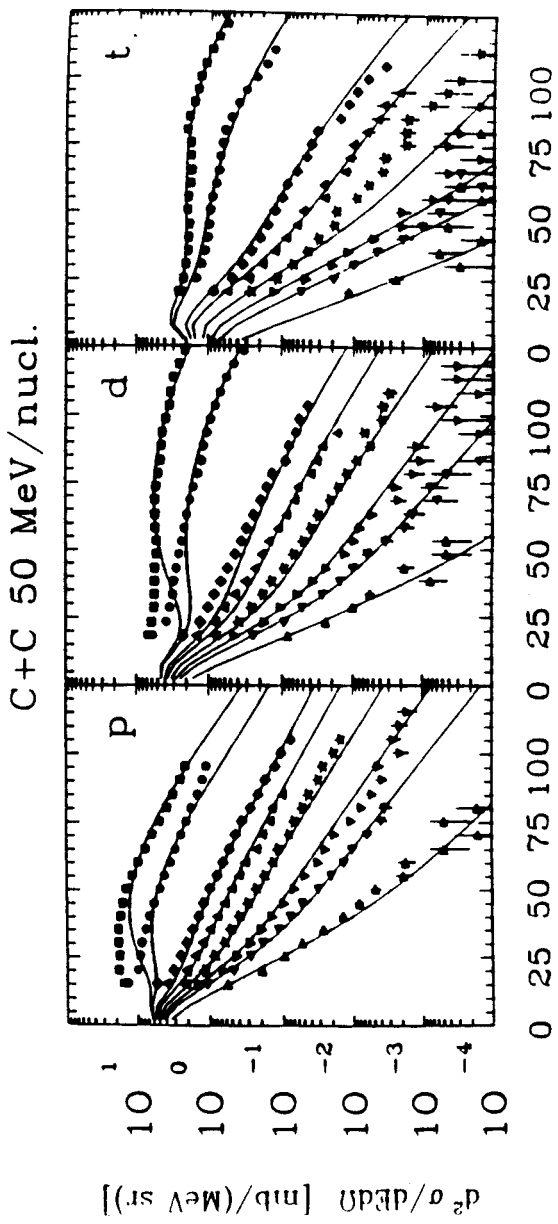

Figure 1.1.3 Single-particle spectra for the reaction C+C at 50 MeV/nucleon. The solid lines are obtained from a triple moving source fit (from [Fox 87]).

expected to take place. More exclusive measurements are therefore needed. Two-particle correlations are a step towards this objective.

Several interesting results have been obtained in experiments of this kind. To mention only a few, measures of large-angle correlations (see, e.g., Nag 79, Tan 80, Poc 85) have confirmed that inclusive measurements, where peripheral collisions dominate, are strongly influenced by quasi-elastic nucleon-nucleon scattering [Bab 85]. Temperature measurements based on the population of decaying excited states have given indications of values lower than those extracted from the slope of single-particle inclusive data [Poc 85]. An experiment measuring R, the ratio of in-plane to out-of-plane correlations, for a heavy system (Ar+Pb) shows that R varies from values <1 for $\theta<70°$, to $R>1$ at larger angles [Tan 80]. This behaviour cannot be explained in terms of quasi-elastic nucleon-nucleon scattering. Csernai et al. [Cse 81,82] have proposed an interpretation which takes into account the momentum distribution of the protons arising from collective. It appears that the measurements at intermediate angles, where $R<1$, correspond to high-energy protons, while the large-angle particles ($R>1$), have lower energy. This result is predicted by a hydrodynamic description of the collision, as is shown in figure 1.1.4. At large angles, it is likely that a proton emitted by the projectile will be detected in coincidence with a proton emitted by the target-like source (low energy, opposite side), while fast, projectile-like protons will be detected at smaller angles.

While these results have broadened our knowledge of the collision processes, there are still several deficiencies. For example, dynamic correlations between particles which are not detected can modify the correlation function [Bab 85]. In particular, Gyulassy has suggested that

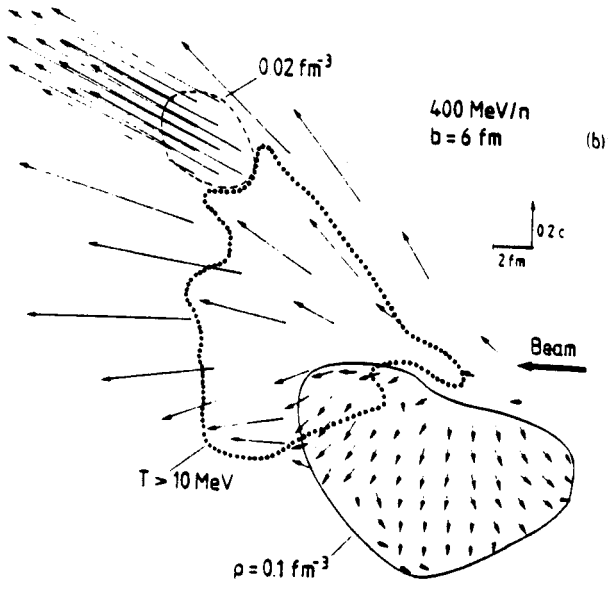

Figure 1.1.4 Density and temperature contours and velocity field (arrows) obtained for the reaction Ne+U at 400 MeV/nucleon from thermodynamical calculations (from [Sto 80]).

the existence of a reaction plane can cause a difference in the absorption of particles in and out of plane [Gyu 82]. To make the determination of the reaction plane possible, all or at least most of the emitted particles must be observed and identified. Detectors efficient over a large solid angle (usually referred to as 4π-detectors, because of their acceptance of nearly 4π sr) are necessary for this purpose.

1.2 Exclusive Measurements

In figure 1.2.1 the theoretical pictures of a Ne+U collision at 400 MeV/nucleon, as predicted by two different models, are shown. On the right, one can see the predictions of the intra-nuclear cascade model, a microscopic theory in which nuclear collisions are treated as a superposition of independent two-body nucleon-nucleon collisions in free space [Cug 85]. According to this picture, transparency effects dominate, and the emission of particles occurs preferentially in the direction of the beam. On the left, the predictions of hydrodynamic calculations are shown. This is a macroscopic theory, which refers directly to thermodynamical concepts. The equation of state serves as an input into the Navier-Stokes or Euler equations (see, e.g., Stö 82). In this model, compression effects give rise to a flux of particles in the direction perpendicular to the beam (side-splash) for central collisions (b=0), and to a bounce-off of projectile-like fragments away from the high-density region at larger impact parameters.

Ideally, exclusive measurements in 4π-detectors should give information equivalent to that obtained from these calculations. If A, Z, and $\vec{p}$ are known for all the emitted fragments, the reaction plane can be calculated and an analysis in terms of global variables (e.g. the

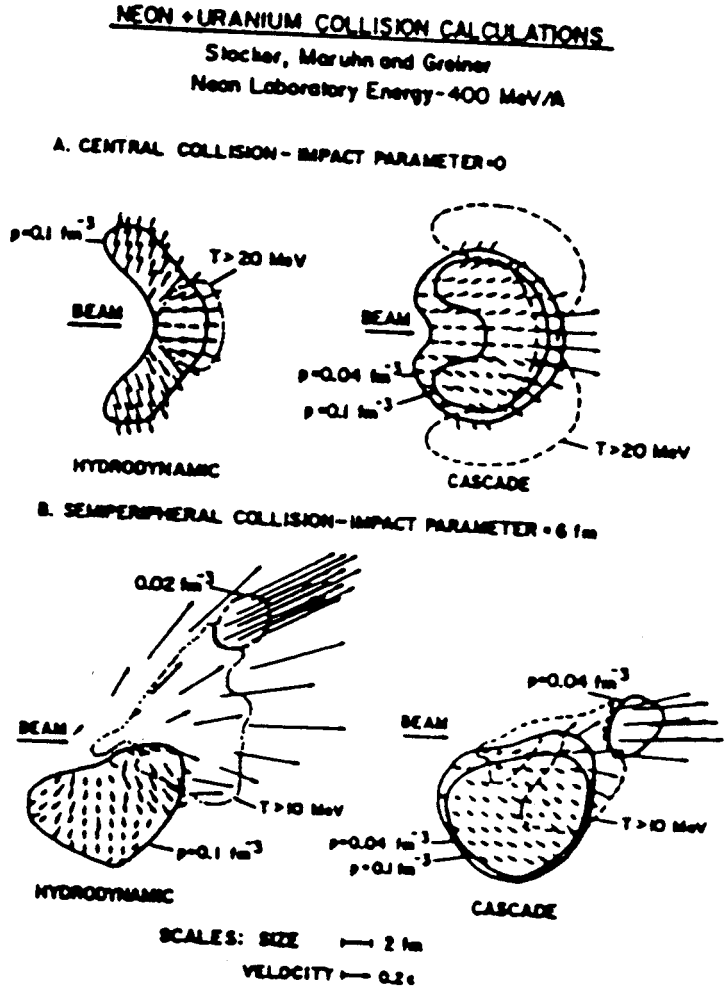

Figure 1.2.1 Predictions of the intranuclear cascade model and of hydrodynamics for central and peripheral collisions of Ne+U at 400 MeV/nucleon (from [Sto 80]).

sphericity tensor, defined in section B of this chapter) is possible. This allows the determination of quantities such as the mean flow angle and the shape of the momentum distribution. The two models mentioned above differ radically in the prediction of these variables.

Several types of detectors are available today, which come close to an acceptance of 4π sr, and with a granularity fine enough to make them well suited to the high- multiplicity events that must be studied. Electronic-type detectors, ranging from the Plastic Ball/Plastic Wall spectrometer [Bad 82] to time-projection chambers have been developed and used in heavy-ion measurements. Visual-type detectors such as streamer chambers and nuclear emulsions have been borrowed from high-energy physics and rather successfully employed in nuclear experiments. A new technical development, which will be described in this thesis, is the use of charge-coupled device (CCD) cameras with a streamer chamber. The introduction of solid-state image sensors in place of photographic film promises to alleviate two of the most problematic features in streamer chamber measurements, by expanding the dynamic range of the recording device and by making the data analysis largely automatic. More will be said about the characteristics of some of these detectors in chapter 2.2. Here, we will give a review of some of the experimental results obtained so far, and of the systematics that can be extracted.

A- π^- Multiplicity Measurements.

The final stage of a reaction is strongly influenced by chaotic thermal effects and by the expansion and break-up which follow compression. In an attempt to avoid these complications, Stöcker, Greiner, and Scheid have proposed to estimate the stiffness of the

nuclear equation of state from measurements of pion multiplicities [Sto 78]. This measure offers the advantages that i) the creation of pions occurs mostly during the compression phase, and ii) multiplicities are not strongly influenced by expansion and freeze-out.

A rather extensive investigation of the energy dependence of π^- multiplicity is described by Sandoval et al. [San 80]. In this study, performed at the LBL streamer chamber, central and peripheral collisions of ^{40}Ar on KCl, at energies between 0.4 and 1.8 GeV/nucleon, were analysed. In figure 1.2.2a the mean π^- multiplicities are shown as a function of bombarding energy in the center of mass. The predictions of a cascade calculation, which lacks compressional effects, does not reproduce the data well. In figure 1.2.2b the compressional energy per nucleon, estimated from figure 1.2.2a by taking the difference between the energy obtained from cascade calculations and the experimental energy for the same multiplicity, is plotted as a function of the relative nuclear density. The equation of state plotted in figure 1.2.2b corresponds to a compressibility of 250 MeV.

B- Collective Flow Measurements: Sphericity-Tensor Analysis.

The sphericity tensor is defined as:

$$T_{ij} = \sum_{\nu} \omega_\nu p_i(\nu)\, p_j(\nu)$$

where p_i and p_j are two components of the momentum (p_x, p_y, p_z) for the particle ν in a given event, and ω_ν is a weight factor associated with each particle. If this tensor is diagonalized, the three eigenvectors have magnitude f_1, f_2, f_3 and their orientation is characterized by the

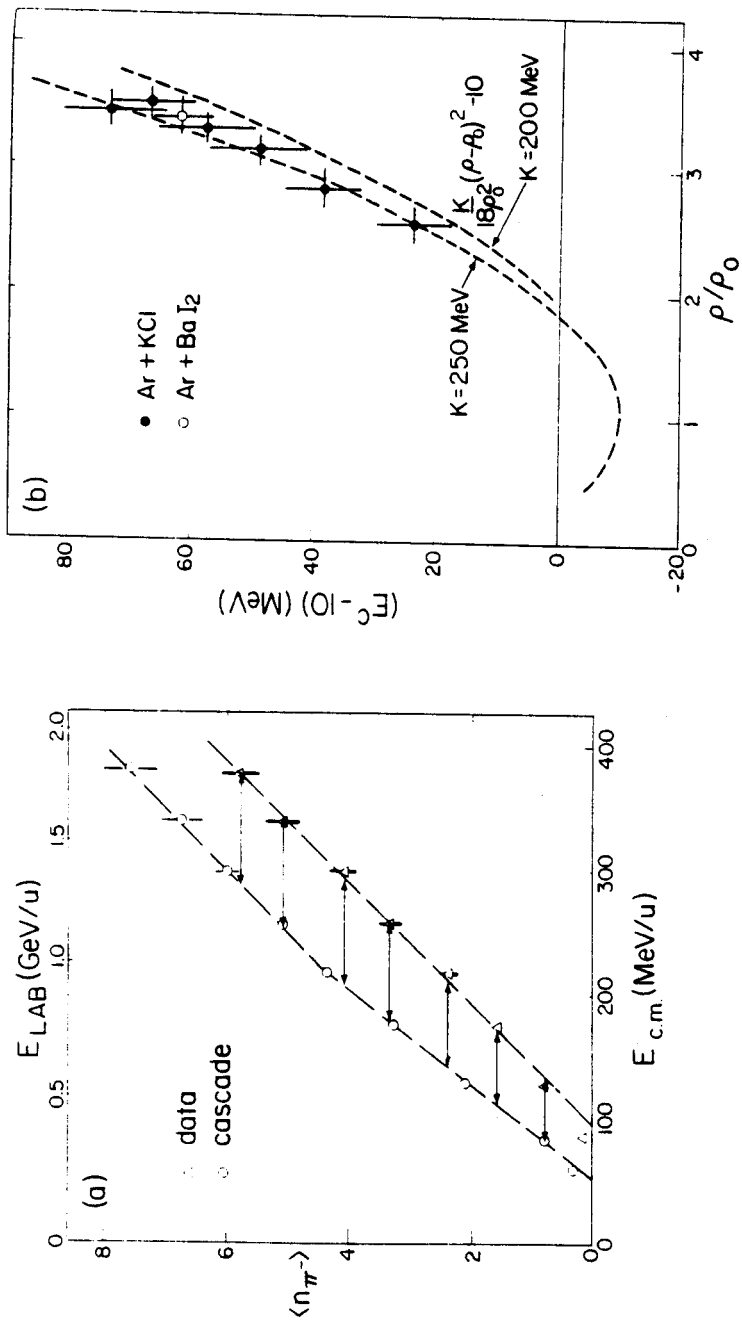

Figure 1.2.2 a) π^- multiplicities from Ar+KCl collisions at different energies. The circles are the results of cascade calculations. The horizontal arrows give the value of the compressional energy. b) E_c vs. relative density for the experimental points in a) and for the nuclear equation of state with K=250 and K=200 MeV (from [Sto 82]).

Euler angles θ, ϕ, ψ.

With this procedure, the distribution of the momenta within an event is represented by an ellipsoid of semi-axes f_1, f_2, and f_3, and rotated by θ, ϕ, ψ. Thus, the shape of the momentum distribution can be evaluated and compared with the predictions of different theoretical models. A particularly interesting parameter is θ, the mean flow angle, which measures the collective sideward flow.

In determining this quantity experimentally, large distortions due to finite-multiplicity effects are introduced. Danielewicz and Gyulassy have shown that these distortions are mostly contained in the Jacobian of the transformation which relates the six parameters f_1, f_2, f_3, θ, ϕ, ψ, to the six independent elements T_{xx}, T_{yy}, T_{zz}, T_{xy}, T_{xz} [Dan 83]. Therefore, when the flow angle distribution is studied, $\frac{dN(\theta)}{d\theta}$ must be corrected by the proper Jacobian. This introduces a term $\frac{1}{\sin\theta}$, and the corrected distribution is:

$$\frac{1}{\sin\theta}\,\frac{dN(\theta)}{d\theta} = \frac{dN(\theta)}{d(\cos\theta)}$$

where N is the number of events which give a flow angle of θ, after diagonalising the tensor T_{ij}.

The flow angle distributions allow an interesting comparison between the cascade model, which predicts a peak at 0 degrees for all impact parameters, and hydrodynamics or VUU calculations, which predict a non-zero flow angle varying with impact parameter, mass of the system, and incident energy.

Several experiments have been performed to study the flow angle distributions for various systems at different energies using the Plastic

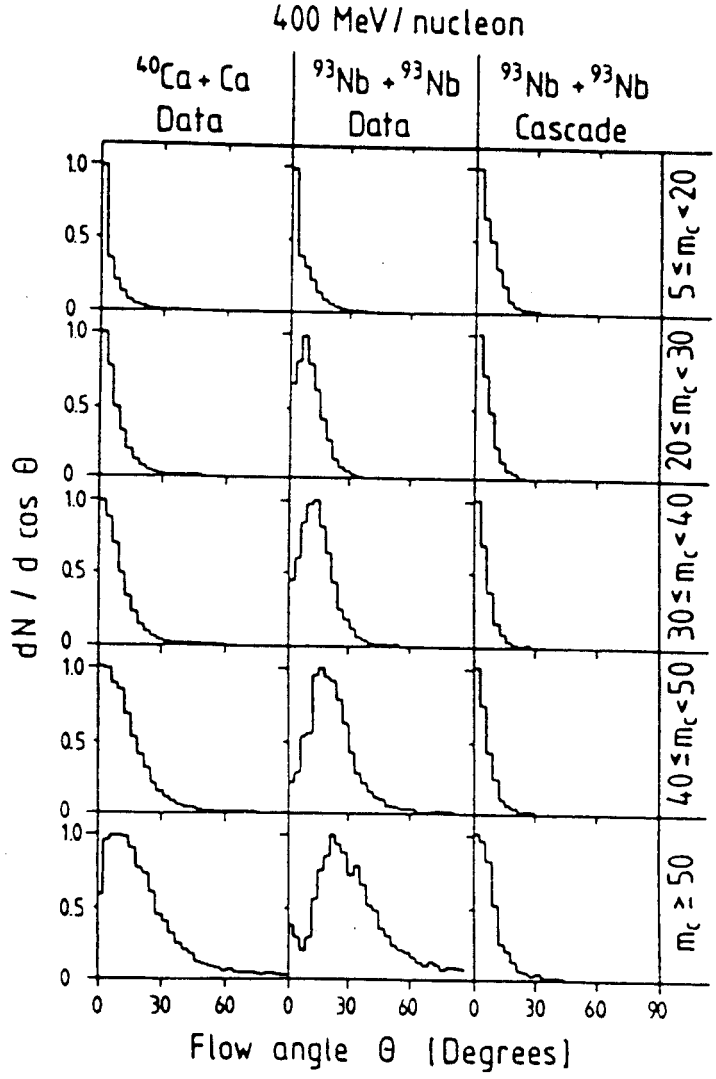

Figure 1.2.3 Experimental flow angle distributions for Ca+Ca and Nb+Nb and predictions obtained from the cascade model (from [Gus 84]).

Ball spectrometer [Gus 84, Rit 85]. In figure 1.2.3 the data obtained for 400 MeV/nucleon Ca+Ca and Nb+Nb are compared with cascade calculations. The experimental distributions clearly show a sideward flow, especially for the heavier system, which the cascade model is unable to reproduce. The predictions of the hydrodynamical model for different impact parameters are shown in figure 1.2.4, where the experimental data for the appropriate multiplicity cuts are also plotted. Although the agreement is not perfect, it is clear that the model reasonably predicts the experimental distributions and their variations with multiplicity.

An asymmetric system was studied by Renfordt et al. using a 0.772 GeV/nucleon Ar beam on Pb at the LBL streamer chamber [Ren 84]. They find a well defined flow angle in semi-central collisions ($3 \leq b \leq 5.5$ fm), but a spherical shape in nearly central collisions. This different behaviour, due to the non-symmetry of the system, is also qualitatively predicted by the hydrodynamical model.

C- Collective Flow Measurements: Transverse Momentum Analysis

The results reviewed above show that the direction of flow and the beam axis define a privileged reaction plane. If an evaluation of this plane is possible experimentally, then one can study the distribution of the projected momentum, rather than simply the flow angle.

The main problem with the sphericity analysis is its sensitivity to statistical fluctuations. Danielewicz and Odyniec have suggested a different approach which helps eliminate finite-multiplicity distortions from the evaluation of the reaction plane, and which has proved a more sensitive and powerful tool in revealing collective-flow effects [Dan 85]. In brief (the details will be given in chapter 4), the method

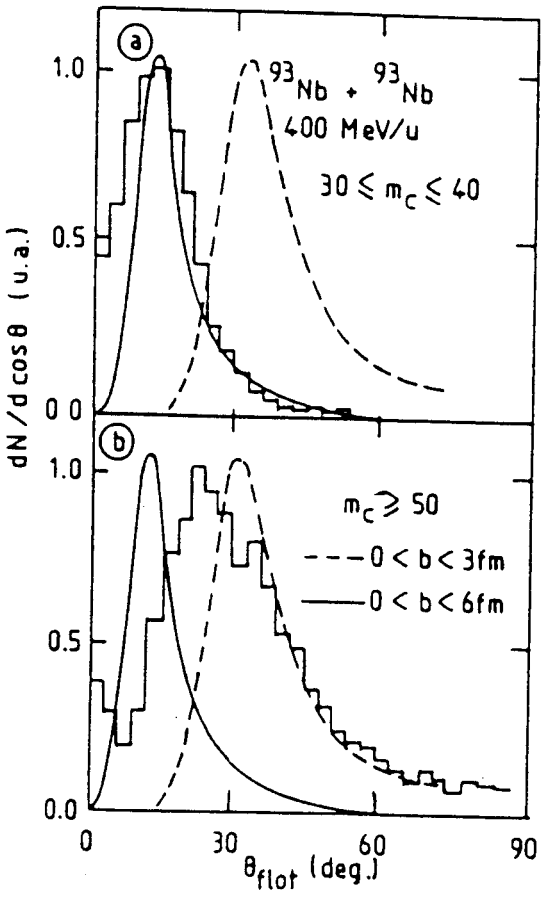

Figure 1.2.4 Experimental flow angle distributions for two different multiplicity cuts (histograms) are compared with hydrodynamical calculations for different impact parameters (from [Buc 84]).

consists of estimating the reaction plane from the transverse momenta of the emitted particles, and then rotating each event to its reaction plane. The distribution of the average transverse momenta of the emitted particles as a function of rapidity is then studied for evidence of collective effects.

In the paper mentioned above, Danielewicz and Odyniec have applied their analysis to the data obtained in an experiment performed at the LBL streamer chamber for the Ar+KCl reaction at 1.8 GeV/nucleon. The same experiment had been previously analysed with the sphericity tensor method, and no conclusive evidence had been found of collective flow [Str 83]. With the transverse momentum analysis a substantial total momentum transfer was found, as can be seen from the data shown in figure 1.2.5).

The same system was studied by another group [Kea 86], again at the LBL streamer chamber. A comparison of their experimental transverse momentum distribution with the predictions of VUU calculations seems to point towards a "medium" to "stiff" equation of state, with compressibility values between 200 and 300 MeV.

Doss et al. have studied the dependence of collective flow on beam energy, multiplicity, and mass of the system in a series of measurements performed at the Bevalac with the Plastic Ball detector [Dos 86]. Ca+Ca, Nb+Nb, and Au+Au collisions were studied at energies between 150 and 1000 MeV/nucleon. To minimize the effects of the detector bias on the quantitative measure of flow, they calculate the slope of the transverse momentum distribution at mid-rapidity, which they call "flow". In figure 1.2.6a and b a summary of their results is shown. As predicted by hydrodynamic calculations, and observed in previous experiments [Rit 85], the flow increases with the mass of the system. Both the multiplicity

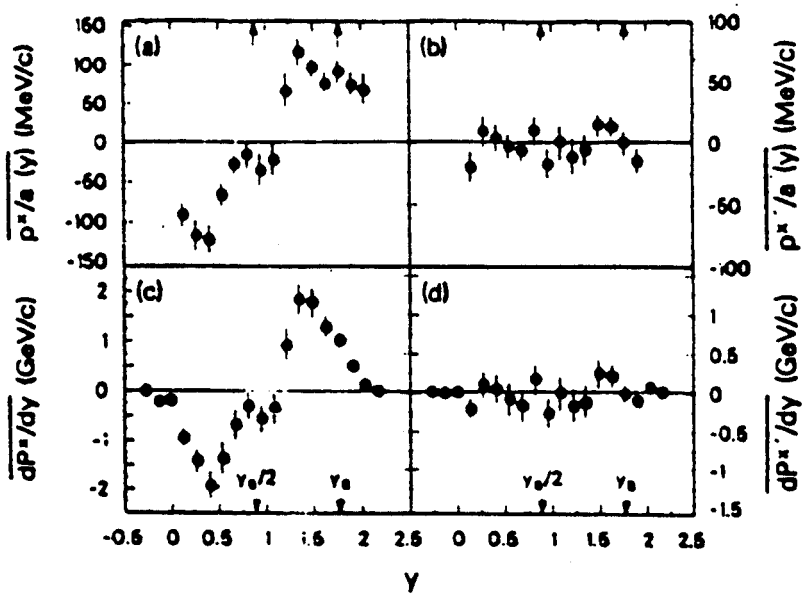

Figure 1.2.5 a,b) Average transverse momentum per nucleon for data (a) and Monte Carlo calculations (b) for Ar+KCl at 1.8 GeV/nucleon. c,d) Differential transverse momentum deposition per unit rapidity for data (c), and Monte Carlo calculations (d) (from [Dan 85]).

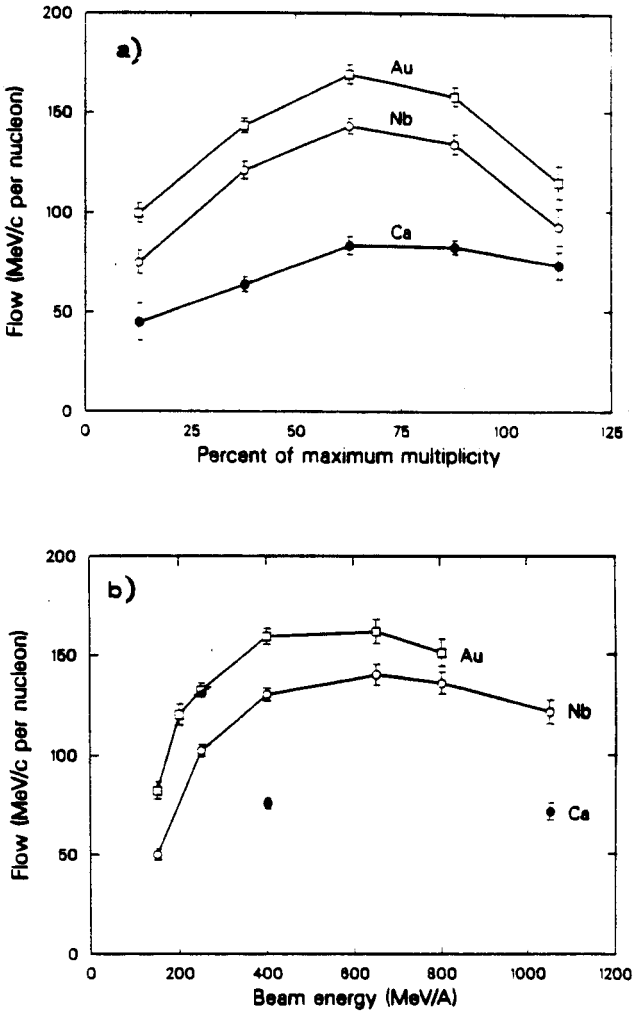

Figure 1.2.6 a) Flow as a function of multiplicity for Au+Au, Nb+Nb, and Ca+Ca at 400 MeV/nucleon. b) Flow as a function of beam energy (from [Dos 86]).

dependence and the energy dependence of the "flow" are different from the behaviour of the flow angles shown in figure 1.2.3. The first distribution (figure 1.2.6a) shows a maximum at intermediate multiplicities, and the energy dependence shows a rise in flow up to about 650 MeV/nucleon, then a slight fall-off. These effects might be partially due to the detector response, which depends on energy and multiplicity.

The last experiment to be briefly described here, chiefly because it involves yet another type of detector, is a series of emulsion measurements with Au and Xe beams, at energies from 0.5 to 1.2 MeV/nucleon [Cse 86]. The energy of the projectile is determined from its range in the emulsion, the charge of $Z \geq 2$ particles is obtained from ionization measurements, and A is assumed to be = 2Z. The only other measured quantity is the azimuthal angle of the fragments. Therefore, a quantity called pseudo-transverse momentum, defined as

$$P_{\mu}^{t} = \tan \theta_{\mu} \, P_{\parallel}$$

is introduced. Here, $P_{\parallel}$ is the longitudinal momentum per nucleon of the beam. The distribution of mean pseudo-P^t per nucleon projected onto the reaction plane, P^x/A, vs. P^t shows a significant collective flow, and the values extracted are consistent with those obtained in other experiments.

A way of comparing the results obtained for different systems at different energies is suggested by Balazs et al. [Bal 84]. This method consists of expressing the data in terms of quantities which, in the

hydrodynamic model, are scale-invariant. Any deviation from this scale-invariant behaviour indicates the possibility of processes causing non-perfect flow, such as dissipation and phase transitions. Bonasera and Csernai apply this method to a variety of experimental data [Bon 86]. In their work, they define a scale-invariant transverse momentum and rapidity:

$$\tilde{p}^x = p^x / p^{CM}_{proj}$$

$$\tilde{y} = y^{CM} / y^{CM}_{proj}$$

where p^x and y^{CM} are the transverse momentum and rapidity obtained from the data, and p^{CM}_{proj} and y^{CM}_{proj} are the momentum and rapidity per nucleon of the projectile in the center of mass. The $\tilde{p}^x$ distributions thus obtained are shown in figure 1.2.7. The behaviour of the various curves in this scale-invariant plot is remarkably constant over the wide range of energies and masses shown. In addition, a scale-invariant flow, $\tilde{F}$, is defined as the slope of the experimental $\tilde{p}^x$ distributions at mid-rapidity (the 'flow', as introduced by Doss et al. in Dos 86) divided by the momentum of the beam in the center of mass. This experimental quantity can be compared with the behaviour of Re, the Reynolds number, which characterises viscous flow patterns: Similar patterns have the same Reynolds number (see Bal 84 and Bon 87 for a detailed description).

In figure 1.2.8 the curves of constant $\tilde{F}$ in the A, E_{CM} plane are compared with the Re=constant lines. The most striking difference appears at low energies, for $E_{CM} \leq 60$ MeV/nucleon, indicating a drastic change

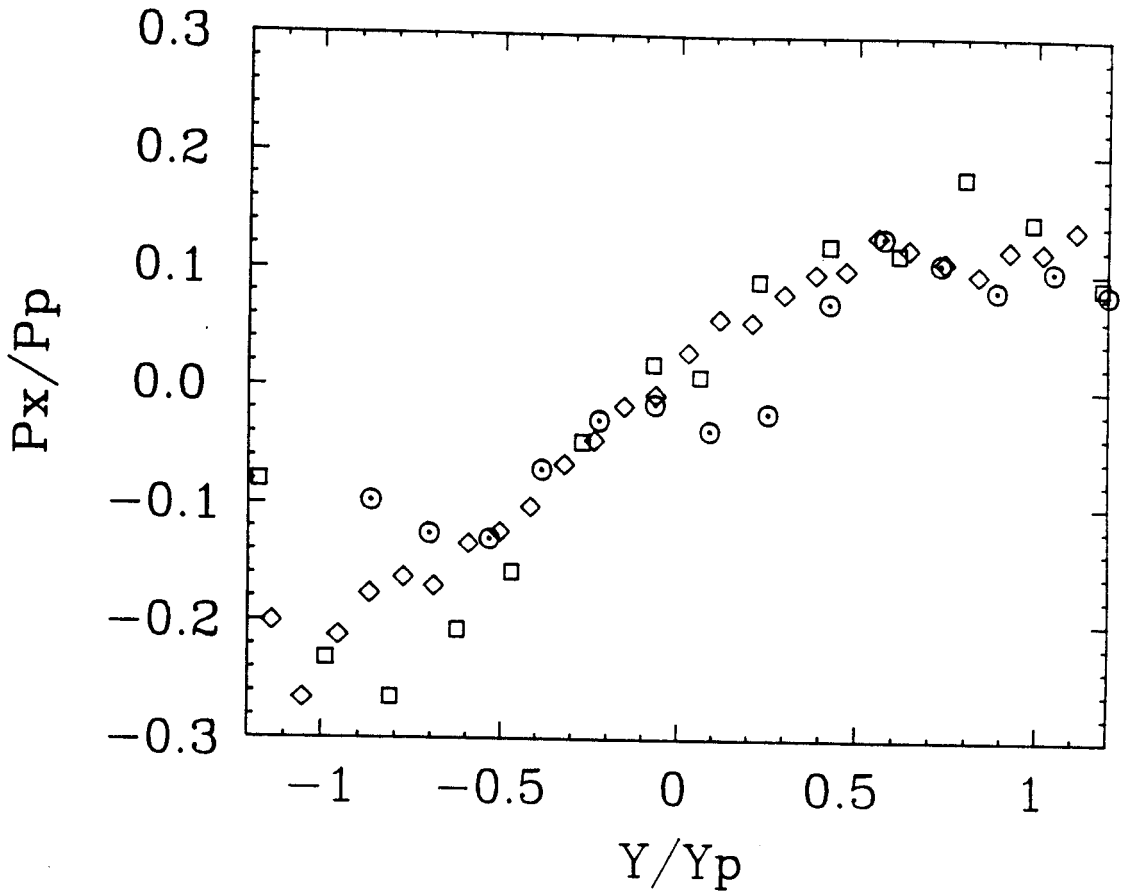

Figure 1.2.7 Scale-invariant transverse momentum distribution for: circle, Ar+KCl at 1.8 GeV/nucleon; diamond, La+La at 0.8 GeV/nucleon; square, Nb+Nb at 400 MeV/nucleon. From [Bon 86].

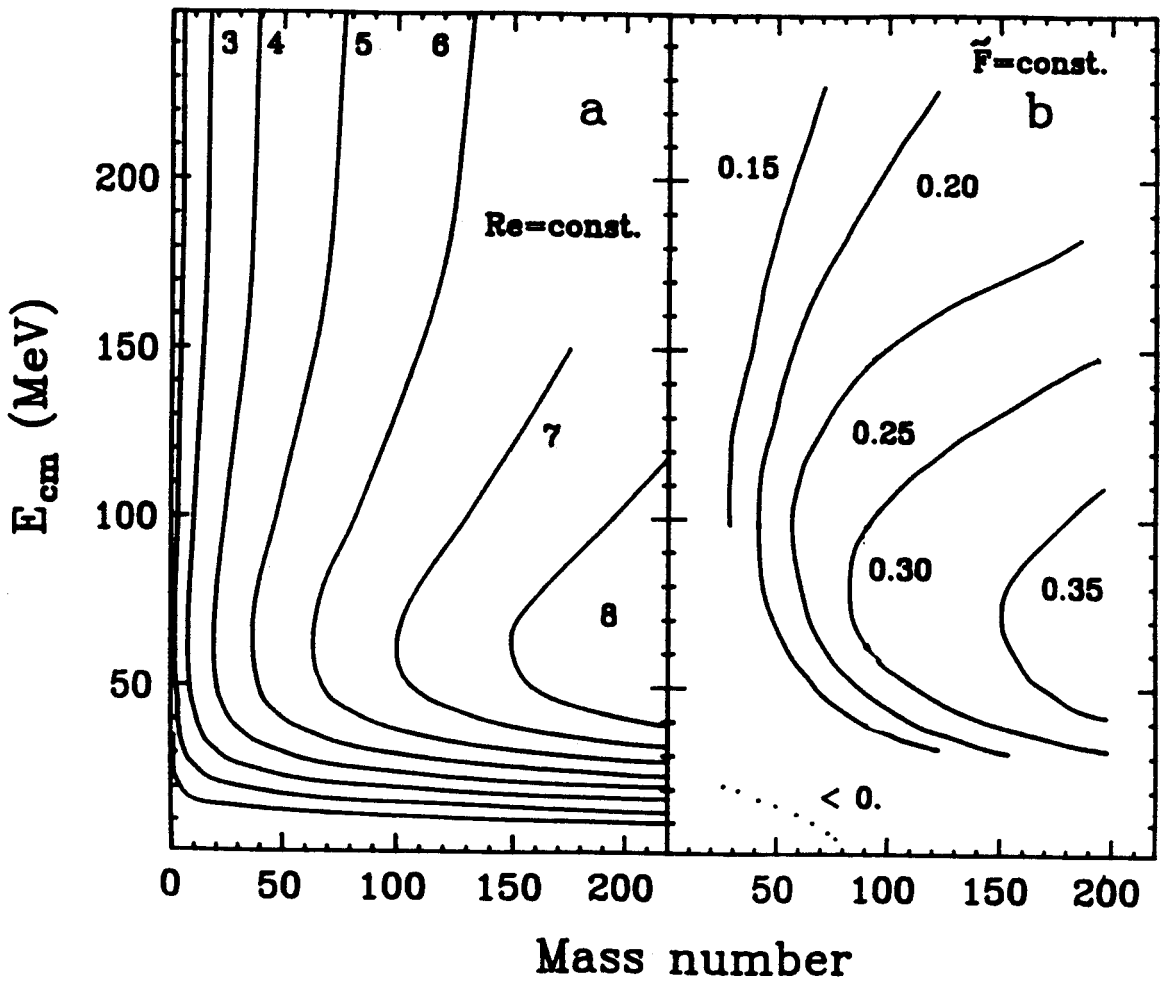

Figure 1.2.8 Contour lines of Re=constant and $\tilde{F}$=constant in the A,E_{cm} plane (from [Bon 86]).

either in the equation of state (e.g. a phase transition), or in the reaction mechanism. It is interesting to observe that in this energy range the Vlasov-Uehling-Uhlenbech (VUU) model predicts a change in slope in the transverse momentum distribution, as shown in figure 1.2.9 [Mol 85]. Some experimental evidence for 'negative' emission angles has been found in neutron emission studies for the N+Ho reaction at 25 MeV/nucleon [Dea 87], and from measurements of the circular polarization of coincident Y-rays emitted from the residual nucleus in the N+Sm reaction at 20 and 35 MeV/nucleon [Tsa 86]. This effect is due to the attractive nuclear force which, at these lower densities, overcomes the repulsive interaction due to pressure build-up. In this respect, the region of interest in figure 1.2.8 is that at low energies.

The work presented in this thesis describes the development of a three-CCD-camera system, which is very well suited for the investigation of heavy-ion collisions in the low-energy region of figure 1.2.8, where the charged-particle multiplicities do not exceed 50 or 60. This system was used in an experiment at the LBL streamer chamber to investigate nearly-central collisions of Nb on Nb at 100 and 180 MeV/nucleon.

Chapter 2 describes the principles of operation of a streamer chamber and compares it with other types of 4π-detectors. The CCD system is then discussed, and its characteristics compared with that of photographic film. Finally, there is a description of the electronics set-up and the software developed to run the system during data acquisition.

In chapter 3 the details of the data analysis will be given, with a discussion of the uncertainties in the results.

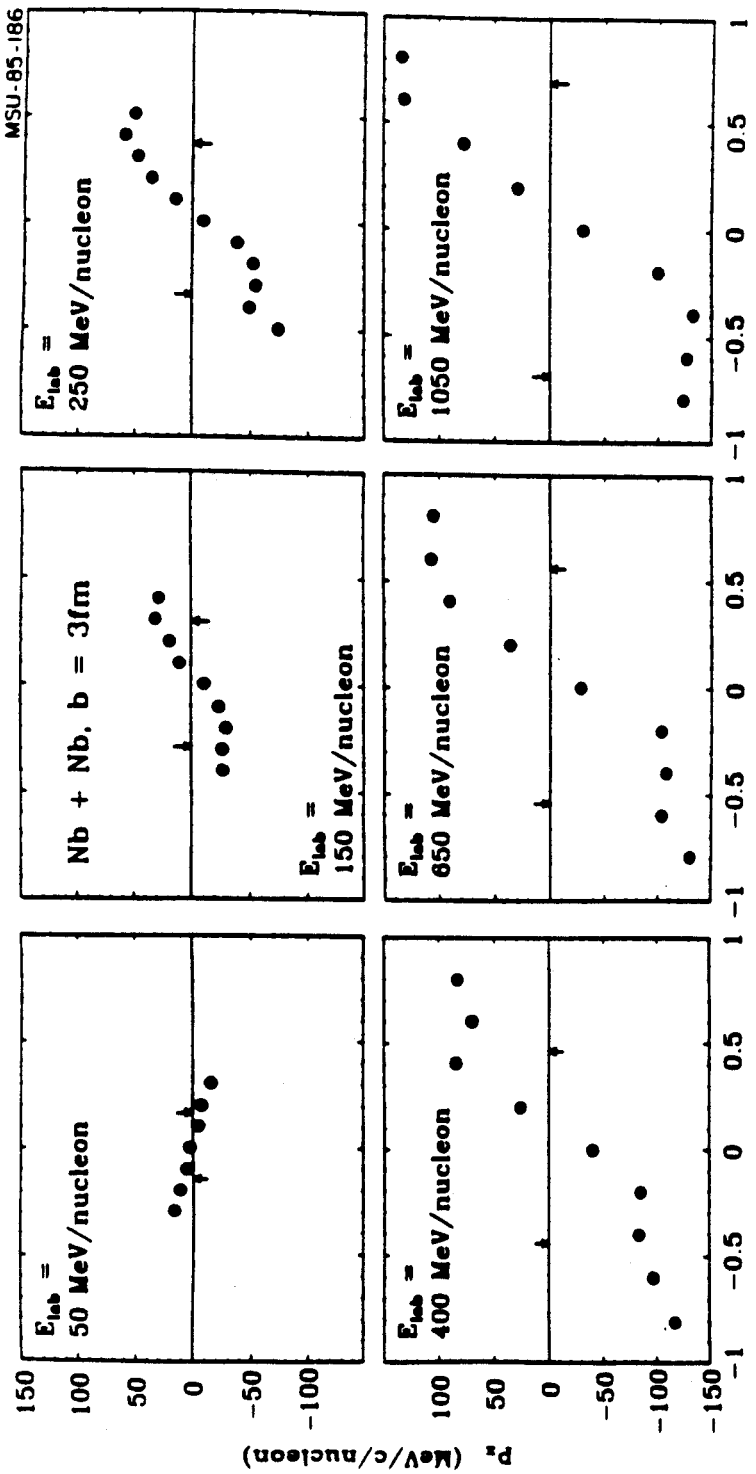

Figure 1.2.9 VUU model predictions of the transverse momentum per nucleon for Nb+Nb at different energies, for b=3 fm (from [Mol 85]).

The physical results extracted from the experiment will be presented in chapter 4, with a description of the calculations and models (transverse-momentum analysis, scaling behaviour of physical observables) used.

A summary of the results, with an evaluation of the performance of the system is contained in chapter 5. Possible future improvements will be discussed as well. Lastly, some ideas for future experiments will be mentioned.

Chapter Two

SYSTEM DEVELOPMENT AND DESCRIPTION

2.1 Principles of Operation of the Streamer Chamber

When a charged nuclear particle moves through a gas, it undergoes a series of inelastic Coulomb collisions with the electrons in the gas, ionizing or exciting the atoms to which it comes sufficiently close. In the process of radiative recombination or de-excitation which follows, photons are emitted. As a consequence, if the photons are of the appropriate wave-length, the trajectory of the particle through the gas can be displayed. In the case of the streamer chamber, the gas used is mostly neon. The transitions from the $2p_1$-$2p_{10}$ levels to the $2s_2$-$2s_5$ levels cause emission of light in the visible part of the spectrum, giving the neon discharge its characteristic red color [Ric 74].

Naturally, for the recording of such an image to be possible, there must be a sufficiently large number of photons to be detected by a light-sensitive device. Therefore, before the primary electrons and ions diffuse away from the initial track, an intense electric pulse is applied, which causes the electrons to accelerate toward the anode. The time delay between the occurrence of an event and the application of the high-voltage pulse should be a few microseconds, and the memory time of the gas should be made to match this value approximately. By adding a few parts per million of an electronegative gas, such as SF_6, the rather long recombination time of neon is reduced to the proper value. After being accelerated, the electrons are likely to gain sufficient energy to cause further ionization when they collide with a gas atom. More electrons are thus liberated which, after acceleration, will in turn ionize too. As

this process continues, an avalanche quickly builds up. This process grows exponentially, and can be described by

$$n = e^{\alpha x} \qquad (2.1)$$

where n is the number of electrons produced by one electron in a length x, and α is the Townsend first ionization coefficient, defined as the number of electrons produced in the path of a single electron travelling 1 cm [Ric 74].

As the number of electrons in the avalanche grows, space-charge effects become more important, gradually reducing the applied field within the avalanche, but enhancing it at the head. In the absence of the electric field, recombination occurs within the avalanche, causing the emission of ultraviolet photons. Those photons that are liberated near the head or tail of the avalanche, where the electric field is very high, can give rise to secondary avalanches, and these in turn can repeat the process, always along the direction of the applied field. The process by which the new and old avalanches merge together is called streamer formation.

A side view of the streamers produced along the path of an ionizing particle is shown in figure 2.1.1a. Here, by limiting the duration of the electric pulse, the streamer growth has been arrested, but the trajectory of the ion is not well defined. Figure 2.1.1b shows how an end view (along the direction of the electric field) of the streamers offers a well defined track, and also makes photography easier, the dots (projections of the streamers) being brighter. At the LBL streamer

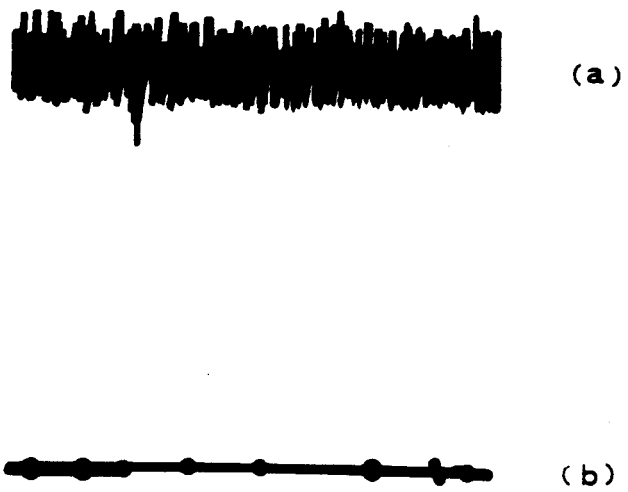

Figure 2.1.1 a) Side view of the streamers produced along the path of an ionizing particle. b) End view (along the direction of $\vec{E}$) of the streamers.

chamber, the size of the ribbon seen along the perpendicular to the field is about 1 cm, and about 1 mm when seen in profile.

As we have mentioned, the light recorded in the streamer chamber is produced not only by the electrons directly liberated by collisions of the particle with the gas atoms (primary ionization), but also by those ejected by successive collisions with the accelerated primary (and secondary) electrons. A measure of either the primary or the total ionization (which is what is observed in the streamer regime) can give information on the specific energy loss of the particle, dE/dx, and, therefore, on its velocity and charge. A number of properties of the observed tracks depend on the ionization, among them the number of streamers per unit length and the streamer brightness. But, while the primary ionization indicates the actual number of collisions that have occurred, and is therefore directly proportional to the energy loss of the particle, by the time streamers develop, this proportionality is to some extent lost. This is the price one has to pay for brightness. One possible advantage of using the more sensitive CCD's instead of film is that a decreased light output is acceptable, and the chamber can be operated at a slightly lower voltage. In this regime, closer to the avalanche mode, the proportionality between track brightness and dE/dx (or Z^2) should be to some extent retained, and the particle identification capability of the chamber improved. This point will be further discussed in chapter 3.

Another advantage of operating at a lower voltage is the reduction of flares. This phenomenon, visible in many events as very bright areas which obscure the tracks, is caused by energetic δ-rays emitted in the

direction of the electric field, shorting the electrodes and producing extremely bright sparks.

2.2 The Streamer Chamber in Heavy-Ion Physics

The ideal detector for heavy-ion experiments should meet a number of requirements suggested by the nature of the reaction processes to be observed. In this section, these requirements will be discussed and the streamer chamber performance compared with that of other detectors currently in use or in construction.

The first characteristic of a detector for exclusive measurements is that of a nearly 4π solid angle. The response of the streamer chamber is isotropic over almost the entire space, with the exception of a small cone of about $\pm$ 20° along the direction of the electric field. In this region, the streamers fuse with each other, forming a continuous channel up to a thousand times brighter than the normal tracks, and the tracks themselves appear as very short, bright stubs. This bias can be estimated, however, by observing the particles emitted in the corresponding cone, at a 90° angle with the E-field.

Due to the high multiplicities observed in heavy-ion collisions, a good multitrack efficiency and two-track resolution are necessary. Events with up to 150 charged particles have been observed at the LBL streamer chamber [Van 82]. An estimate of the two-track resolution must take into account the characteristics of the recording device (CCD or photographic film), and will therefore be discussed in detail in section 3 of this chapter. For the moment, it will suffice to mention that, due to the chamber's fine granularity, its ability to separate adjacent tracks is better than that of any electronic-type detector.

Another important requirement is the triggerability of the device, so that particular kinds of events can be selected during the measurement. The memory time of the chamber, of about 2 μsec, is long enough for a set of plastic scintillators, or other electronic detectors, to establish that an event of interest has occurred and to trigger the high-voltage pulse in the chamber.

In addition, one must keep in mind that fragments over a wide range of masses and momenta, corresponding to a wide range of primary ionization, can be produced in heavy-ion collisions. Ideally, all these fragments should be identified (Z and A determination) and their momenta measured. The first limitation, which prevents the detection of all the fragments emitted in the streamer chamber, is the necessity for a particle to travel at least 8-10 cm in the gas to be observed, since the density of tracks is usually very high near the interaction vertex. Including energy losses in the target material and in the gas, for a 220 mg/cm^2 Nb target, and assuming that the particles are produced at the front surface of the target, the minimum energy for protons and α-particles to be observed is about 9 MeV/nucleon. For the particles that are seen, the curvature of the trajectory in the magnetic field of the chamber allows the determination of the ion's magnetic rigidity (momentum divided by the charge, p/Z). Therefore, the identification of the charge is necessary to derive momenta and, hence, energies, rapidities, and other physical variables of interest.

The problem of the identification of such a wide range of fragments, with different charges and energies, has been approached in different ways. The plastic ball [Bad 82] has been used to detect and identify relatively light ions (up to α-particles), while the 4π array, under

construction at NSCL [Wes 85], promises to provide good position, charge, and time resolution for particles over a wide range of charges. Data obtained at the LBL streamer chamber, with film as a recording medium, have been analysed using the integrated intensity per unit length along the tracks to provide a good separation between p, d, t, and ^{4}He in a limited range of rigidities [Wol 81]. Limitations in the performance of photographic film, which will be discussed in detail in section 2.3, prevent the identification of higher-charge fragments. It is hoped that the introduction of CCD cameras as a recording device will help overcome these limitations, once the problems encountered during the experiment and in the analysis described in this thesis are solved.

Of the shortcomings of the streamer chamber, as opposed to electronic-type detectors, one is the slow event rate imposed by the pulsed high-voltage supply (a Marx generator), and, in the case of CCD cameras, by the data-reduction and read-out time of the electronics and the computer. The rate obtained with the system described in this work was one event per Bevalac spill. At this rate, over 1000 good events (clean central collisions) were collected at each beam energy during the allotted time. The relatively slow analysis is another often-mentioned problem with this type of experiments. The introduction of CCD's has improved the speed of the analysis, even though the extent of the improvement depends strongly on the multiplicity of the events. This point, too, will be discussed in more detail in section 3.2.

2.3 Charge-coupled Devices

Charge-coupled devices (CCD's) have been used in optical astronomy for some years, and "have opened new horizons" in the field [Djo 84]. To

mention only one of their most recent applications, they have been used for imaging fast variations in the coma and tail of Comet Halley [Bau 86].

The introduction of CCD cameras in nuclear physics is a more recent development, and the system described in this work is the first of its kind ever to be developed and used as a recording device in an experiment. The substitution of CCD's for photographic film to record events in a streamer chamber represents a significant improvement in the processes of data acquisition and analysis. To appreciate better the differences between the two media, a brief description of the CCD characteristics will be given first, followed by a comparison with the performance of film.

A CCD is a solid state image sensor composed of a matrix array of charge-coupled photosites, or pixels (picture elements). Photons penetrating the silicon produce hole-electron pairs in proportion to the incident photon rate. The holes combine with free electrons in the substrate, while the photoelectrons are collected in the potential wells created by MOS capacitors, until read-out. Thermal energy in the silicon lattice produces free electrons, which are indistinguishable from those created by photons. The contribution of thermally generated charge is called dark current and it can be reduced to negligible levels by cooling the CCD's to about -50° C (see Appendix B).

In principle, the advantages of using a CCD system as a recording device in streamer chamber experiments are manyfold. First, CCD's have a large dynamic range, a linear response to light, a high quantum efficiency, and a good performance in low-light conditions. Second, the output of a CCD is in digital form, and can be recorded directly on tape,

thus avoiding the time-consuming processes of developing the film and digitizing the images. The events can also be displayed on a graphics terminal, providing a useful tool for on-line diagnostics both during the beam tune-up phase and during data-taking. Third, the digitized pictures can be processed for image enhancement, and easily lend themselves to computer-assisted track recognition and intensity scanning.

It is interesting to examine how these characteristics compare with those of photographic film, the other recording medium commonly used in streamer chamber experiments. A summary of the following discussion is given in table 2.3.1.

As was mentioned in sections 2.1 and 2.2, a large dynamic range is necessary in order to separate the wide variety of fragment charges and energies which are observed in heavy-ion collisions. The dynamic ranges of CCD's and photographic emulsions are compared in figure 2.3.1a and b. Figure 2.3.1a shows the typical response curve for a charge-coupled device digitized to 12 bits. Here E represents the exposure, defined as $E=tI$, where t is the time during which the medium was exposed to the light source, and I is the illuminance of the source [Ecc 83]. The exposure can be given in units of incident energy per unit area, or as photons per unit area. The response curve is linear for CCD's, and the useful dynamic range, after the subtraction of background noise, is of about 3000:1. A similar curve is plotted in figure 2.3.1b for film. The 'usable' region of the curve, where the response of the medium is logarithmic, includes a relative density range between about 1 and 2.5, corresponding to a dynamic range of about 300:1.

The quantum efficiency, defined as

Table 2.3.1. Characteristics of CCD's in comparison with photographic film. The values indicated with (*) are taken from [Djo 84].

	CCD	Photographic film
Pixel size	23 μm	8 μm
Resolution	1.7 mm	0.2 mm
Two-track resolution	3.7 mm	2.3 mm
Linearity	± 0.1 % (*)	poor (*)
Dynamic range	35 dB (*)	20-25 dB (*)
Quantum efficiency	≈ 60%	≈2% (*)
Data-acquisition rate (Bevalac Streamer Ch.)	1 ev./beam spill	≈3 ev./beam spill

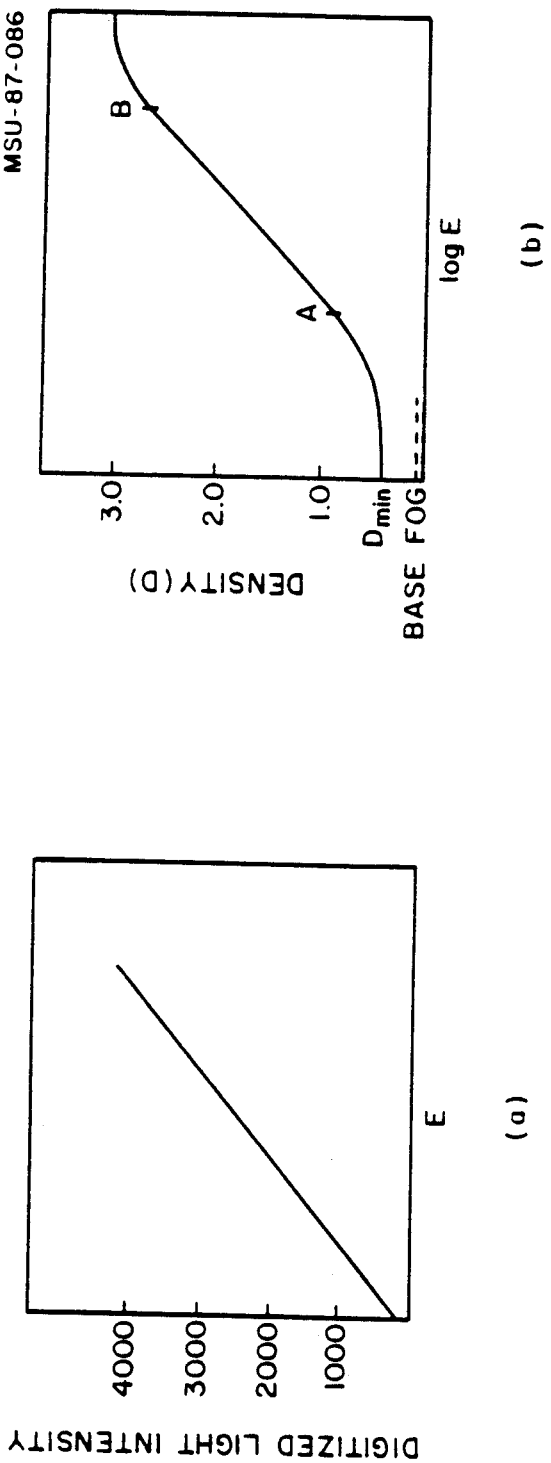

Figure 2.3.1 a) Characteristic curve of CCD response to exposure E. b) Characteristic curve for a photographic film.

$$Q.E. = \frac{\text{number of electrons collected}}{\text{number of photons absorbed}}$$

is about 60% for the Thomson devices used in our system, compared to a value of about 2% for film. This characteristic makes CCD's essentially photon-counting devices (for some chips the quantum efficiency is as high as 80%), and ideal for use in low-light conditions.

Resolution is where film offers some advantage over CCD's. Due to the smaller grain size and the larger area, the typical resolution for photographic film is about 0.2 mm. For the Thomson CCD's used in the system described in this work, the pixel size is 23 μm square, and the dimensions of the sensitive area of the chip are 13.2 mm x 8.8 mm. The resolution, defined as the "real" size of a line mapped on one pixel, is about 1.7 mm. This value depends on the demagnification necessary to image the whole chamber on the recording device, and the grain (or pixel) size of the medium. While these values appear very different, one must also include in the definition the size of the object to be recorded, the streamers viewed from the side. A better comparison is therefore given by the value called two-track resolution, defined as the minimum distance between streamers which can be identified as belonging to two different tracks [Ana 82]. This value is given by the expression:

$$D = \sqrt{D_A^2 + \frac{\Delta x^2}{F^2(M+1)^2} + [\lambda F(M+1)]^2 + M^2 \left(\frac{1}{R_1^2} + \frac{1}{R_m^2}\right)}$$

where D_A = size of a streamer (1 mm)

Δx = half depth of the chamber (20 cm)

F = f-stop (2)

M = demagnification (80 for CCD's, 50 for film)

λ = wavelength of the emitted light (6000 Å)

R_l = lens resolution (100 line pairs)

R_m = medium resolution (100 lp/mm for film
25 lp/mm for CCD's)

The first term in expression 2.3.1 represents the effect due to the size of the streamers, the other terms estimate the distortions due to depth of field, diffraction and resolution of the lens and CCD or film.

The values one obtains for the two media are D_{CCD}=3.7 mm, and D_{film}= 2.3 mm, showing that the resolution is only slightly worsened by the use of CCD's.

One of the main advantages of CCD's over photographic film, namely the possibility of digital image-enhancement and of computer-assisted analysis, will be discussed in detail in section 3.2.

2.4 Description of the CCD System

In order to do a three-dimensional reconstruction of the tracks, more than one view of a given event are necessary. For this reason, the system described here consists of three CCD cameras, with related read-out electronics. A schematic of the electronics is shown in figure 2.4.1.

The modules provided by Photometrics, Ltd. with each camera head include a model PS 830 T.E.C. (thermoelectric cooler) Power Supply, a model CH 84 Camera Head Electronics Module, and a model 80A Camera Controller. A 24 mm f/2 lens was mounted on each camera.

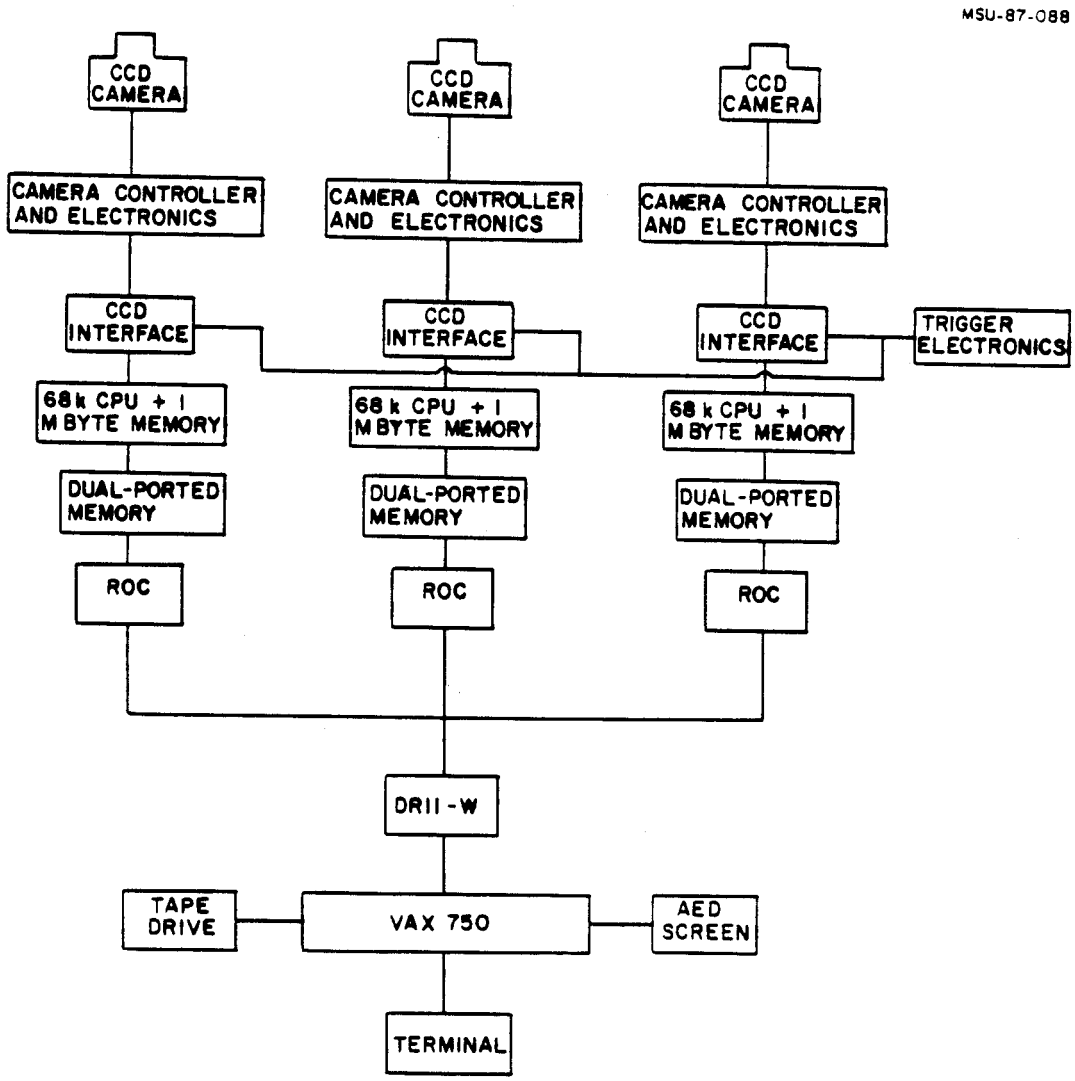

Figure 2.4.1 Schematic of the electronics for the CCD camera system.

The CCD chip is mounted in an evacuated enclosure in the camera head, which also houses the lens-shutter assembly. A thermoelectric cooler, soldered to a copper heat sink, is connected to the CCD, and the heat produced is removed by circulating a water-antifreeze mixture, cooled to about 10°C. A thermistor bonded to the cold sink near the CCD allows the determination of the cold side temperature from a reading of the current. During the operation of the cameras, the temperature was maintained at around -45°C.

The camera-head Electronic Module provides shutter control, it contains the clock drivers for the CCD and the analog processing, and it houses ADC electronics.

The Camera Controller serves several purposes. It provides all timing signals for the Camera Head, it receives serial digitised data from the Camera Head, and produces parallel output. Also, it provides user interfacing through manual input on the front panel, or digital control input from the rear panel. The control parameters that can be sent to the camera are in the form of hexadecimal command codes (0-F), defining the task to be performed, or which data are being transferred, plus an eight-bit data word determining read-out parameters, such as the size and origin of the array to be read out in the CCD, exposure time, etc.

During an experiment, when an event of interest occurs, the CCD's must be read out, and the resulting image digitally processed and transferred to tape. The details of the trigger hardware and the software will be given in sections 2.5 and 2.6. Here, the electronic system developed to accomplish the purposes mentioned above will be described. A detailed CCD-to-VAX block diagram is shown in figure 2.4.2.

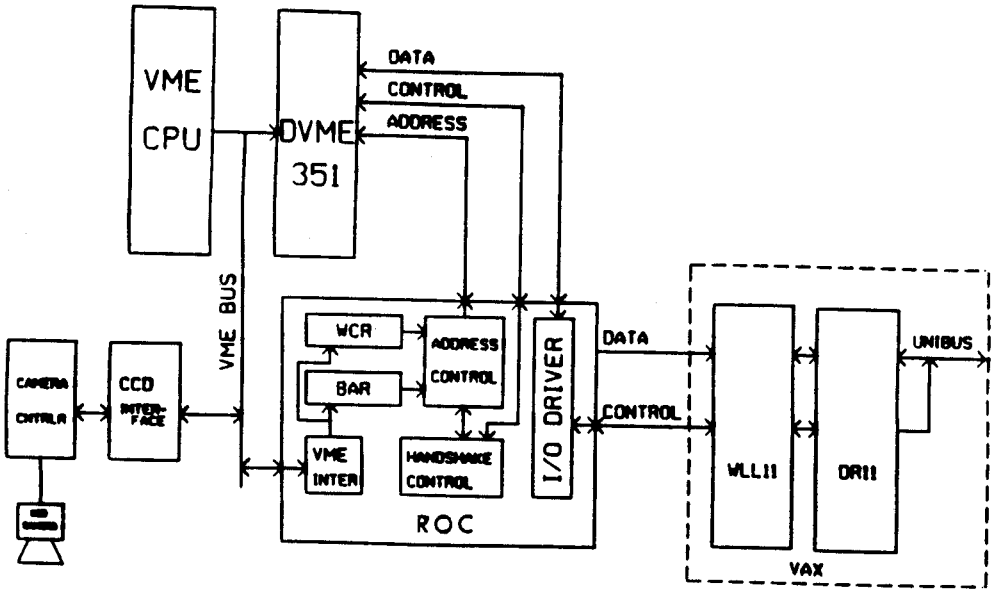

WCR=WORD COUNT REG.
BAR=BEGINNING ADDRESS REG.

Figure 2.4.2 CCD-to-VAX block diagram.

Each of the three CCD systems is run by a dedicated SYS68K/CPU-2F microcomputer. This is a VMEbus based board, which combines a Motorola 68000 CPU chip and, in our case, 1 Mbyte of RAM. The clock frequency is 10 MHz, corresponding to a cycle time of 0.1 μsec.

Each camera controller is interfaced to a CPU board through a CCD-camera to VME interface. This board, designed and built in-house, allows operation of the cameras, through a one-word command input register, and read-out through a one-word Z-digital output register. The same board also interfaces the VME crate to the external trigger, using a strobe (write-only) register, and a status (read-only) register. The first allows visual control of the status of the process, through an LED panel, where different color lights indicate the current stage of processing: green, when the camera is ready and waiting for a trigger; yellow, when the camera is taking an exposure; red during read-out. The status register contains the information on FIFO synchronism, and trigger and camera status. A schematic description of the contents of the four CCD-interface registers is shown in figure 2.4.3.

Each CPU processes the image from one of the cameras using the 1 Mbyte on-board memory, then transfers the results to a Mass Memory Board (DVME 351, a commercial board, with 1/2 Mbyte of memory) with dual port access. This board allows read/write access by the VMEbus master and read-only access by a Read-Only Controller (ROC).

The ROC's have also been designed and built in-house. They provide for high-speed parallel transfer of data from the dual-ported memory to the DR11-W board, which resides in a VAX computer. The events are then stored on magnetic tape, and they can also be displayed, on-line, on an AED screen.

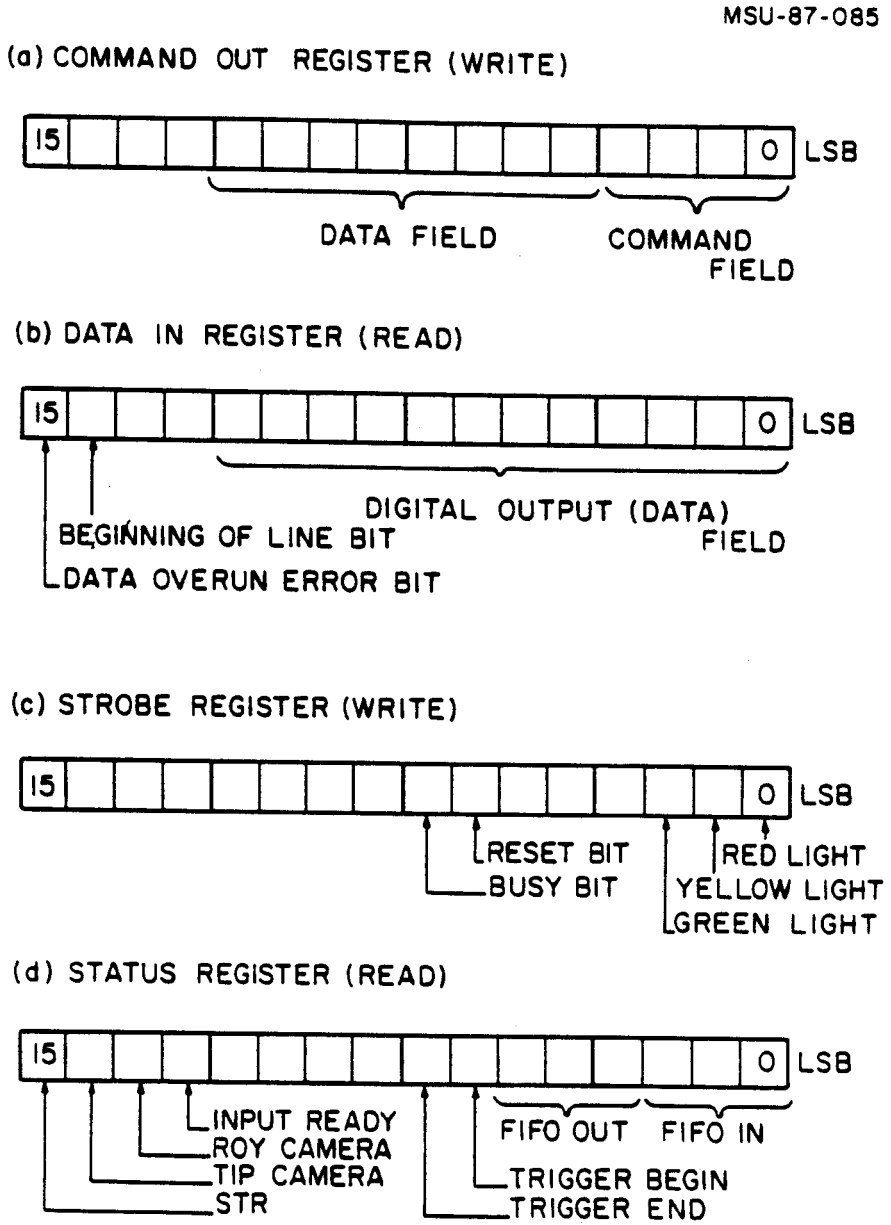

Figure 2.4.3 Description of the read/write registers in the CCD interface.

The next sections will deal with the rest of the experimental set-up, and will describe the software used to run the system during data-taking.

2.5 The LBL Streamer Chamber

The main components of the LBL streamer chamber are shown in figure 2.5.1, in which a schematic view of the chamber, seen from the top, is given. The Marx generator provides the high-voltage pulse; a main spark gap and a Blumlein transmission line shape the pulse before it is applied to the chamber; and the trigger counters with their electronics fire the Marx generator and the cameras when an event of interest occurs. Not shown in the figure is the dipole magnet in which the chamber is placed.

The streamer chamber has a rectangular shape, 120 cm long, 60 cm high, and 40 cm deep. Its body is made of polyurethane foam, except for the back plane, which is made of aluminum, and the transparent mylar front window, through which the photographs are taken.

The high-voltage electrode, made of stainless steel wire mesh, is placed in the center of the chamber, so that the chamber itself is essentially divided into two 20 cm deep areas. The front electrode is also made of wire mesh.

The dipole magnet, which generates the magnetic field in the chamber, produces a field of up to 1.32 T, normal to the electrodes.

A two-stage Premarx and a twelve-stage Marx generator provide the high-voltage pulse, of up to 720 kV. The main spark gap controls the voltage of the pulse applied to the chamber, and a Blumlein line reduces and controls the duration of the applied field. The length of the pulse can be varied between 5 and 15 ns [Van 82].

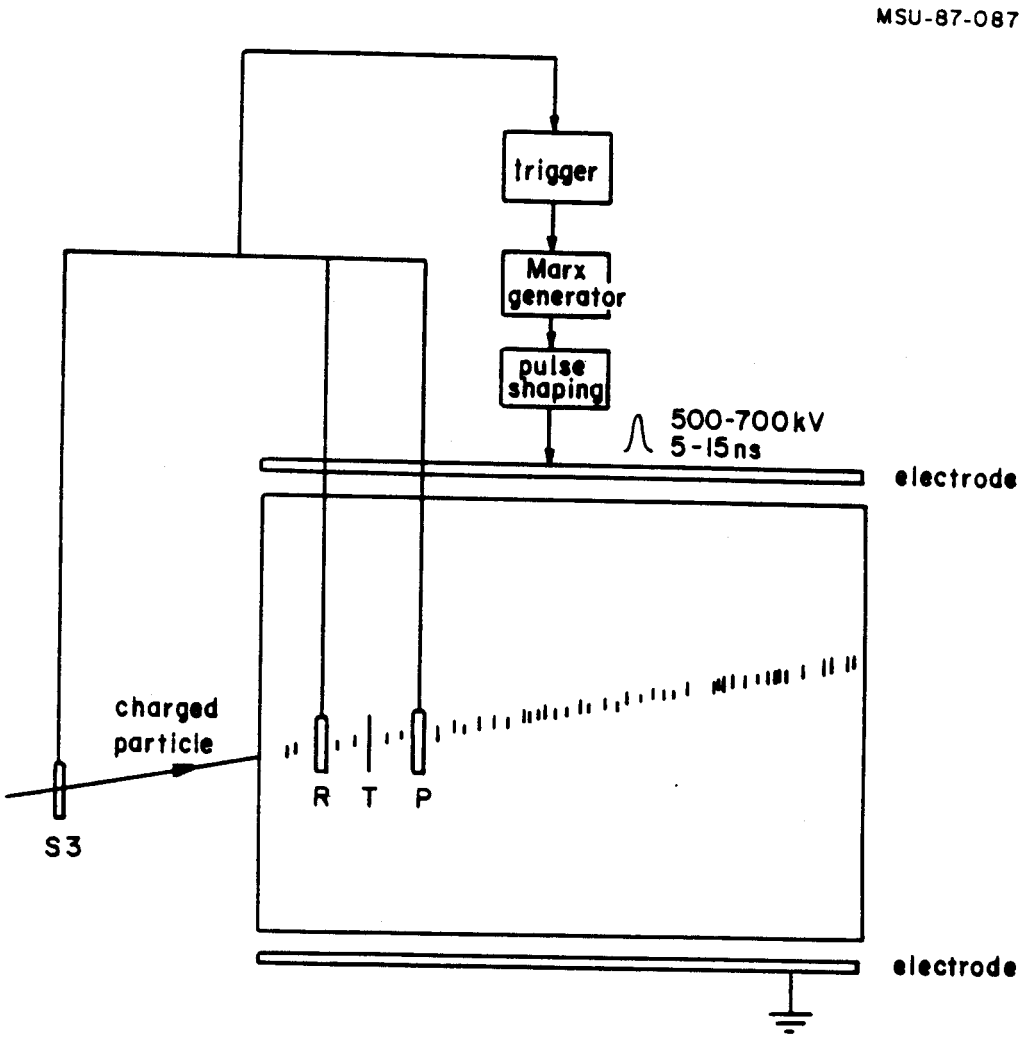

Figure 2.5.1 Main components of the LBL streamer chamber (adapted from [Sch 79]).

A coincidence between a plastic scintillator (S3), located at one of the focuses of the beam, and a scintillator (R-counter), located inside the chamber, about 5 cm upstream from the target, defines the beam signal. The trigger scintillator (P-counter) was placed about 30 cm downstream from the target and is used in anticoincidence with the signal from the two beam counters. The S3 counter was 0.22 mm thick, and was mounted at a 45° angle with respect to the beam direction. For the R-counter, a thickness of 0.64 mm was used for the 180 MeV/nucleon beam, and 0.22 mm at 100 MeV/nucleon. The P-counter was 2 mm thick.

The plastic scintillators are inserted through the back plane, and are connected to long light-pipes, so that the phototubes are outside the chamber.

In order to have a trigger signal for the Marx generator and the cameras, we required a valid beam signal (S3·R) with a pulse in the P-counter below a predetermined threshold (trigger : $S3 \cdot R \cdot \bar{P}$). By varying the threshold level, it is possible to select events corresponding to different amounts of energy deposition in the downstream (P) counter, from an 'unbiased' trigger, when the threshold is at beam pulse height, to central trigger, when the threshold is at about 10% of the beam pulse height.

The purpose of the experiment described in this work was the study of central collisions between two Nb nuclei, which, at 100-200 MeV/nucleon, are characterized by the shattering of the target and projectile into a large number of fragments, emitted in different directions. The central trigger was therefore selected for the experiment.

2.6 The Experiment

The Bevalac produces a pulsed beam, with spills about one second long and 4 seconds apart. As a consequence, the cameras start an exposure at the beginning of a beam pulse, and the read-out must begin when an event of interest occurs, simultaneously with the triggering of the Marx generator. A listing of the assembly-language code that handles the various signals and operates the cameras is given in Appendix A. What follows is a description of how the different tasks are executed.

Before a beam burst starts, the cameras are running in the "fast charge dump" mode, which clears the CCD's continuously, until a new command is issued. At the beginning of a beam pulse, the fast clear instruction is interrupted by sending a set of commands that define the size and origin of the array to be read out (the entire CCD in our case). The CCD's are now being exposed. If a valid event signal is sent at any time during the beam spill to trigger the chamber, the CCD's are read out, and further triggers are inhibited until the current event has been processed.

One of the problems that had to be solved in order to make this type of system viable was the handling and storage of the large amount of data obtained for each recorded event. The read-out of each of the CCD's used in this system, where the charge accumulated in each of the 221184 pixels is digitised to 12 bits, consists of almost 0.5 Mbytes of information. In order to reduce the amount of data to be transferred to tape, a previously stored background frame is subtracted and a low-level threshold applied (see Appendix B for a description of the contributions to the background). The pixels whose content is below the threshold level

are discarded, and only the remaining ones are transferred to the dual-ported memory, together with a series of bit masks, containing the information on which of the pixels are below or above the threshold.

This type of processing reduces the amount of information that is stored on tape by 30 to 60%, depending on the event multiplicity and the number of flares.

After the CPU's have finished processing the current event (a different view for each system, in parallel), and have stored the non-zero values and the bit masks in the dual-ported memory, the downloading of the processed frames to the VAX can start, through the ROC boards, and the next exposure from the CCD's can proceed simultaneously, thanks to the use of the dual-ported memory boards.

During data acquisition, randomly selected events can be displayed on an AED screen, providing on-line monitoring of the experiment. This has proven to be a very useful diagnostic tool.

As mentioned earlier, one obvious disadvantage of a CCD plus streamer chamber system is the slow event-rate imposed by the processing and transferring of the large amount of information collected. The rate of one event per beam spill, obtained with CCD cameras, should be compared with that of about three events per spill when film is used.

A total of about 1000 central collisions was recorded at each energy in about 60 hours. Obviously, a large number of the collected events is eventually discarded, for several reasons. First, the target thickness is comparable to the thickness of the several windows, counters, chamber gas, and air that the beam must go through. This causes a high number of interactions to occur with nuclei other than those in the target. Secondly, some rather peripheral collisions, while producing only a few

fragments, deposit so little energy in the P-counter that a valid trigger signal is sent to the chamber.

It is possible that, by using a different trigger system and by allowing the counters in the chamber to be moved vertically (therefore correcting for the bending of the beam when the magnetic field is applied), the number of such spurious interactions could be reduced.

Chapter Three

DATA REDUCTION AND ANALYSIS

3.1 Introduction

While a streamer chamber offers several advantages as a 4π-detector for heavy-ion collisions, one major drawback is the time-consuming task of digitizing the images and recognizing the tracks. The amount of time involved in this part of the analysis is one of the reasons for the low statistics usually obtained in such experiments, the other being the slow data acquisition rate.

When the recording medium is photographic film, the film must first be developed, then scanned on an image plane digitizer by an operator. The coordinates of the digitized points along each track are stored on magnetic tape for the spatial reconstruction of the event [Str 84].

The use of CCD cameras eliminates the necessity of handling and developing film, since the whole digitized image is directly stored on magnetic tape during the experiment.

Since parts of the tracks are frequently obscured by flares, the use of digital image-enhancement techniques is extremely helpful. Therefore, our CCD pictures are first processed to make tracks more visible and to reduce the background. As a second step, a track-recognition program attempts to find and follow all the tracks in the event. Omissions and errors can be later corrected by an operator.

Once the coordinates of points along the tracks have been determined in all three views, the Three View Geometry Program (TVGP) [Som 66] reconstructs the trajectory of each fragment in three-dimensional space, determining the radius of curvature (R), emission angles (dip and

azimuthal), and length of the track. If the magnetic field is known, R provides the magnetic rigidity (p/Z) of a particle, since RB=p/Z. Therefore, determination of the fragment charge is necessary in order to find its momentum.

In a streamer chamber, particle identification relies on the analysis of track intensity. As mentioned before, while the energy loss of a particle in a gas is proportional to Z^2, the intensity of the light emitted in the streamer regime does not show the same charge dependence. Nevertheless, information about the charge and mass of each fragment can be extracted by combining the rigidity and intensity information. In this way, the emitted particles can be identified and their 4-momentum calculated.

The rest of the chapter will describe how the various steps of the analysis are performed. A summary of these steps is given in a flow chart in Appendix C.

3.2 Image Enhancement and Track Recognition

Several methods have been developed to process digital images in order to enhance the features of interest, reduce the background, etc. In the case of streamer chamber events, where particle tracks are to be recognized and reconstructed, an edge-enhancing technique has been adopted, which reduces such unwanted features as flares and background illumination, while making the track narrower and better defined.

The processing consists of calculating the angle between the line joining a point on the track with the vertex and the horizontal, and then taking the double derivative of the intensity with respect to this angle for each point in the image. How this double differentiation operates on

a gaussian-like curve is shown qualitatively in figure 3.2.1. Once the double gradient has been calculated, the sign of the negative values found (refer to figure 3.2.1c) is inverted, and the positive ones are set equal to zero. In practice, the central negative peak in figure 3.2.1c becomes positive and is all that is left of the original track. In this way, the tracks, characterized by a sharp rise in intensity, become narrower and well defined, while the background and the slowly-varying illumination due to flares disappear. Figures 3.2.2 and 3.2.3 show an event at 100 MeV/nucleon before and after the processing just described.

Using the image-enhanced picture, the track-recognition code starts scanning in vertical swaths at the right edge, searching for non-zero points. For each point found, the search is continued in a grid of 3X5 pixels, tilted along the direction of the line joining the point and the vertex. The intensity-weighted average of the x and y coordinates of the non-zero points found within the grid is calculated, and the search moved to the new point.

Before a new point is added to an existing segment, the least-squares slope of the last six points of the segment is compared to the slope given by the last three points (including the new one) and, if the difference is less than 20°, the new point is added to the track.

After the whole picture is scanned, the segments less than 10 points long are discarded. The remaining ones are compared and the tracks are reconstructed by matching adjacent segments with similar slopes.

The recognized tracks are then numbered, and a 'track' file is written to disk, which contains the track numbers, number of points on each track, and the x and y coordinates of the points.

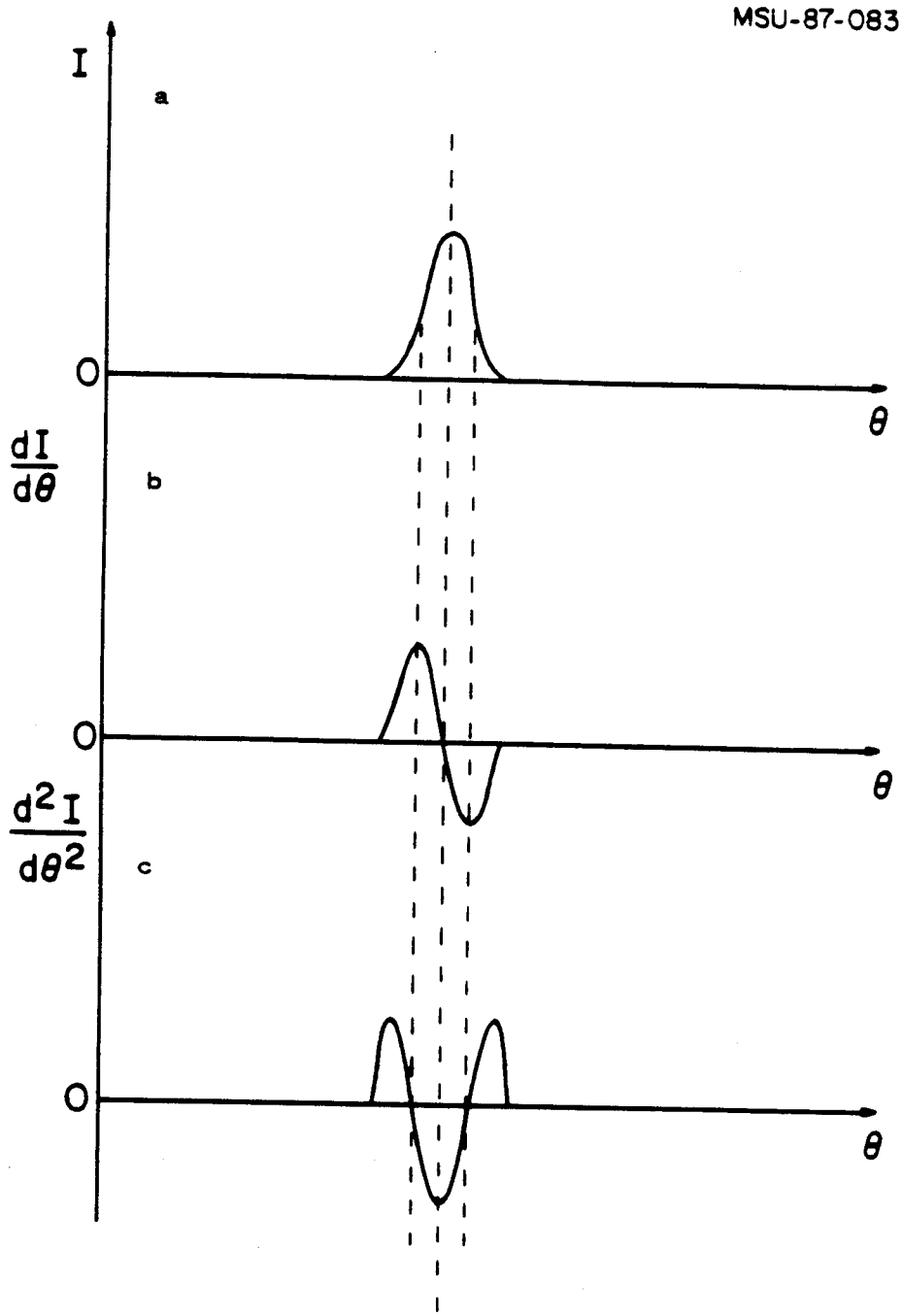

Figure 3.2.1 a) Gaussian-type curve which approximates the intensity along a cut perpendicular to a track. b) First derivative of intensity with respect to angle. c) Second derivative of intensity with respect to angle.

Figure 3.2.2 Nearly-central collision at 100 MeV/nucleon. Unprocessed event.

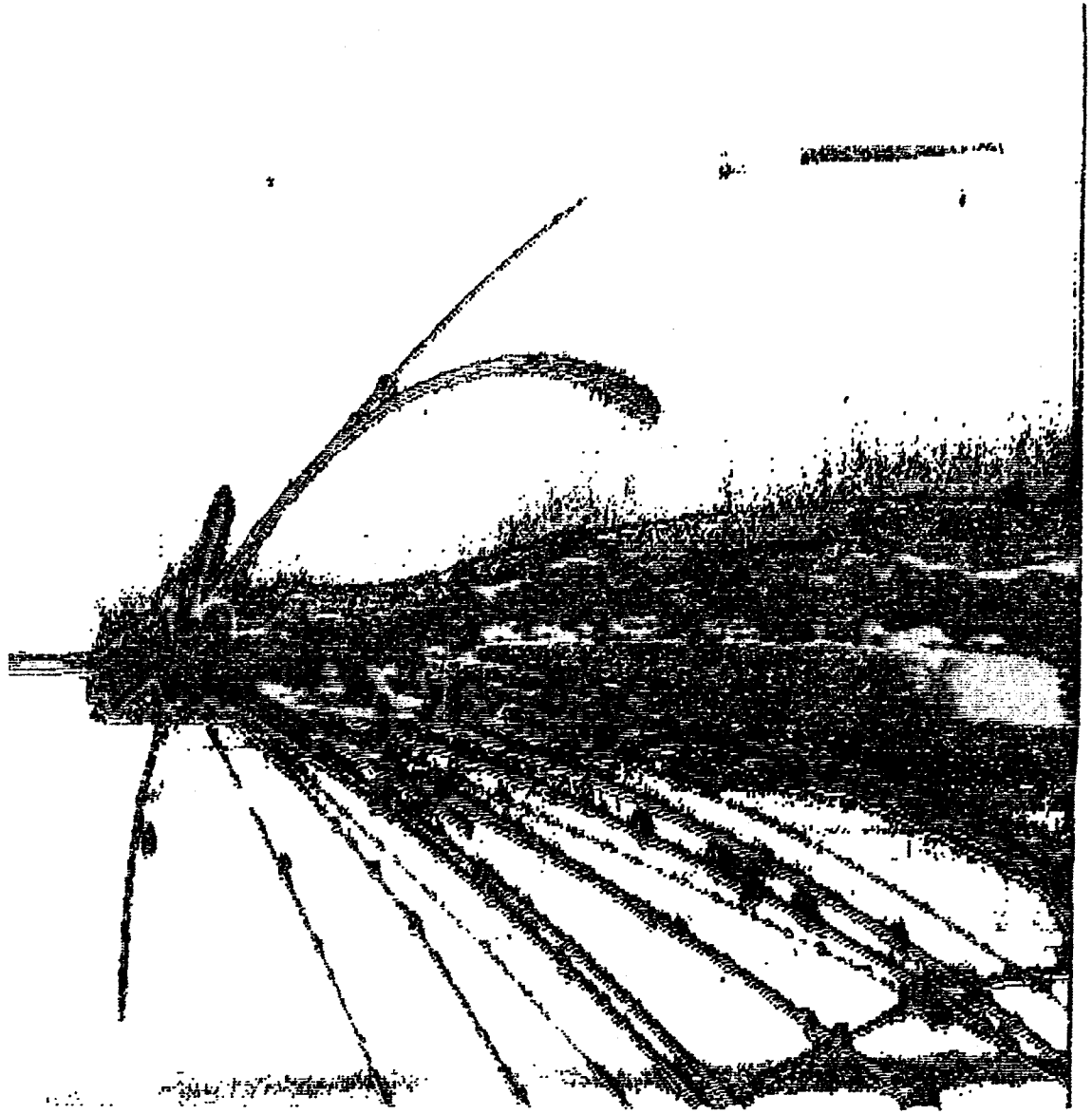

Figure 3.2.3 Event in figure 3.2.2 after image-enhancing processing.

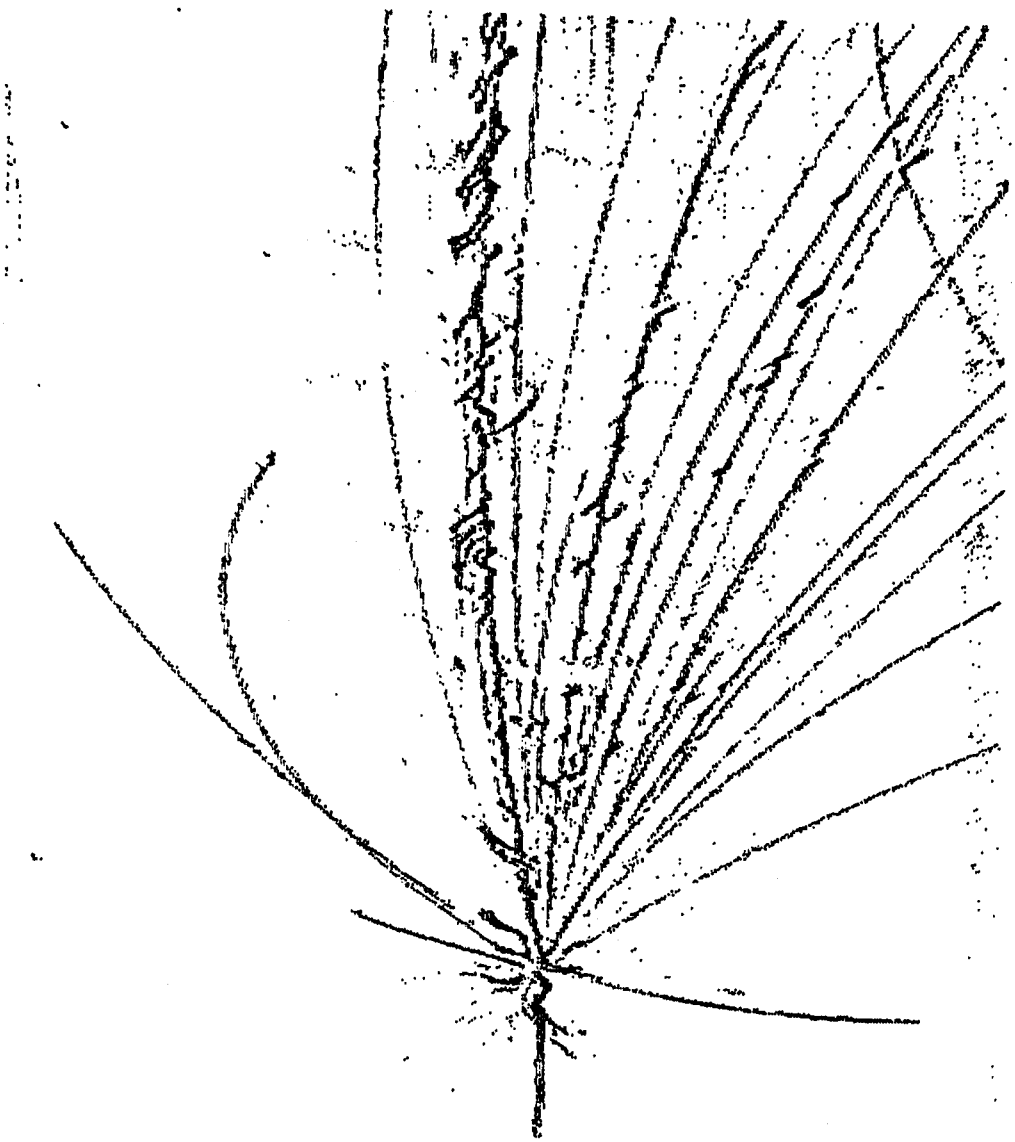

At the present stage, it is still necessary for an operator to display the processed event and the output of the track-recognition program on a color graphics terminal, where corrections and additions to the tracks can be introduced. The extent of this intervention is strongly multiplicity-dependent (the higher the number of tracks, the higher the likelihood of crossing and partially overlapping tracks, which confuse the search) and it also depends on the overall quality of the image.

After all the tracks have been recognized, the operator introduces the position of the interaction vertex, which is added as a last point to all the tracks, and a third degree polynomial is fitted to each track. The tracks found in the event shown in figures 3.2.2 and 3.2.3 are plotted in figure 3.2.4. At this point, a new track file is written, which is used for the next step in the analysis of the event, namely the three-dimensional reconstruction.

3.3 Three-View Geometry Program

The programs described in this section, WEASEL and TVGP, were originally written in 1965 to process bubble chamber pictures, and were later modified to be used with streamer chamber photographs.

After the tracks in three views have been recognized, files containing the (pixel) coordinates of the track points are created. The three different views record different projections of an event relative to fixed fiducial marks. The three-dimensional reconstruction of each track is based on the fact that, by measuring the projection of a point on a fixed plane, seen from two different views, the intersection of the rays from the projected point to the cameras gives the position of the point in space. In figure 3.3.1 the trajectory of a particle in space,

Figure 3.2.4 Tracks found for the event in figure 3.2.2.

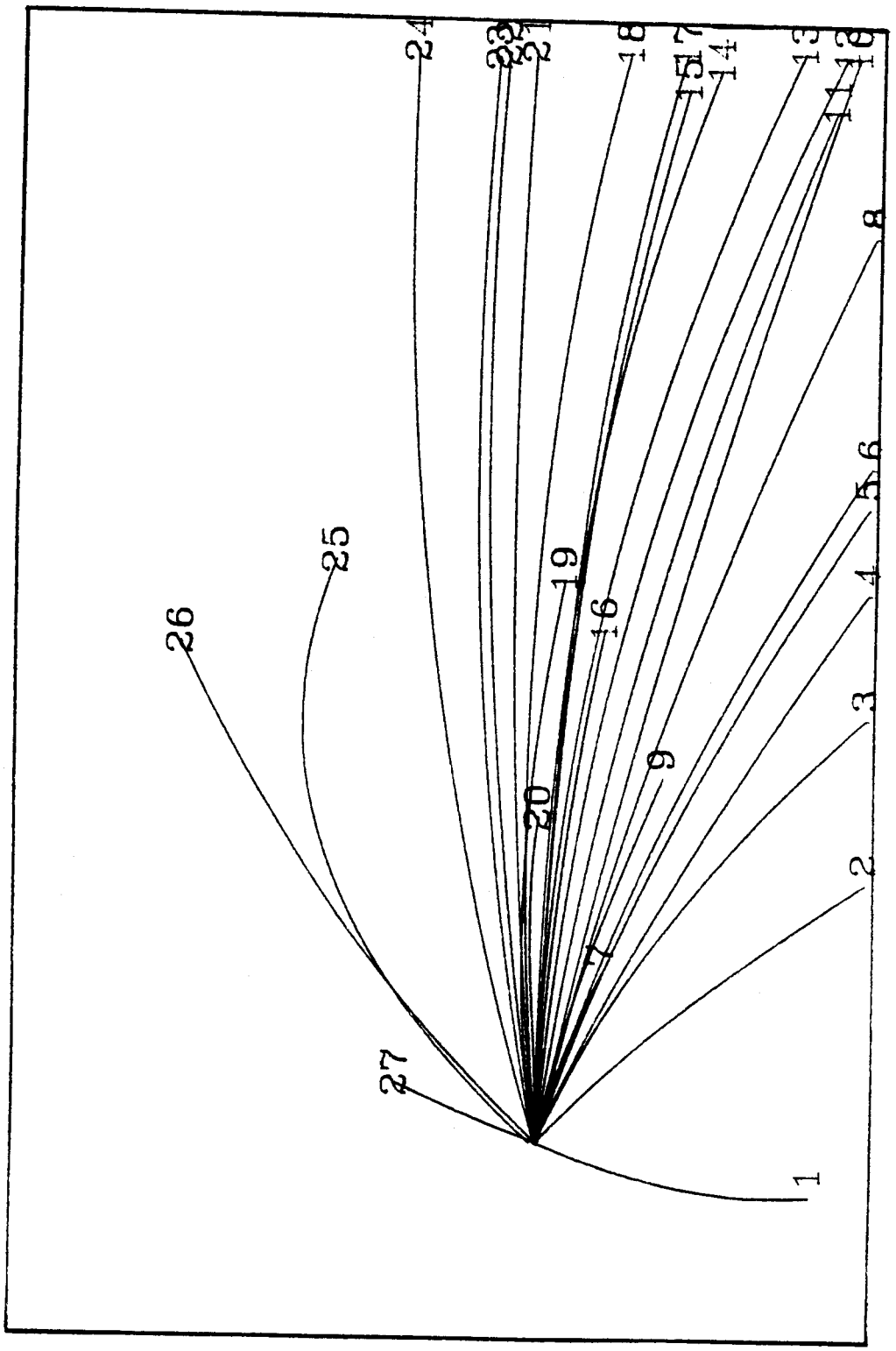
24
23
22
21
18
15
14
13
12
11
10
8
6
5
4
3
2
1
9
7
16
19
20
25
26
27

MSU-87-084

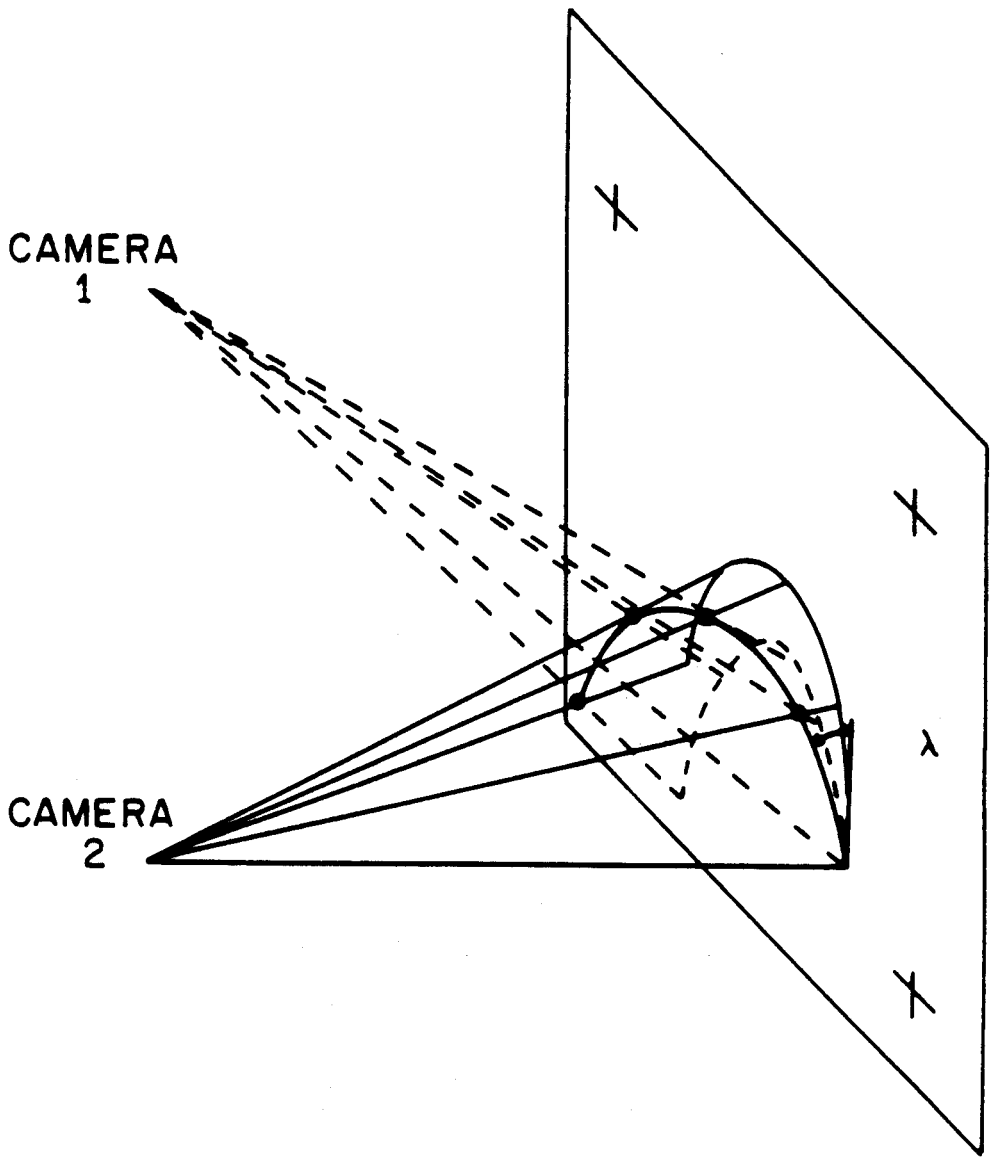

Figure 3.3.1 Trajectory of a particle in space and its projections as seen from two different views. λ is the dip angle.

with dip angle λ, is shown. From the projections observed from cameras 1 and 2 on a plane defined by a set of fiducial marks of known coordinates, the trajectory can be reconstructed.

The first step in the spacial reconstruction of an event is the measurement of the position of the fiducials on the CCD planes. The (averaged) x and y coordinates of the fiducial marks (in pixels), their real space coordinates in the streamer chamber geometry, and the approximate position of the three cameras are the input for WEASEL, a program that calculates rotation, translation, and magnification for each camera, and the optical parameters used by TVGP in the track reconstruction. The system of axes associated with the streamer chamber in these calculations, and in those performed by TVGP, is centered around the position of the target. The x-axis is vertical, the y-axis is in the direction opposite to the beam, and the z-axis is towards the cameras.

This part of the calculations needs to be done only once, in our case, since the CCD planes, unlike film, do not move from one event to another.

Before running TVGP, the tracks recognized following the procedure described in section 3.2 must be matched in the three views. The coordinates of the matched tracks are then read by TVGP.

The steps of the reconstruction performed by the Three View Geometry Program are summarized in the following paragraphs.

i- For each view, a circle is fitted through the points, to help check for bad points (which will be dropped from the reconstruction); for interpolating between points; and for getting space-point weights.

ii- For each view, the good points are rotated to two stereo systems (given, e.g., by views 1-2 and 1- 3). This is done for all views.

iii- A new view-loop is started. Here, for all the points in the primary view, the corresponding points are found, by interpolation, in the other two views.

iv- For each point, the z-coordinate in each stereo system is found using the intersection of the rays from the two projections. The final z-coordinate in space is the weighted average of the two points reconstructed in the two stereo systems.

v- When all the approximate space-points are reconstructed, a circle is put through the first, middle and last point. At this stage, for a given track, approximate space points, optical-ray components, and projected arc-lengths, approximated by circular arcs in the x,y plane are known.

vi- Now, the corrections due to variations in the magnetic field and energy loss must be introduced, and a space-curve calculated such that its projection on the CCD plane minimizes the distance to the measured track. Such a curve is described by a set of five parameters and by functions, incorporating these parameters, from which the points in space can be calculated.

vii- For each point, the least-squares errors are calculated and added to the appropriate summation. When all the points have been used, the error matrix is found by inverting the 5x5

summation matrix of derivatives, and the corrections to the five parameters are found.

viii-Now the five parameters of the fit are available. They are angles, curvature, and x,z position near the middle of the track. These parameters, and their error matrix, are then propagated to the beginning and end of the space-curve, using the assumed functional form of curvature and slope vs. projected arc length.

The results obtained from this procedure are the curvature, angles, and space coordinates at the beginning and end of each track.

The product BR, where B is the magnitude of the magnetic field and R is the radius of curvature of the track, gives the magnetic rigidity of the particle, which is also equal to p/Z (momentum divided by the charge). From the azimuthal and dip angles, the projections of the magnetic rigidity along the three axis in the chamber geometry are calculated.

The accuracy of the results calculated by TVGP was estimated by using computer-generated tracks of known momentum (in magnitude and direction) in a known magnetic field. The coordinates of three projections were used as an input for TVGP. For such an ideal case, the rigidity and emission angles of the reconstructed track deviate very little (about 0.25%) from the original values.

Several factors contribute to a much larger error in the analysis of 'real' streamer chamber tracks. The first is the non-negligible width of the recorded tracks, which introduces an uncertainty in the position of the points along the tracks themselves. Secondly, the points used as an input for TVGP are the result of a polynomial fit, and the fitted curve

may, in some cases, deviate slightly from the original trajectory. In the third place, the high density of tracks around the vertex makes the exact determination of its position difficult, thereby introducing a further deviation from the real track in a region where the track is especially difficult to observe.

Another problem which is encountered in the analysis of the recorded events, especially at the higher multiplicities, is the difficulty of matching the tracks in the three views when some of the short tracks are obscured by flares, or are simply not visible in one or two of the views, or when several longer tracks are emitted so close together, and are so similar in intensity, that the determination of the proper match is very doubtful. This factor limits the success rate for TVGP to about 80% for the 180 MeV/nucleon data, where the multiplicities are higher, and to a little better than 90% for the 100 MeV/nucleon data.

3.4 Intensity Analysis

The intensity of the light emitted by a charged particle in the streamer chamber provides information on the energy loss of that particle as it passes through the gas in the chamber.

In principle, when magnetic rigidity and dE/dx are known, the identification of the emitted particle is possible, e.g. from a scatter plot where the intensity is plotted vs. rigidity, in the same fashion as a common dE vs. E plot. A rather accurate determination of the track intensity is therefore very important.

In the case of particles emitted in a streamer chamber, up to two or three hundred points per track are usually visible in a CCD picture (less for shorter tracks, or for tracks emitted at large angles towards or away

from the cameras). Our intensity analysis takes advantage of the fact that this reconstruction gives us a large number of points along each track, as described in the following paragraphs.

The starting points for the determination of the intensities are the 'track' file containing the coordinates of the points found along each track, and the original CCD-recorded event, where the digitized image contains the available information about the light intensity.

Starting from each point in the track file, a search is made in the direction perpendicular to the track for the true maximum intensity on the track, and for the minima on either side of the maximum. At the end of this step, the intensity has been determined along the width of the track itself, for each point along the track. Now, after subtracting a locally determined background, the intensities along each cut are added, to give the total intensity for the entire width of the track.

This gives us the light intensity for a large number of points along the length of the particle trajectory in the chamber.

For the purpose of particle identification, the fragments emitted in an event can be divided into two groups: those that stop in the chamber and those that do not. For the first group of particles, the intensity information is not strictly necessary, since the fragments can be identified from their range in the gas and their rigidity, both of which are obtained from TVGP. For these fragments the energy loss dE/dx is not small compared to the energy, and it increases rapidly, peaking at the end of the range. The Bragg peak typically observed for stopping fragments is seen in the streamer chamber in these cases, as shown in figure 3.4.1. Here the intensity at each point along the track

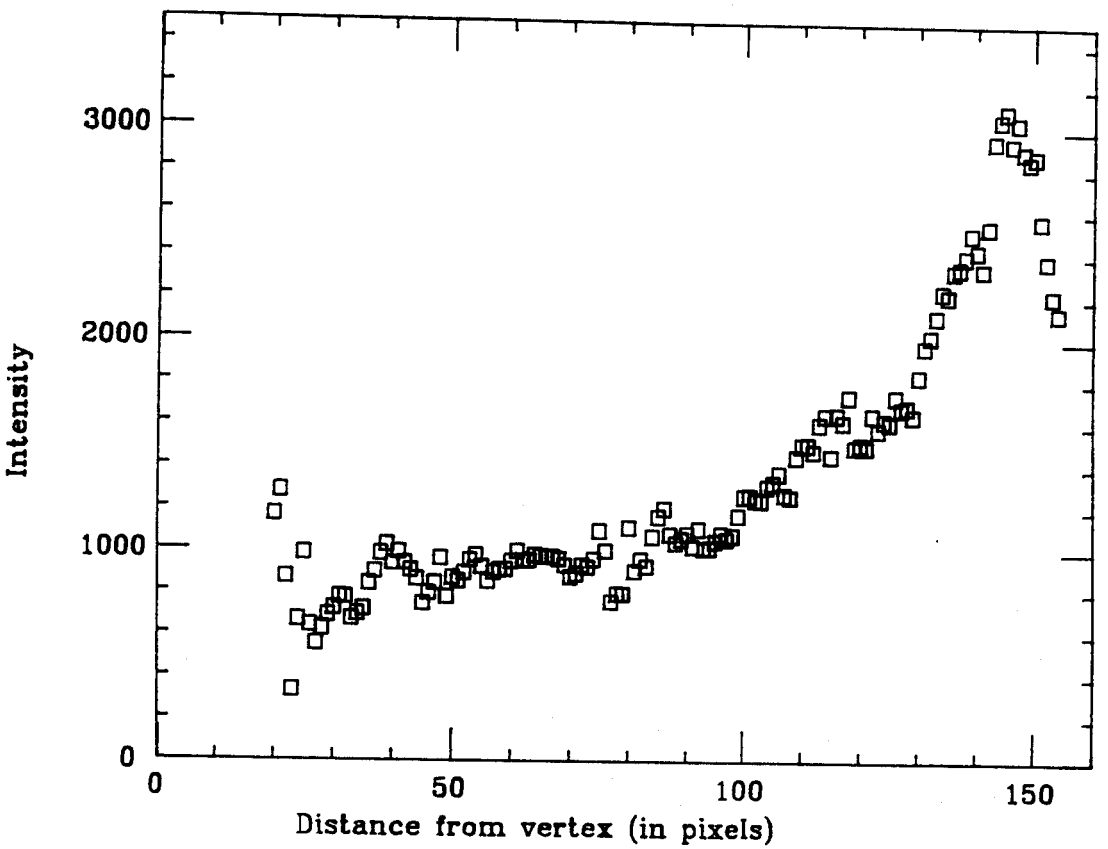

Figure 3.4.1 Bragg peak observed for a proton stopping in the gas of the streamer chamber.

(calculated as described above) is plotted as a function of the distance from the interaction vertex.

For the fragments that do not stop in the chamber the intensity (proportional to the energy loss) is a necessary piece of information, together with the rigidity, to determine A and Z. In this case, the statistics of the energy loss can be described by a Landau distribution, which is characterised by a sharp rise on the low-energy side and a high-energy tail [Igo 59, Seg 64]. The maximum of the distribution corresponds to the most probable energy loss, as shown in figure 3.4.2. One advantage of using an energy loss distribution to obtain the track intensity, rather than calculating the average intensity per unit length, is that those points along the track which are obscured by flares will fall in the high-energy tail of the distribution and will not influence the evaluation of the maximum. In figure 3.4.3, where the intensity along a track is plotted as a function of the distance from the vertex, the localised flares and the areas of relatively constant energy loss are evident. Some typical intensity distributions for our data, showing the features of a Landau curve (except for the low-statistics case) are plotted in figures 3.4.4a, b, and c. This figure also shows the large range of intensities usually observed in an event.

By these means, magnetic rigidities (rig) and track intensities (I) are obtained for most of the charged particles emitted in an event. By plotting each rig,I point on a scatter plot particle identification should be possible. In practice, for our data, this has proven to be a rather uncertain enterprise. The first problem, due to a less-than-optimum performance of the streamer chamber, was that of many flares along the tracks, which caused large uncertainties in the intensities.

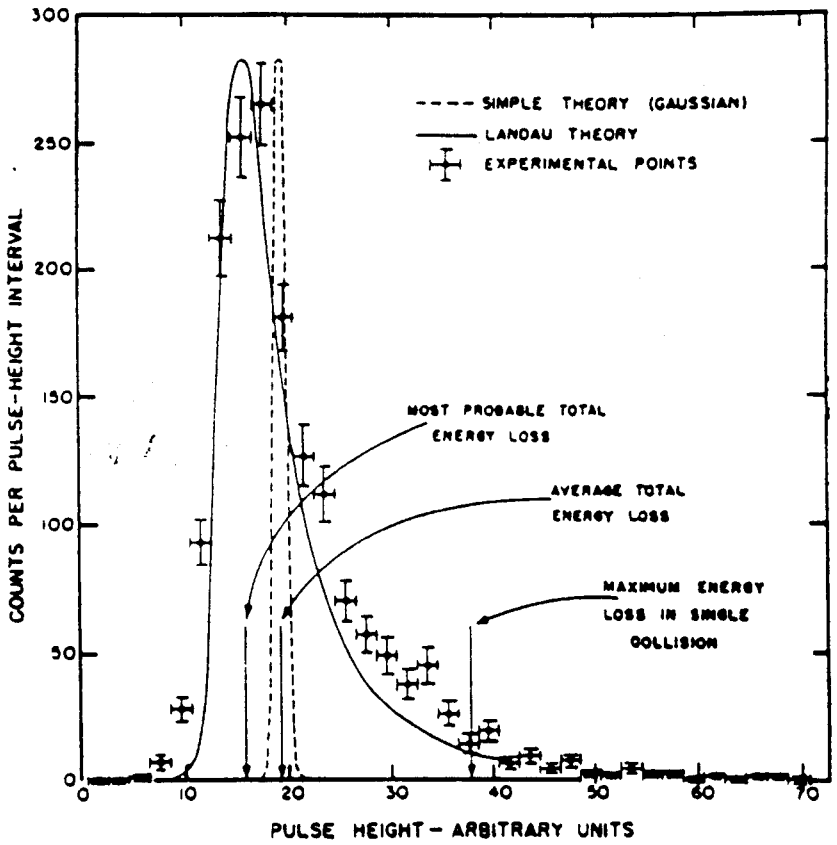

Figure 3.4.2 Experimental distribution of energy losses of 31.5 MeV proton. The corresponding theoretical Landau distribution is also shown (taken from [Igo 53]).

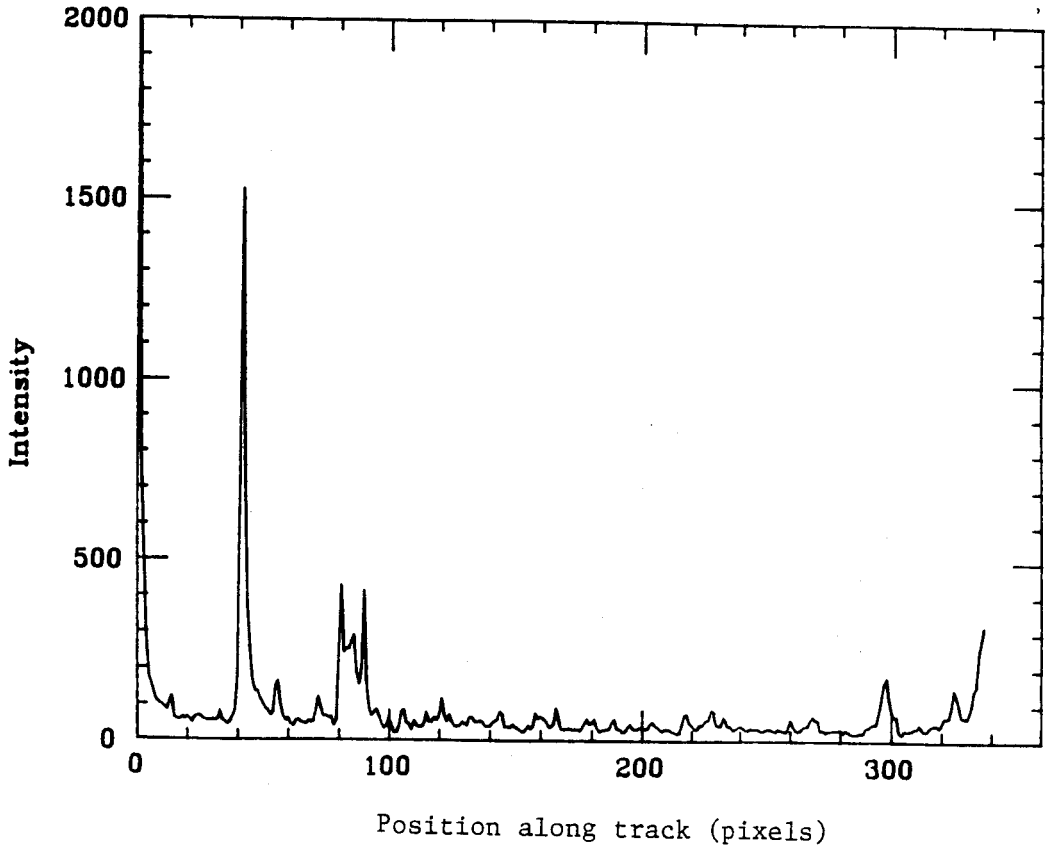

Figure 3.4.3 Intensity along a track as a function of distance from the interaction vertex.

Figure 3.4.4 Intensity distributions for three different tracks in a CCD-recorded event.

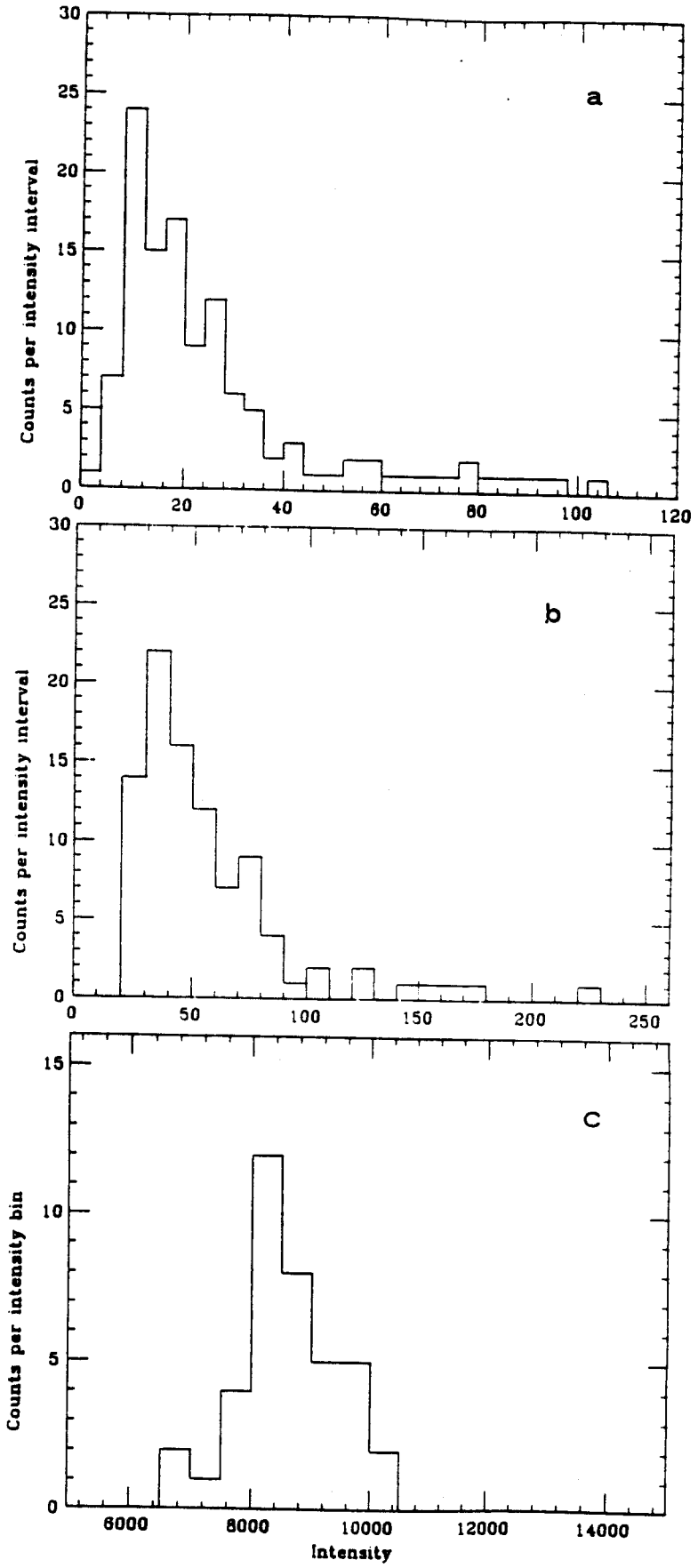
a
Counts per intensity interval
0
5
10
15
20
25
30
0
20
40
60
80
100
120
b
Counts per intensity interval
0
5
10
15
20
25
30
0
50
100
150
200
250
c
Counts per intensity bin
0
5
10
15
6000
8000
10000
12000
14000
Intensity

This fact is illustrated in figure 3.4.5, where the intensity at each point along a track is plotted vs. the distance from the vertex. In this figure, which exemplifies an extreme case of flaring, the track is obscured by large flares, which saturate the CCD along most of its length, and the determination of the actual intensity is impossible.

The second problem arises when data from different events are compared. Since the amount of light emitted by a fragment depends on the height and duration of the electric pulse applied to the chamber, variations in pulse height from event to event require that the intensities be normalized before they can be compared. For our experiment, a laser beam was to be used for this purpose. The beam, leaving a constant-ionization track (approximately corresponding to a mimimum-ionizing particle), would have provided a known reference intensity for an event-to-event normalization. Unfortunately, the laser used for this purpose at the LBL streamer chamber was not functioning properly at time of our experiment, and could not be used. Other ways of normalizing the intensities in different events had to be considered, and our criterion for the determination of this normalization factor will be described later.

Due to these problems, our 2-dimensional (I vs. rig) plot does not show a distinct isotope separation, and the fragment identification was based on an algorithm to be described.

An important question to be addressed in dealing with the intensity of the light emitted in a streamer chamber is how it depends on the charge and velocity of the particle. It is known that, because of the statistical process of streamer formation (not all ionization sites develop streamers), the light does not show the same Z and v dependence

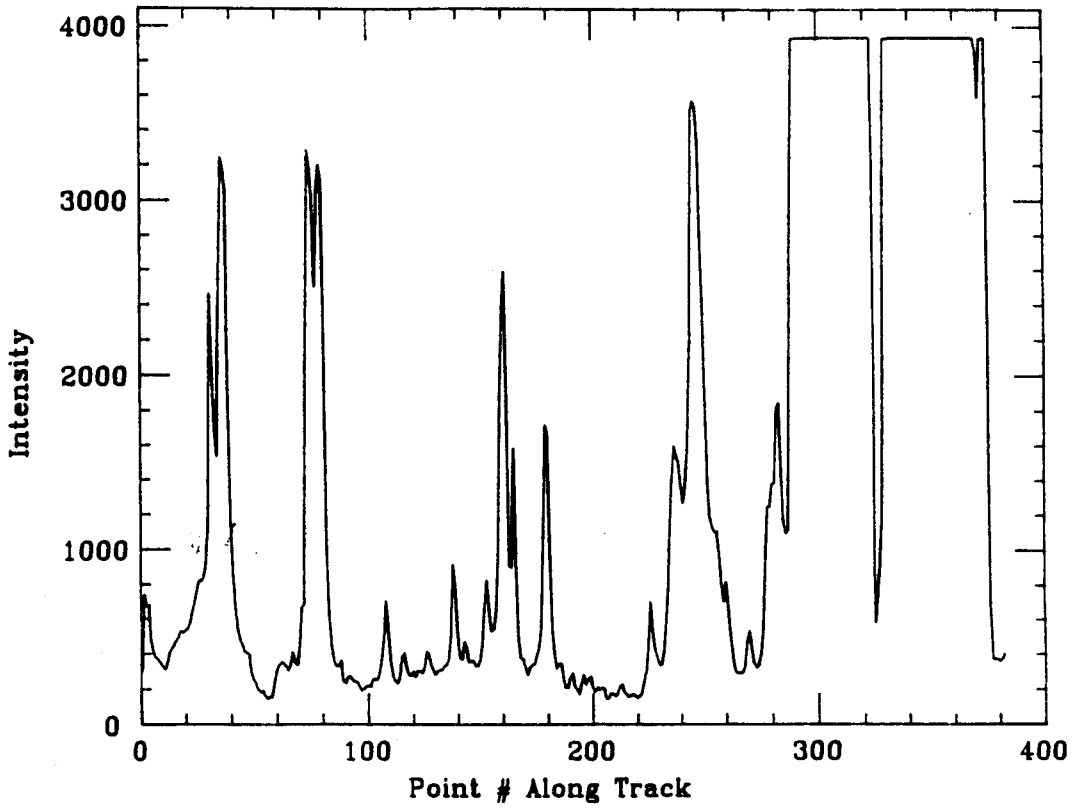

Figure 3.4.5 Intensity along a track as a function of the distance from the vertex. This illustrates an extreme case of flaring along the whole length of the track.

as dE/dx. In order to investigate this dependence, we have tried to select particles with similar velocity by analysing the fragments emitted in a narrow forward cone (±8° around the beam direction) and by plotting an intensity histogram for those tracks with rigidity around twice that of beam-velocity protons. This should select ions with M/Z=2 (deuterons and α-particles) and with velocity close to that of the beam. Under these constraints, if such leading particles indeed exist, the histogram should show two peaks of area proportional to the ion yield. The position of the peaks would correspond to the intensity of beam-velocity deuterons and α-particles. The results obtained for our 180 MeV/nucleon data are shown in figure 3.4.6 for a sample of 96 events. Here, two peaks are clearly visible, in spite of the low statistics. The areas are in a ratio of 2.7:1 and the position of the maxima suggests that the intensity varies linearly with Z.

Our criterion for estimating the normalization factors was based on the histogram in figure 3.4.6. By comparing the intensity of different types of tracks (e.g. low-intensity tracks, with rigidity corresponding to beam-velocity protons; or low- and intermediate-intensity tracks over a wider range of rigidities), different normalizations were tested. We selected the factor that gave the best separation between the deuteron and alpha peaks in this distribution.

On the basis of the information described above, we have assumed a simple expression for the intensity, $I=\text{const}\ \frac{Z}{v^x}$, where the exact dependence on the particle velocity in unknown. Since $v=\frac{Z}{M}\frac{rig}{}$, substitution for v gives:

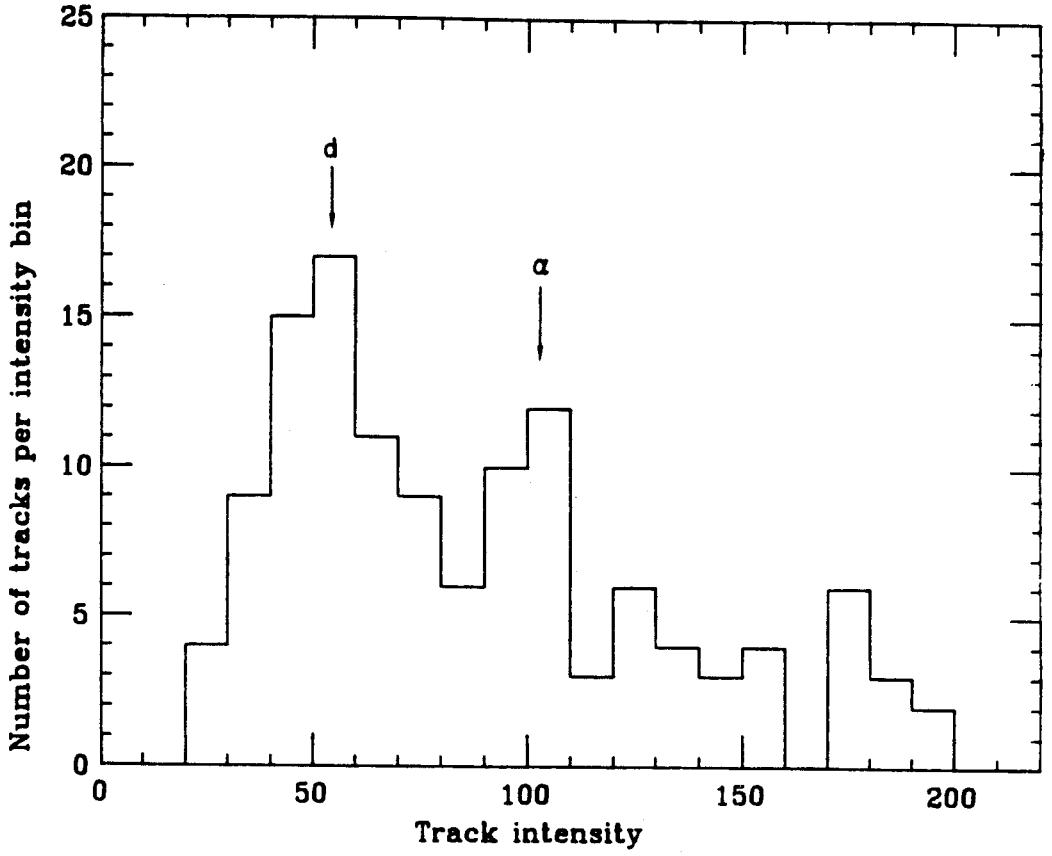

Figure 3.4.6 Intensity histogram for forward-going particles with rigidity between 1000 and 1400 MeV/c/Z. Peaks corresponding to beam-velocity deuterons and α-particles are indicated.

$$I = \text{const} * Z^{1-x} (M/rig)^{x} \qquad 3.1$$

The scatter plot obtained for rigidities and (normalised) intensities for the 180 MeV/nucleon data, including all the non-stopping tracks for 97 events, is shown in figure 3.4.7. Only intensities lower than 500 are included. The curves are calculated from expression 3.1 with x=0.5.

These curves were used to select the particle type from the plot. The percentage of various isotopes obtained with this method is given in table 3.4.1. These yields agree reasonably well with those obtained from a code like FREESCO [Fai 86], which simulates the process of statistical disassembly of a single excited source of given A, Z, volume, and excitation energy, through a statistical model. The different final states compete according to their microcanonical weights [Fai 83]. The input parameters for our calculations were a freeze-out density of 1/3 ρ_o and an excitation energy of the source of 1/2 the beam energy (the other 1/2 of the energy goes into collective effects). The largest discrepancies in table 3.4.1 are observed for large-mass fragments ($A \geq 4$). One of the reasons for the presence of a relatively higher number of heavy fragments in our data is the fact that the calculation was performed for one source of A=186 and Z=82, i.e. assuming that all the nucleons in the Nb+Nb system contribute to the excited source. This assumption is probably not true if the impact parameter is not zero. In this case, a remaining target-like source, with very low excitation, is likely to produce a few heavy fragments. The other reason rests with the uncertainty in the intensities mentioned before. Because of this, some of the apparently highly ionizing tracks are in reality tracks largely

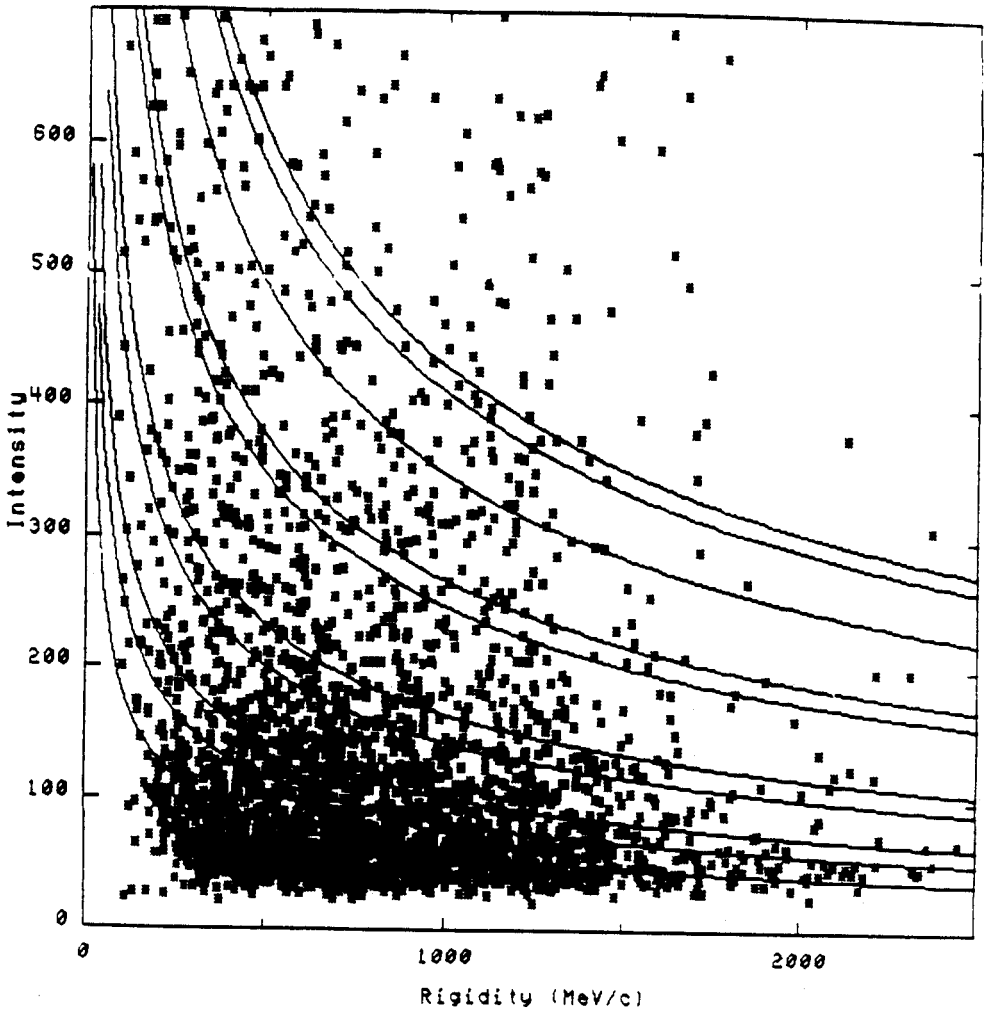

Figure 3.4.7 2-dimensional plot (intensities are corrected for the dip angle) for 97 events at 180 MeV/nucleon. The particle-identification curves shown are calculated from expression 3.1 with x=0.5.

Table 3.4.1. Percentages of various isotopes emitted in a Nb+Nb collision at 180 MeV/nucleon. The values on the left are the yields obtained from the experimental data using the curves shown in figure 3.4.7. Those on the right are calculated with the code FREESCO.

Particle	% from data	% from FREESCO
p	24.2	33.7
d	22.4	27.7
t	11.7	11.3
^{3}He	12.9	5.4
α	4.4	14.2
Li	10.9	1.2
Be	4.7	not given
B	2.7	not given
C	1.7	not given
	much smaller yields for higher masses	

obscured by flares.

In this chapter the steps in the analysis of CCD-recorded nuclear collisions have been described. Computer codes have been developed to enhance the digitised images, recognize the tracks, and calculate the tracks mean intensity. The Three View Geometric Program has been adapted to perform the spacial (three-dimensional) reconstruction of CCD-recorded events. An algorithm has been developed to identify the charge and mass of the observed fragments from the information thus extracted.

Much has been learned about the performance of our experimental set-up and the streamer chamber, and about the analysis of digitised events obtained with CCD cameras. An evaluation of the data reduction methods, and ideas for future experiments will be given in the Conclusions.

Chapter 4

EXPERIMENTAL RESULTS AND COMPARISON WITH THEORETICAL MODELS

4.1 Introduction

The experiment described in this thesis was performed at the Bevalac and utilised a ^{93}Nb beam, incident on a 220 mg/cm^2 Nb target, at two energies, 100 and 180 MeV/nucleon.

Several experiments have previously used the same system at different energies (150, 250, 400, 650, 800, and 1000 MeV/nucleon) with the Plastic Ball spectrometer as a detector [Dos 86]. Theoretical calculations are available as well, based on the nuclear fluid-dynamical model [Buc 84], the intra-nuclear cascade model [Mol 86], and the VUU theory [Mol 85].

In this chapter, the results obtained from our experiment will be described and compared with previous data and theoretical models.

4.2 Charged-particle Multiplicities

Multiplicity distributions are easily studied without having to measure the physical characteristics associated with the tracks emitted in a collision.

Low multiplicity events are usually produced in large impact-parameter collisions, where projectile and target fragmentation processes dominate. As the impact parameter decreases, fewer heavy fragments and higher charged-particle multiplicities are expected. All leading projectile fragments disappear in the limit of very central collisions. This effect is illustrated in figures 4.2.1 and 4.2.2. In the first, a CCD-recorded image of a peripheral collision is shown, where a massive

Figure 4.2.1 CCD-recorded image of a peripheral Nb+Nb collision at 180 MeV/nucleon.

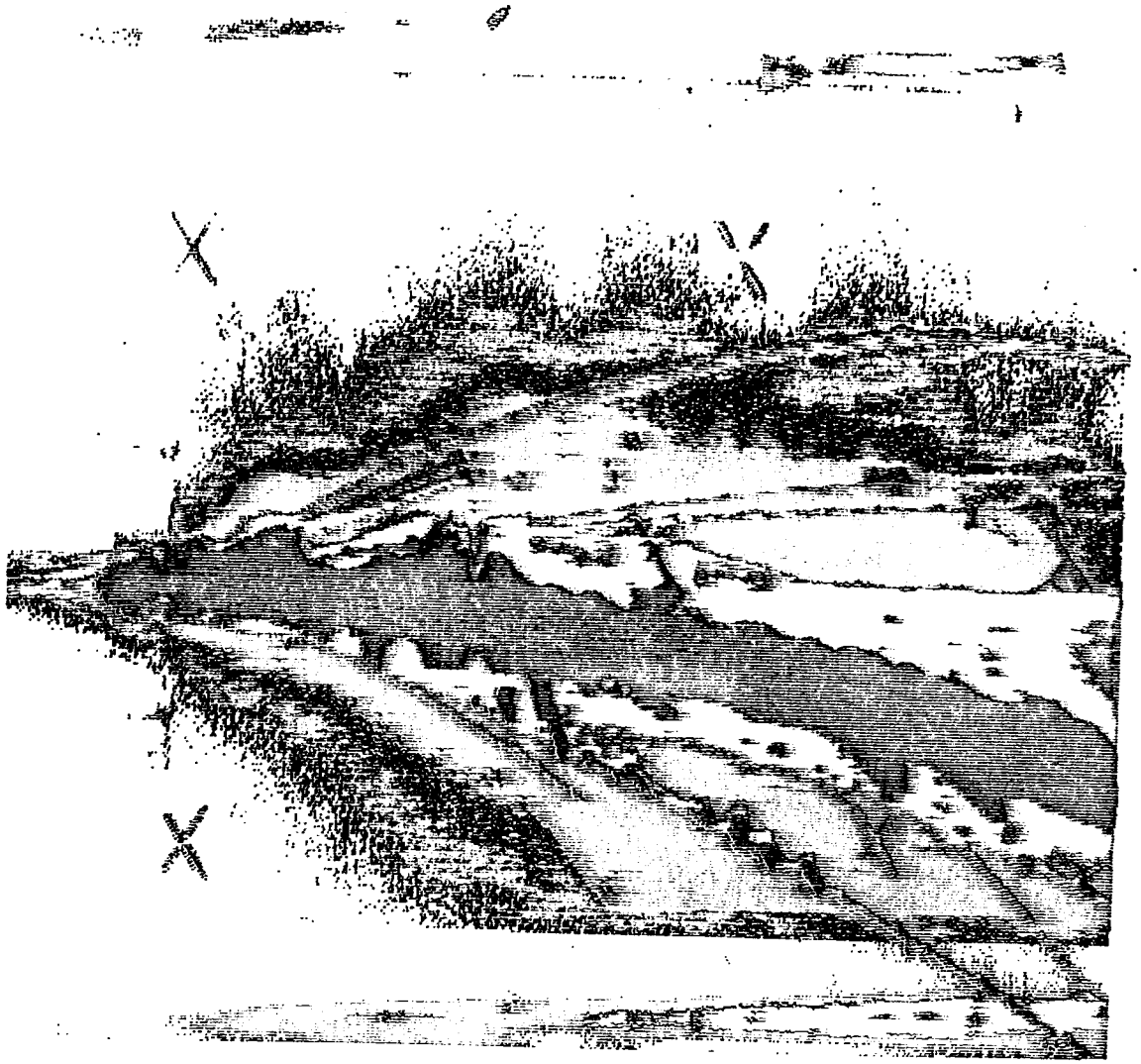

Figure 4.2.2 CCD-recorded image of a nearly-central collision at 180 MeV/nucleon.

projectile-like fragment produces a bright track, and a few light fragments are created as well. The second figure shows a nearly-central collision, where both projectile and target are completely shattered and the fragment distribution extends to backward angles.

The trigger system at the LBL streamer chamber is based on this effect. The trigger scintillator (the P-counter in figure 2.5.1) is positioned to intercept non-interacting beam particles and leading fragments in the forward cone [Lu 81]. By selecting different pulse heights in the P-counter, it is possible to trigger on events corresponding to different ranges of impact parameters, from the "unbiased" mode, where all events are accepted, to a "central" trigger which corresponds to small pulse heights in the trigger counter and selects nearly-central collisions.

For our experiment, we used the central trigger mode, thereby favouring high-multiplicity events. It has been established from comparisons between data taken in this and in the "unbiased" mode, that the central trigger is only minimally biased towards high multiplicities, within the requirement of nearly-central collisions [Hui 83].

The charged-particle multiplicity distributions for our data at 100 and 180 MeV/nucleon, each including about 300 events, are shown in figures 4.2.3 and 4.2.4. The solid lines are the result of a fit with a Poisson distribution. The centroids obtained from the fits, or mean multiplicities, are ~47 at 180 MeV/nucleon and ~34 at 100 MeV/nucleon. The fact that the experimental distributions are well fitted by a single Poisson curve indicates that the central trigger selected a relatively small range of impact parameters.

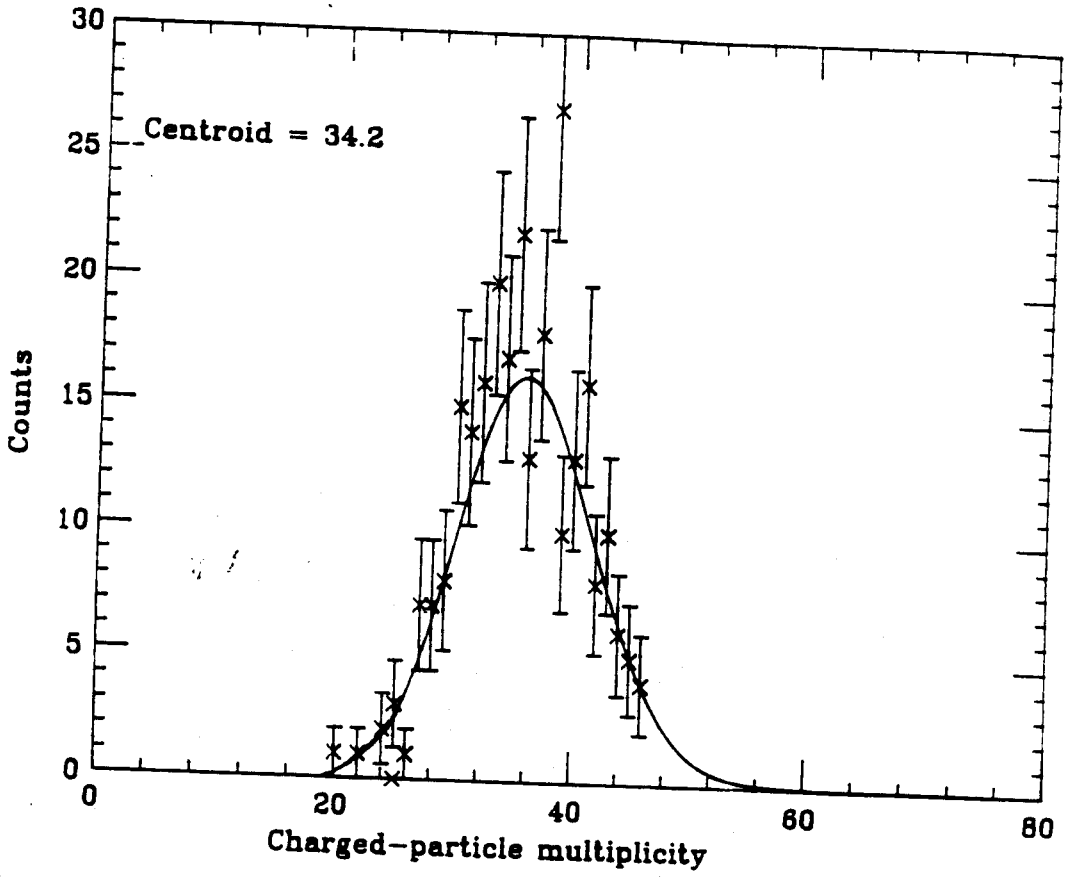

Figure 4.2.3 Multiplicity distribution for 300 events at 100 MeV/nucleon. The curve is obtained by fitting the experimental points with a Poisson distribution.

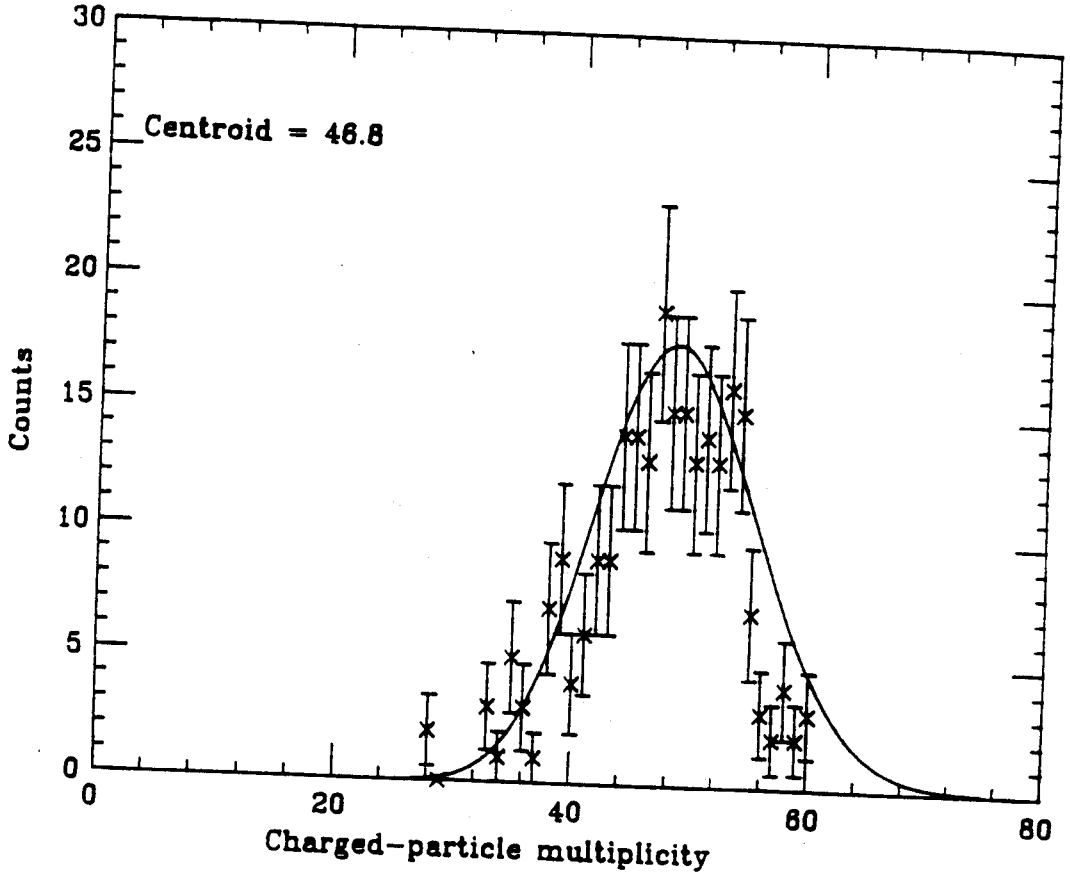

Figure 4.2.4 Multiplicity distribution for 300 events at 180 MeV/nucleon. The curve is obtained by fitting the points with a Poisson distribution.

4.3 π^- Multiplicities

The measurement of pion multiplicities has long been suggested as a useful tool to probe the nuclear equation of state [Stö 78]. Since pions are mostly created during the compression stage of the reaction, they presumably carry information about the high-density nuclear matter formed at this stage. Also, multiplicities are not much influenced by the subsequent phases of the reaction (expansion and freeze-out), unlike other variables such as angular or energy distributions.

Systematic measurements of negative pion multiplicities have been carried out at the LBL streamer chamber for the reaction Ar+KCl at energies between 0.6 and 1.8 GeV/nucleon [San 80, Sto 84, and Har 85], and La+La, at energies between 530 and 1350 MeV/nucleon [Har 87].

The pion yields decrease very rapidly at lower beam energies. For this reason, digitised and computer-scanned images of streamer chamber events could offer a distinct advantage in the measurements of π^- tracks. The curvature of these negative particles in the magnetic field of the chamber makes them easily identifiable by automatic scanning. Figure 4.3.1 shows an event where a negative pion is produced. For the measurement described here, the scanning of the images to count the negative pions was done visually, since the processing and scanning codes were being developed during the course of the analysis.

The measured π^- multiplicities, n_{π^-}, were 0.05 at 180 MeV/nucleon and 0.0099 at 100 MeV/nucleon, in both cases for about 300 events scanned. In order to compare this value with the results for Ar+KCl from [Sto 84], the π^- multiplicities must be divided by the number of participant nucleons, A. Stock et al. give the values of $\langle Q \rangle$, the mean number of participant protons, and A can be calculated from a simple

Figure 4.3.1 Nb+Nb collision at 180 MeV/nucleon, in which a negative pion is created. The particle is clearly recognizable from its curvature in the magnetic field.

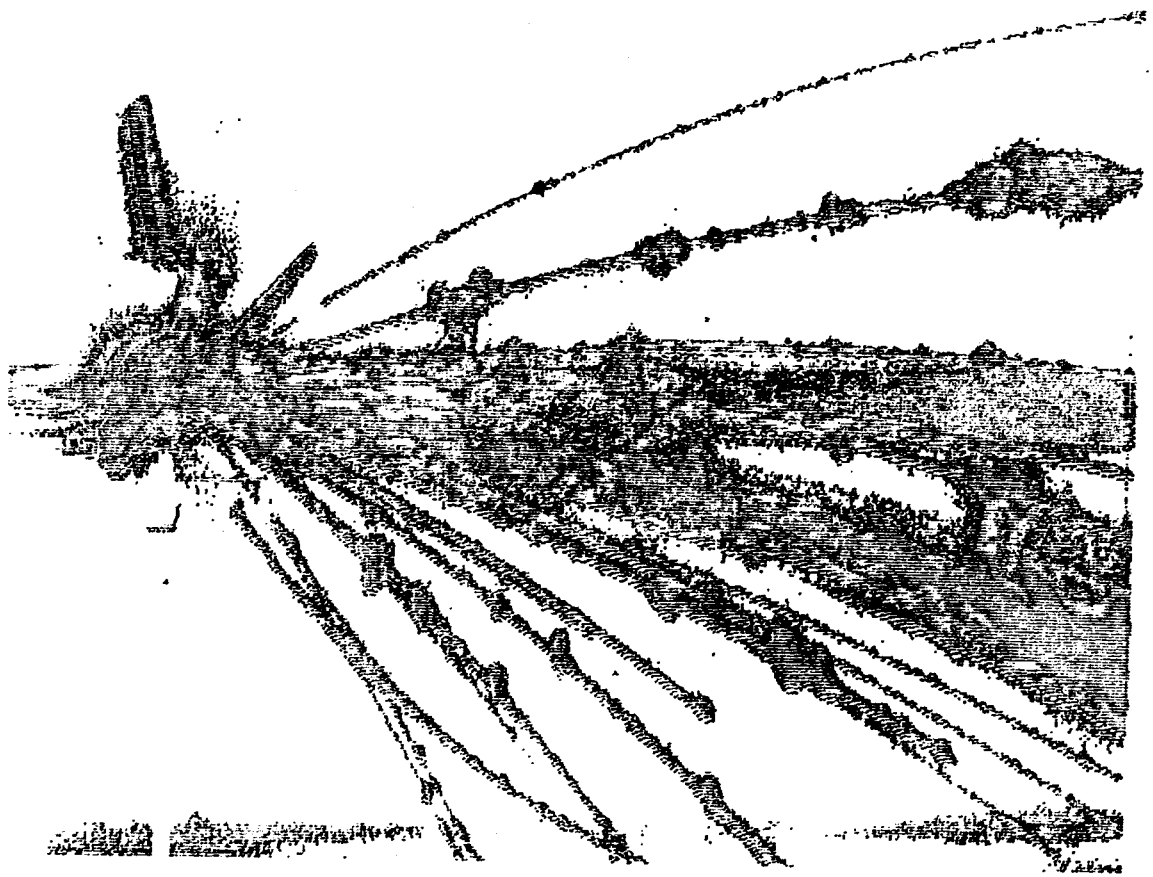

fireball geometry. In our experiment, this number was not determined. We have therefore assumed that, in the central trigger mode, a range of impact parameters between 0 and 3 fm was selected. The number of participant nucleons was then calculated from the fireball geometry for the various b, and a range of A between 128 and 186 (157±29) was found. Therefore the error bars for our points include both the statistical error on n_{π^-} and the calculated range of participant nucleons. In figure 4.3.2 the points obtained from our Nb+Nb data are compared with the systematics found for the Ar+KCl experiment.

In a recent preprint, Bonasera et al. have compared the pion yields from the Ar+KCl, La+La, and Nb+Nb reactions on the basis of a simple analytical approximation [Bon 87a].

Assuming that the pions are emitted from a source in thermal equilibrium, the number of bosons in equilibrium with a fermion gas at temperature T is given by [Lan 58]:

$$N_{Bose} = \int d\vec{r}\, d\vec{p}\, f_B(r,p) = 4\pi\beta \frac{Vg}{(2\pi h)^3} \int \frac{p^2 dp}{e^{\varepsilon/T}-1} \qquad 4.1$$

where β is a fit parameter.

For pions this expression becomes:

$$N_{\pi} = \beta \frac{2A}{3\pi} \left(\frac{r_0}{h}\right)^3 \int \frac{p^2 dp}{e^{\varepsilon/T}-1} \qquad 4.2$$

The temperature T is calculated from the beam energy in the assumption that the nucleons in the source form an ideal Fermi gas.

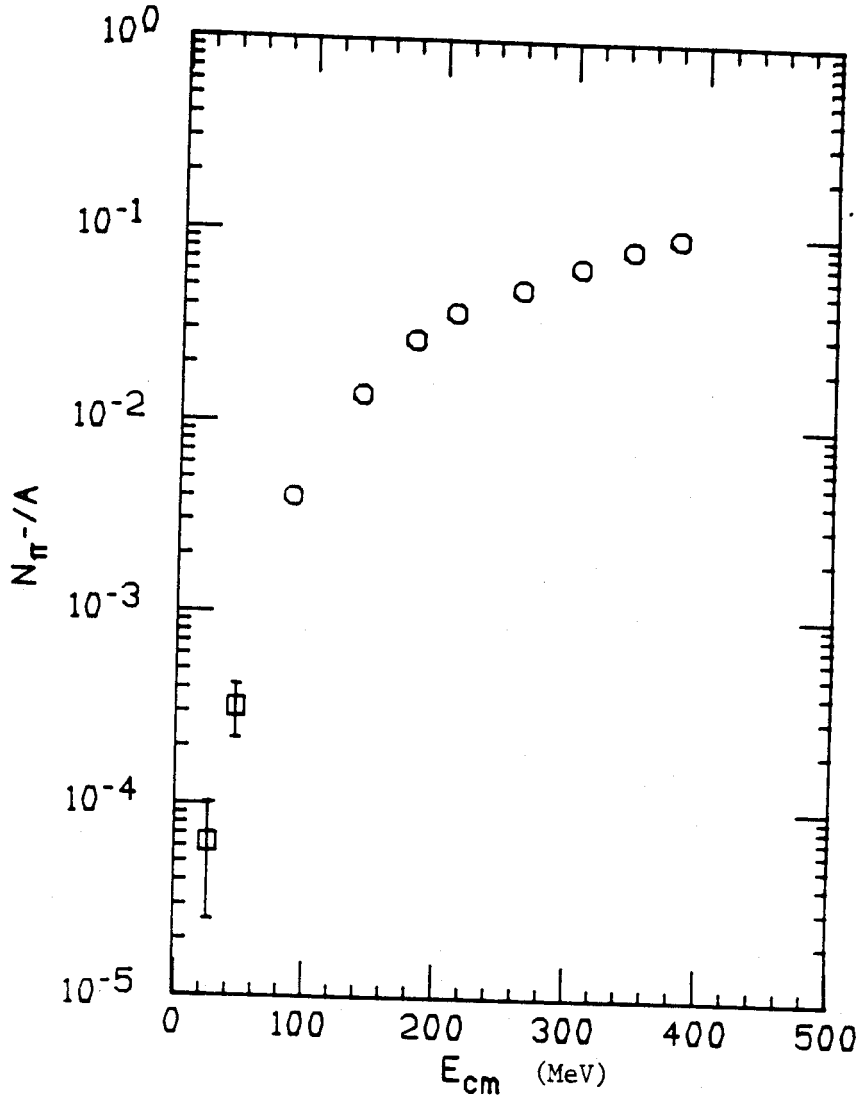

Figure 4.3.2 Negative pion multiplicities obtained from our data are compared with the values found by Stock et al. from Ar+KCl measurements [Sto 84].

For a comparison of these results, the negative pion multiplicity per participant nucleon (n_{π^-}/A) is divided by $E_{lab}^{1.5}$. The factor $AE_{lab}^{1.5}$ compensates for the multiplicity increase with increasing energy and decreasing impact parameter. The experimental yields $n_{\pi^-}/AE_{lab}^{1.5}$ are plotted in figure 4.3.3 with the curve obtained from expression 4.2 with $\beta \approx 0.16$. At high energies the scaled π^- yields tend to a constant value, but at lower energies the pion production drops considerably. This is due to the effect of the pion mass, which is no longer negligible compared to the beam energy. The experimental results are in good agreement with this prediction.

4.4 Transverse-momentum Flow Analysis

The transverse-momentum analysis recently introduced by Danielewicz and Odyniec [Dan 85] is now recognized as the most sensitive method to identify collective flow effects in experimental data.

These effects are of particular interest because, in theoretical calculations, they are associated with the compression of nuclear matter during a collision. The intra-nuclear cascade model, which lacks compression, does not predict such collective flow. The hydrodynamical model and the VUU (or BUU) theory, on the other hand, predict a sidewards flow which varies in magnitude and direction with the beam energy and the mass of the system.

Experimental results for two-particle correlations [Mey 80, Cse 82], and from exclusive measurements analysed with the sphericity tensor method [Gus 84, Ren 84] have contributed experimental evidence that such a collective flow indeed exists. But the extraction of information from

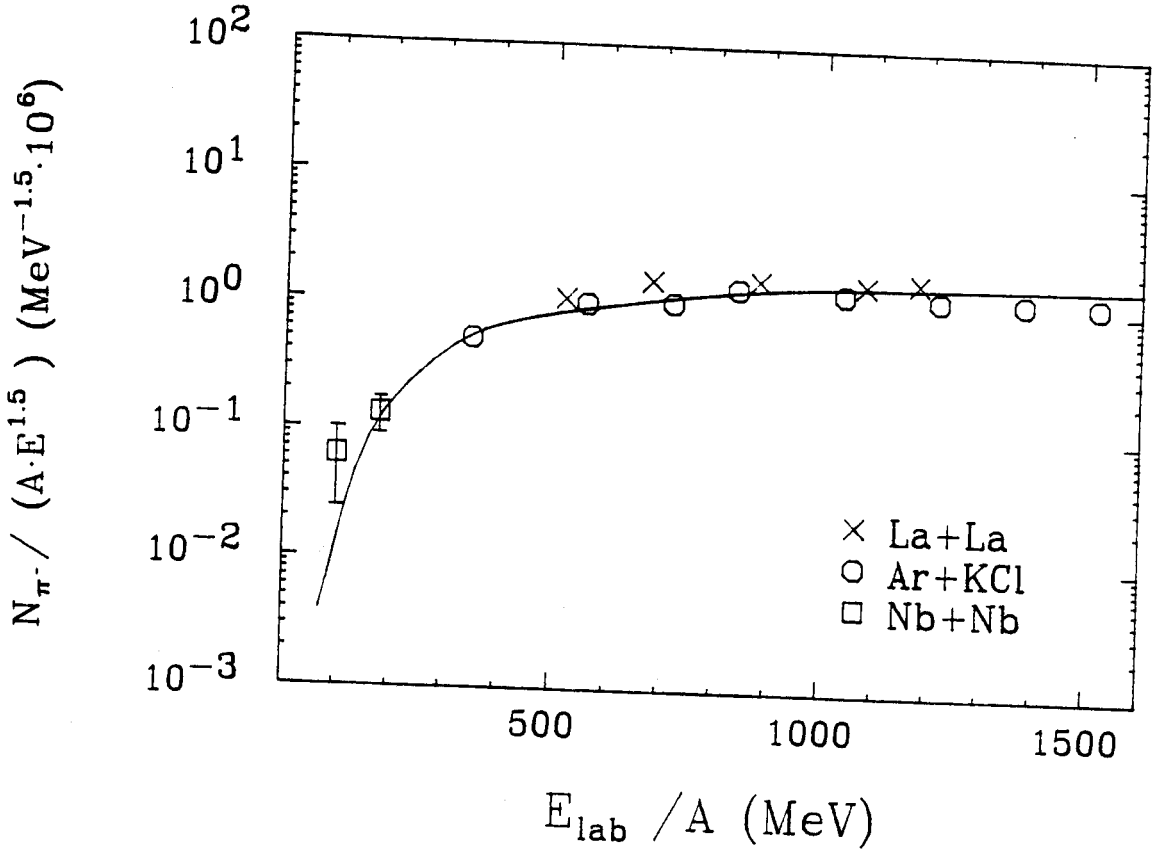

Figure 4.3.3 Scaled negative-pion multiplicities as a function of incident energy per nucleon for various systems. The curve is obtained from the analytical formula described in the text.

the data is complicated by the existence of statistical fluctuations due to the small number of particles involved [Dan 83].

The method suggested by Danielewicz and Odyniec removes some types of finite-multiplicity distortions, and has succeeded in finding evidence of collective motion in a case for which the sphericity analysis was inconclusive [Str 83].

A detailed description of the method follows. The results obtained from our data, using the computer code MOMFLOW [Cse 86a], will then be shown and compared with previous experimental results.

A. Transverse-momentum Analysis

This method involves calculating the reaction plane for each event, by defining a vector $\vec{Q}$ constructed from the transverse momenta of the particles observed in that event, $\vec{p}_\nu^{\perp}$:

$$\vec{Q} = \sum_{\nu=1}^{M} \omega_\nu \, \vec{p}_\nu^{\perp} \qquad 4.3$$

where ν is an index which runs over all the fragments in the event, and ω_ν is a weight factor defined as follows:

$$\begin{aligned} \omega_\nu &= +1 \text{ for baryons with rapidity } y_\nu > y_{cm}+\delta \\ &= -1 \text{ for baryons with rapidity } y_\nu < y_{cm}-\delta \\ &= 0 \text{ otherwise} \end{aligned} \qquad 4.4$$

By setting $\delta \neq 0$, particles around mid-rapidity, which contribute most of the unwanted statistical fluctuations, are removed from the evaluation of the reaction plane.

The goal of the calculation is to obtain the transverse momentum per nucleon projected onto the reaction plane. In order to eliminate another type of finite-multiplicity distortion in this estimate, the self-correlation term is removed from the calculation of $\vec{Q}$. An 'estimated' reaction plane is thereby obtained for each particle ν in the event:

$$\vec{Q}'_\nu = \sum_{\mu \neq \nu} \omega_\mu \vec{p}^{\perp}_\mu \qquad 4.5$$

The projected transverse momentum per nucleon of the fragment ν, evaluated with respect to this 'estimated' reaction plane, is therefore:

$$p^{x'}_\nu = \vec{p}^{\perp}_\nu \cdot \frac{\vec{Q}'}{|\vec{Q}'_\nu|} \qquad 4.6$$

When this quantity has been calculated for all the fragments in all events, its mean value , $\langle p^{x'} \rangle$, is evaluated for each rapidity bin. The obtained $\langle p^{x'} \rangle(y)$ is smaller than the 'true' average transverse momentum (projected onto $\vec{Q}$ rather than $\vec{Q}'_\nu$) by a factor of $\langle \cos \phi \rangle$, where ϕ is the azimuthal angle between $\vec{Q}$ and $\vec{Q}'_\nu$, and

$$\langle p^x(y) \rangle = \langle p^{x'}(y) \rangle / \langle \cos \phi \rangle \qquad 4.7$$

In order to estimate $\langle \cos \phi \rangle$, and also to insure that, through the above procedure, we are indeed estimating a reaction plane, each event is randomly divided into two sub-events (each containing half the observed particles). The reaction plane is then separately evaluated for each of the two sub-events. Thus, two vectors, $\vec{Q}_I$ and $\vec{Q}_{II}$, are constructed. The azimuthal angle ϕ between $\vec{Q}_I$ and $\vec{Q}_{II}$ is calculated and its distribution plotted. If a reaction plane really exists, this distribution will peak at $\phi=0$. Figure 4.4.1a shows the results obtained by Danielewicz and Odyniec for the Ar+KCl reaction at 1.8 GeV/nucleon. In figure 4.4.1b the analogous distribution is shown for Monte Carlo generated events, obtained by mixing particles from different events in the same multiplicity range. In this case, all real correlations are removed from the data and the resulting distribution is completely flat.

The value of δ in expression 4.4 is chosen to minimize the width of the azimuthal angle distribution. This width is then used as an estimate of the angle ϕ in equation 4.7.

B. Momentum Flow Analysis: Experimental Results

The results described in this section were obtained from a total of 75 events at 180 MeV/nucleon. The initial sample of 100 events was reduced by a number of selections based on:

i) Limits set on the event normalization factor. Events with a factor differing from 1 by more than 40% were excluded. Four events out of 100 were found to exceed the set limits.

ii) Charge conservation check. After the particle types were identified, the total Z in each event was calculated. If it was found to exceed 82 (the total number of protons in the Nb+Nb

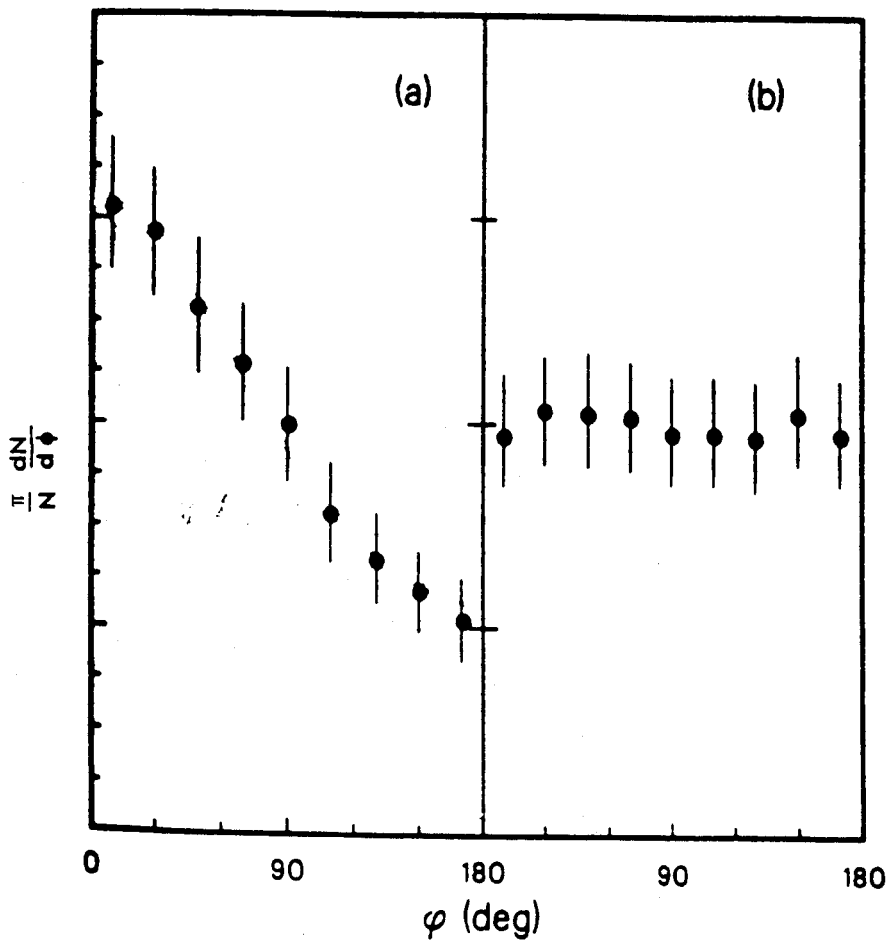

Figure 4.4.1 a) Distribution of the azimuthal angles between $\vec{Q}_I$ and $\vec{Q}_{II}$ obtained by Danielewicz and Odyniec [Dan 85] for Ar+KCl at 1.8 GeV/nucleon. b) Similar distribution for Monte Carlo generated events, in which a reaction plane does not exist.

system), the event was not included in the momentum flow calculations. Fourteen events were excluded for exceeding (usually by a few units) the total Z allowed.

iii) Energy conservation check. If the total energy of the emitted fragments was found to exceed the total energy of the beam (E_{tot}) or to be less than 1/3 E_{tot}, the event was excluded. The final energy is expected to be less than E_{tot} because 1) emitted neutrons are not detected, 2) very low energy fragments, with a range of less than about 10 cm in the chamber are not seen, and 3) only about 80% of the observed fragments were identified. 7 events out of the remaining 82 were found to be outside the set energy limits.

Figure 4.4.2 shows the distribution of the azimuthal angles between the vectors $\vec{Q}_I$ and $\vec{Q}_{II}$ for our 75 events at 180 MeV/nucleon. Except for a shoulder observed at $90° < \phi < 120°$, the curve peaks at 0° and decreases with increasing angle. The width of the distribution is about 60°. This is the value to be introduced in equation 4.7 to estimate the transverse momentum projected on the true reaction plane.

Figure 4.4.3 gives the projected transverse momenta, corrected for the deviation from the true reaction plane, as a function of rapidity, for our 180 MeV/nucleon data. The error bars include only the statistical errors. Because of detector bias, the curve is not symmetric around the origin, but the projected momentum does change from negative to positive values around zero rapidity. The center-of-mass beam rapidity is indicated in the figure.

Observing that the $\langle p^x/A \rangle$ vs. y curves can be well approximated by a straight line around mid-rapidity, where detector biases are usually less

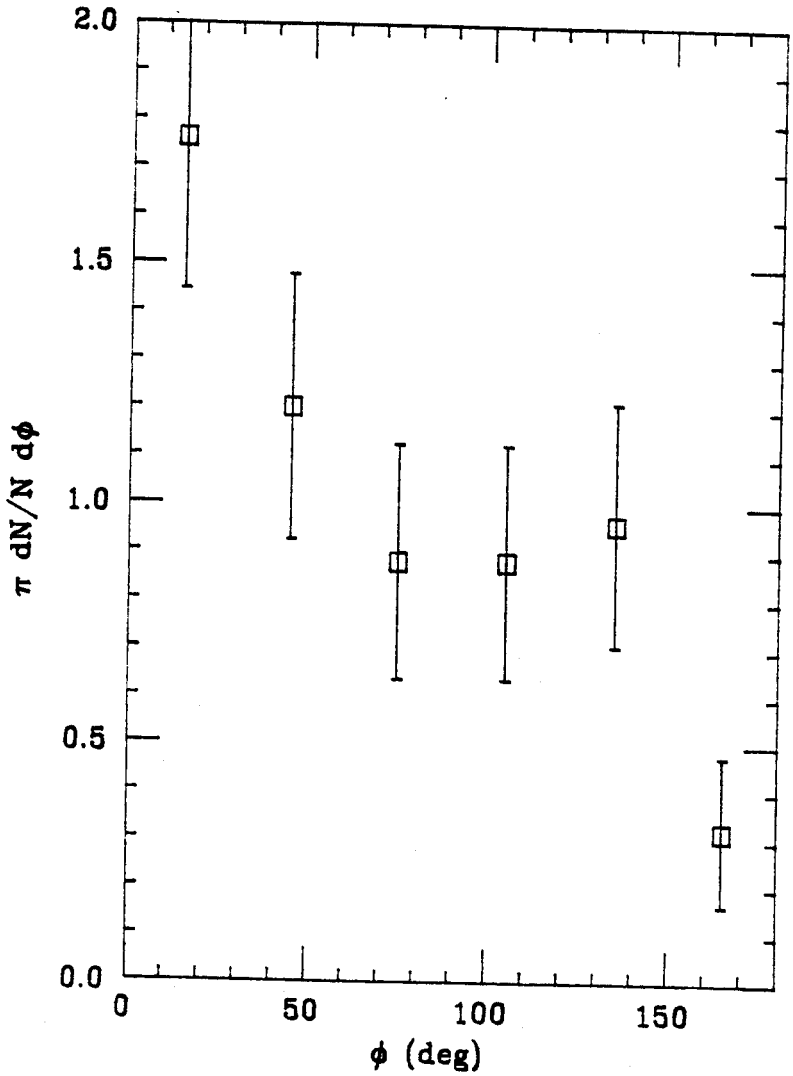

Figure 4.4.2 Distribution of azimuthal angles between $\vec{Q}_I$ and $\vec{Q}_{II}$ for 180 MeV/nucleon Nb+Nb.

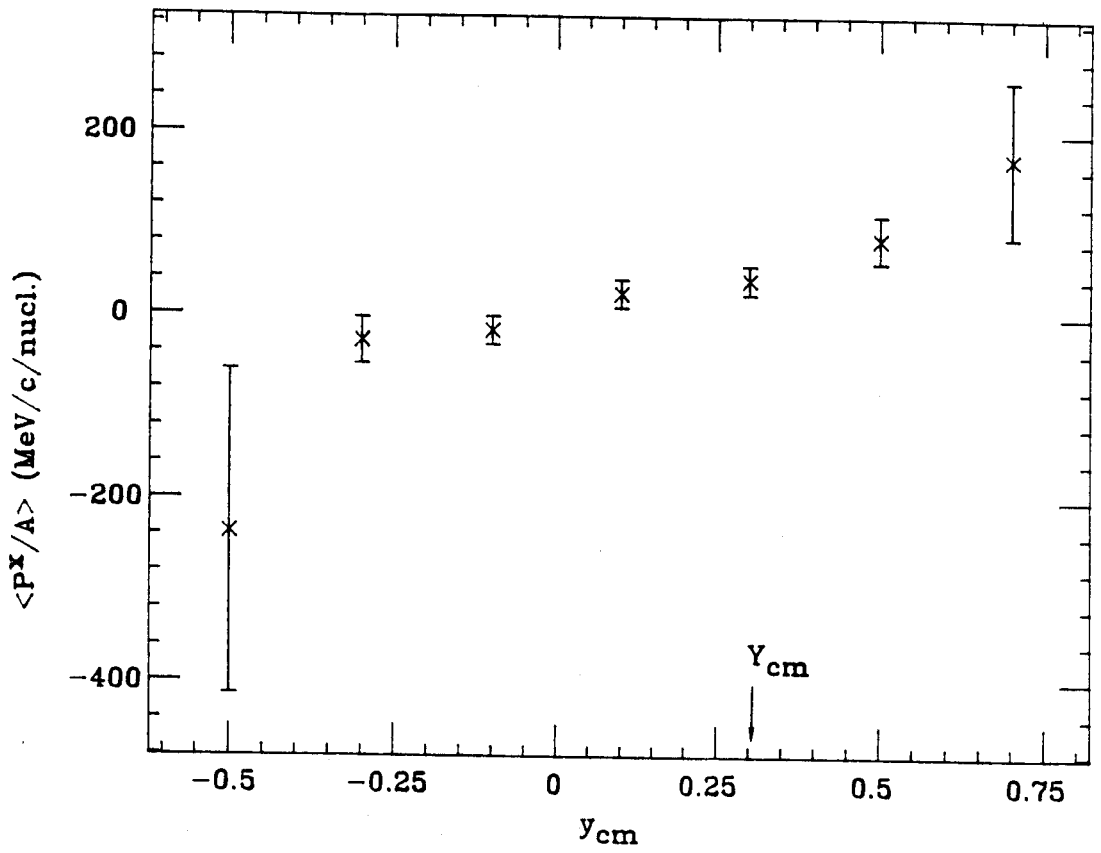

Figure 4.4.3 Mean transverse momentum per nucleon, corrected for the deviation from the true reaction plane, as a function of rapidity.

important, Doss et al. have suggested a definition of the flow as the slope of the transverse momentum distribution at mid-rapidity. In order to emphasize this fact, the experimental points can be plotted as a function of the normalised rapidity, y/y_{proj}. This plot is shown in figure 4.4.4.

A least-square fit procedure gives an intercept of 3.4±9.4, consistent with the expected value of zero, and the flow (slope of the fitted line) is 47.0±11.3 MeV/c. The value of χ^2 obtained for this fit is 0.47. The slope found by Doss et al. for their 150 MeV/nucleon Nb+Nb data is 50.0±3.0 MeV/c.

It must be stressed that, in our analysis, the slope and shape of the transverse momentum distribution were found to be relatively insensitive to small changes in the exponent x (between 0.5 and 0.8) and the normalization constant (between 65 and 80) in the curves used for the particle identification (expression 3.1).

4.5 Scaling Behaviour of Transverse Flow Variables.

The following derivation is taken from [Bal 84], [Bon 86], and [Bon 87].

The basic equations for a simple hydrodynamical description of a nuclear collision (non-relativistic and not including viscosity) are the continuity equation:

$$-\frac{\partial \rho}{\partial t} + \vec{\nabla}(\rho \vec{u}) = 0 \qquad 4.8$$

which relates the mass distribution ρ and the velocity distribution $\vec{u}$; the Euler's equation:

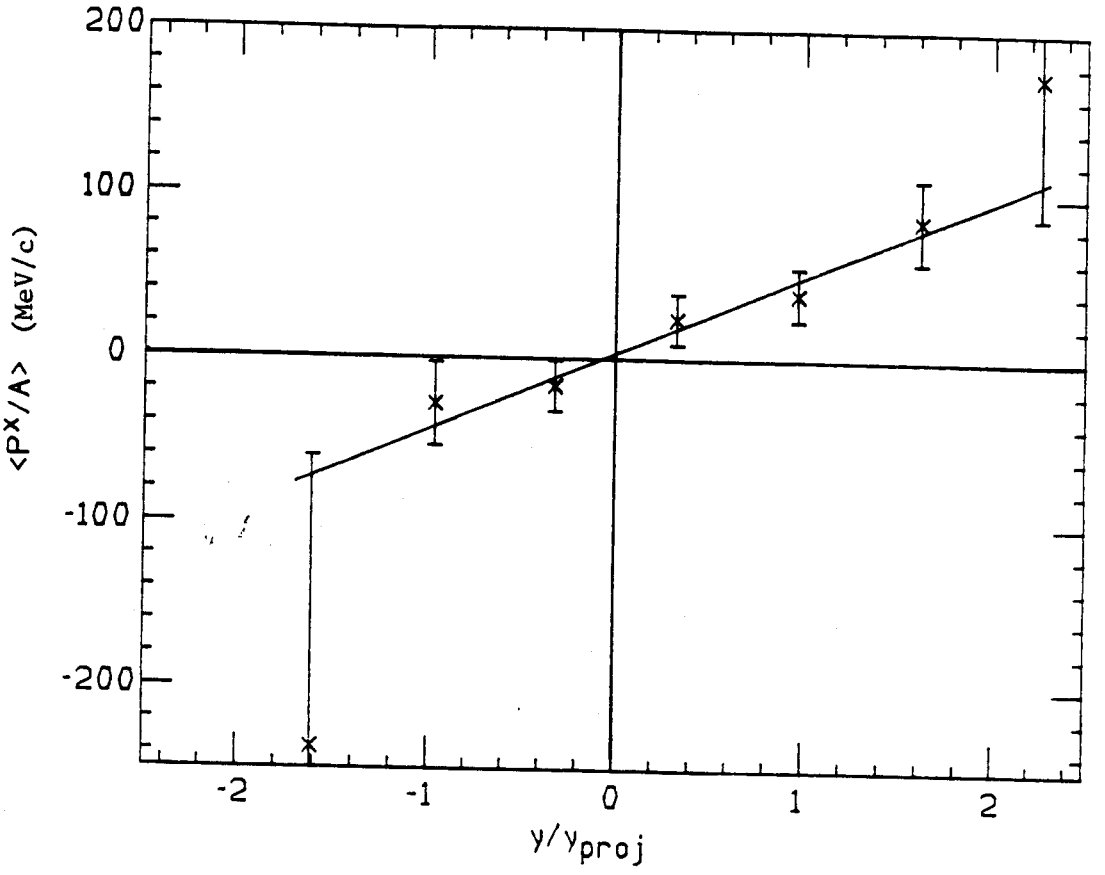

Figure 4.4.4 Mean transverse momentum per nucleon projected onto the true reaction plane, as a function of the normalized center-of-mass rapidity. The solid line is the result of a least-square fit to the experimental points, and its slope represents the flow obtained for this experiment.

$$-\frac{\partial \vec{u}}{\partial t} + (\vec{u}\cdot\vec{\nabla})\vec{u} = -\frac{1}{\rho}\vec{\nabla}P \qquad 4.9$$

and the equation of state, which relates, for instance, the pressure P. the density ρ, and the entropy per volume of the system:

$$P = P(\rho,s) \qquad 4.10$$

For a non-viscous fluid the entropy can be considered constant during the expansion, therefore

$$\vec{\nabla}P \approx (\frac{\partial P}{\partial \rho})\vec{\nabla}\rho = c^2\,\vec{\nabla}\rho \qquad 4.11$$

where c is the sound velocity.

Equations 4.8, 4.9, 4.10, and 4.11, with the initial conditions on $\vec{u}$, ρ, and s, determine the hydrodynamical evolution of the system.

In [Bal 84], the authors isolate dimensionless, scale-invariant quantities, which can be used to describe the general properties of a system, and to compare the hydrodynamical behaviour of systems of different mass and energy.

A characteristic mass, m_1, temperature T_1, length l_1, and velocity u_1 are introduced:

$$m_1 = mA \qquad 4.12$$

where m is the nucleon mass and A is the number of nucleon in the system;

$$u_1 = |\vec{u}_0| = \left(\frac{2E_0}{m}\right)^{1/2} \qquad 4.13$$

where E_0 is the initial energy per nucleon of the projectile; and

$$l_1^3 = \frac{4}{3}\pi r_0^3 A \qquad 4.14$$

which represents the volume of the system.

After introducing the definitions $\vec{r}=l_1\tilde{\mathbf{r}}$ for the radius, $t=t_1\tilde{t}$ for the time, and $T=T_1\tilde{T}$ for the temperature (where $T_1 = 2/3\ E_0$), equations 4.12, 4.13, and 4.14 are used to define dimensionless quantities, denoted by a tilde:

$$\rho(\vec{r},t) = \frac{m_1}{l_1^3}\tilde{\rho}(\tilde{r},\tilde{t}) \qquad 4.15$$

$$\vec{u}(\vec{r},t) = u_1\,\tilde{u}(\tilde{r},\tilde{t}) \qquad 4.16$$

$$T(\vec{r},t) = T_1\,\tilde{T}(\tilde{r},\tilde{t}) \qquad 4.17$$

These characteristic dimensionless hydrodynamical functions are independent of the total mass A and the energy E_0 of the system.

Now, since the sound velocity is of the same order as the thermal velocity of the nucleons, $c= u_1\tilde{c}$, with $\tilde{c}\approx 1$, the continuity and Euler's equations can be rewritten in dimensionless form:

$$m_1\left[\frac{\partial\tilde{\rho}}{\partial\tilde{t}} + S\tilde{\nabla}(\tilde{\rho}\,\tilde{u})\right] = 0 \qquad 4.18$$

$$\frac{\partial \tilde{u}}{\partial \tilde{t}} + S(\tilde{u}\cdot\tilde{\nabla})\tilde{u} = -S\tilde{c}^2 \frac{\tilde{\nabla}\tilde{\rho}}{\tilde{\rho}} \qquad 4.19$$

where $S=u_1 t_1/l_1$ is the Strouhal number.

In a small system, such as the one formed in a nuclear collision, the role of viscosity should not be neglected. Assuming that the coefficient of bulk viscosity ξ is proportional to the dynamical viscosity η, $\xi=q\eta$, where q is a dimensionless constant, and that the kinematic viscosity $\nu=\eta/\rho$ is constant during the expansion, tha Navier-Stokes equation can be written (again in dimensionless form) as:

$$\frac{\partial \tilde{u}}{\partial \tilde{t}} + S(\tilde{u}\cdot\tilde{\nabla})\tilde{u} = -S\tilde{c}^2 \frac{\tilde{\nabla}\tilde{\rho}}{\tilde{\rho}} - \frac{S}{Re}\left[\tilde{\Delta}\tilde{u} + (q+1/3)\tilde{\nabla}\,(\tilde{\nabla}\cdot\tilde{u})\right] \qquad 4.20$$

where Re is the Reynolds number: $Re=l_1 u_1/\nu$.

With a proper choice of the time scale, $t_1=l_1/u_1$, S can be set equal to 1, and the solutions of the hydrodynamical equations depend on $\tilde{r}$, $\tilde{t}$, and the Reynolds number Re. In this way, the flow patterns of systems at different energies and of different masses are similar if the Reynolds number is the same.

According to this picture, scale-invariant quantities can be defined, and a deviation from the scale invariance indicates the onset of physical processes which lead to a non-scale-invariant flow in the hydrodynamical description, such as a change in the equation of state or in the reaction mechanism.

Bonasera et al. introduce a scale-invariant transverse momentum per nucleon, defined as:

$$\tilde{p}^x = p^x / p^{CM}_{proj}$$

and a scale-invariant rapidity:

$$\tilde{y} = y^{CM} / y^{CM}_{proj}$$

In figure 4.5.1 $\tilde{p}^x$ is plotted for the experimental data obtained from Ar+KCl at 1.8 GeV/nucleon [Dan 85], La+La at 0.8 GeV/nucleon [Ren 84], Nb+Nb at 400 MeV/nucleon [Dos 86 and Rit 85], and for our 180 MeV/nucleon Nb+Nb measurement. Some differences are expected, due to different multiplicity selections, different types of particles detected, and different detector bias. In spite of this, the various curves show remarkably similar behaviours, especially for y/y_{proj} greater than -0.5. At lower rapidities the different biases of the various detectors cause a rather large spread in the values found for the transverse momenta.

As seen in section 4.3, Doss et al. [Dos 86] have introduced a parameter F, which they have named 'flow', defined as the slope of the transverse momentum vs. rapidity curve at mid-rapidity. This parameter, as a measure of the transverse flow, is less influenced by statistical fluctuations or detector bias than, for instance, the maximum of the curve. Bonasera et al. define a scale-invariant flow, $\tilde{F}$, as:

$$\tilde{F} = F / p^{CM}_{proj}$$

In figure 4.5.2 the points for the experiments listed in table 4.5.1 are shown, together with the $\tilde{F}$ = const contour lines, in the A, E_{CM} plane. As was mentioned in the introduction, in [Bon 86] the behaviour of the

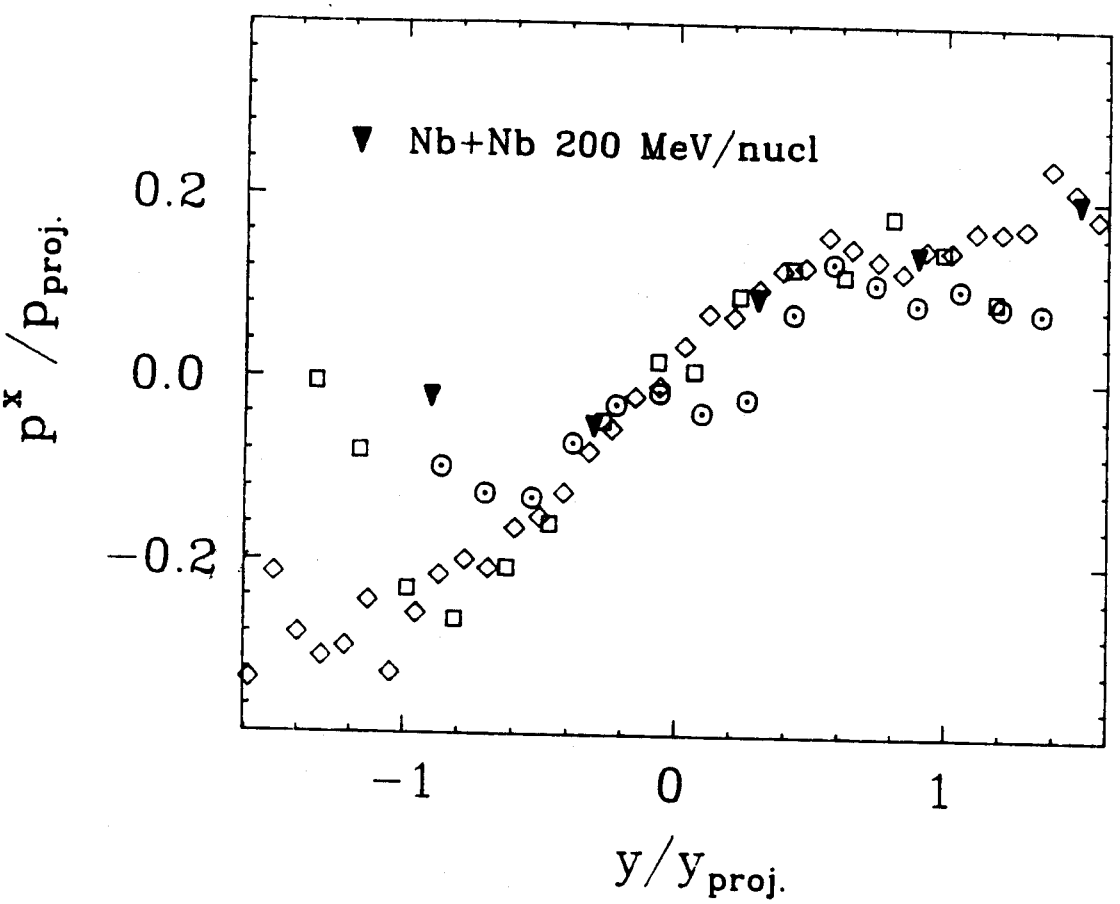

Figure 4.5.1 Scale-invariant transverse momentum vs. scale-invariant rapidity for Ar+KCl at 1.8 GeV/nucleon (circle) [Dan 85], La+La at 0.8 GeV/nucleon (diamond) [Ren 84], Nb+Nb at 0.4 GeV/nucleon (square) [Dos 86 and Rit 85], and Nb+Nb at 180 MeV/nucleon (black triangles). From [Bon 86].

Table 4.5.1. Flow measured from different experiments, and the corresponding scale-invariant quantity, $\tilde{F}$ (from [Bon 86]).

lab. E (MeV) proj.	CM E (MeV) nucl.	A	F (MeV/c)	CM p (MeV/c) proj.	Ptcl.	$\tilde{F}$	ref.
150	37	197	82	265		.310	[Dos 86]
200	49	197	120	306		.391	[Dos 86]
210	51	197	115	314	H	.37	[Bec 85]
210	51	197	157	314	He	.35	[Bec 85]
210	51	197	220	314	Li	.35	[Bec 85]
250	61	197	132	343		.385	[Dos 86]
400	96	197	160	433		.368	[Dos 86]
650	150	197	162	552		.293	[Dos 86]
800	182	197	151	613		.247	[Dos 86]
800	182	139	170	613	d	.23	[San 84]
150	37	93	50	265		.188	[Dos 86]
180	44	93	47±11	291		.16±.04	
250	61	93	102	343		.299	[Dos 86]
400	96	93	130	433		.301	[Dos 86]
650	151	93	140	552		.254	[Dos 86]
800	182	93	136	613		.222	[Dos 86]
1050	233	93	122	702		.173	[Dos 86]
400	96	40	76	433		.175	[Dos 86]
800	182	40	140	613	d	.19	[San 84]
1050	233	40	72	702		.102	[Dos 86]
1200	263	40	100	750		.13	[Dan 85]
1800	375	40	140	919		.15	[Dos 86]

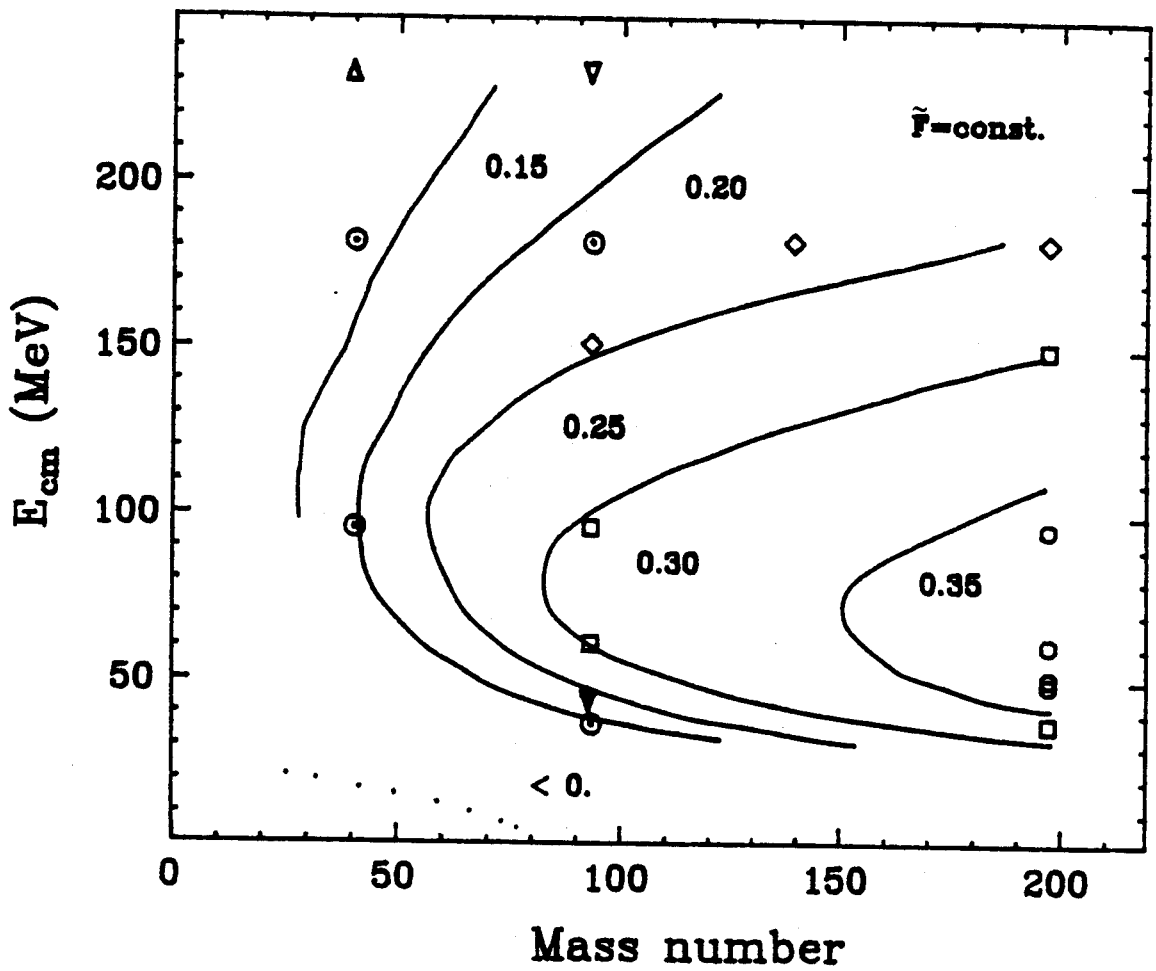

Figure 4.5.2 Contour lines in the A,E_{cm} plane for $\tilde{F}$=constant. The dotted curve represents the prediction for low energies. The various symbols refer to the experimental values of $\tilde{F}$ listed in table 4.5.1: ◇ for $0.4<\tilde{F}<0.325$, □ for $0.325<\tilde{F}<0.275$, ◊ for $0.275<\tilde{F}<0.225$, ⊙ for $0.225<\tilde{F}<0.175$, ▽ for $0.175<\tilde{F}<0.125$, △ for $0.125<\tilde{F}<0.1$ [Bon 86].

experimental $\tilde{F}$=const. lines are compared with the curves of constant Reynolds number in the same A,E_{CM} plane (refer to figure 1.2.8a). The point added for our system falls between the $\tilde{F}$= 0.20 and the $\tilde{F}$=0.25 lines, while our estimated value of $\tilde{F}$ is slightly lower, $\tilde{F}$=0.16±0.04. It must be noticed that, in this region of the A,E_{CM} plane, the $\tilde{F}$=const lines are very close together and an unambiguous attribution of the experimental points to one or another of them is especially difficult.

Chapter 5

CONCLUSIONS

5.1 Evaluation of the System.

In this concluding chapter, an evaluation of the system (CCD's and streamer chamber), of the analysis programs, and of the difficulties encountered in extracting results from our data will be made. The limitations and advantages of our CCD-camera system will be described and possible improvements discussed.

A. Electronics and Data Acquisition.

The CCD system we have developed is the first of its kind to have been used in a streamer chamber experiment.

Several challenges were faced, from the necessity of a reasonably fast data acquisition rate to the development of all the analysis software for the digitised images. Some of these problems have been successfully solved, in others much useful insight has been gained. This has led to plans for improving and updating the system.

During the experiment, our CCD cameras and electronics performed very well, allowing us to record events at a rate of about one per beam spill. Considering the amount of data that has to be read out and recorded for each event, this can be regarded as a rather fast acquisition rate.

The main problem found in interpreting our data was that of obtaining a reliable particle identification. This is a very important step in the analysis, and it still remains to be shown unambiguously that

CCD cameras can improve the particle identification capability of the streamer chamber.

One of the principal problems encountered in the present data was the poor performance of the streamer chamber during the experiment. Difficulties in regulating the SF_6 pressure and the high-voltage pulse forced us to run at higher voltages than desired, thus producing rather poor-quality images, with tracks often obscured by large flares. The fixed position of the target and of the trigger scintillators made it impossible to tune the beam into the chamber with high magnetic fields, so that the curvature of the high-energy tracks was extremely small, and the errors in the evaluation of their rigidity rather large. All of these factors were out of our control for the experimental run.

The LBL streamer chamber has recently been modified by narrowing the Blumlein gap. This will allow running the chamber at considerably lower voltages than those obtainable during our previous experiment. This fact alone should help in two ways: one, by reducing the flaring it should make estimation of the intensities less uncertain; two, by operating the chamber closer to the avalanche mode a better proportionality should be obtained between intensity of the emitted light and energy loss. Another advantage would be that of smaller pulse-to-pulse variations, and of a reduced effect of these variations on the light output, making the event-to event intensity normalization less important.

Naturally, the price to pay for the advantages of low-voltage operation is a loss in track brightness. It is possible that CCD's alone are not sensitive enough to record the dim tracks that will be produced in this way. The use of image intensifiers could offer a solution to this problem, and this possibility is currently under study.

B. Analysis Software.

All the steps of the analysis have now reached a good degree of automation, with the exception of the track-recognition code. It is clear at this stage that the amount of operator intervention in this part of the analysis depends strongly on the quality of the images and on the event multiplicity. Typically, the time required to correct and complete the track recognition of an event at 180 MeV/nucleon, with an average multiplicity of almost 50 tracks, was between 15 and 20 minutes. For a 100 MeV/nucleon event (average multiplicity ≈35, and usually fewer flares) it was reduced to about 5 to 10 minutes. Improvements on the track-recognition code, which is at the present time the biggest obstacle to a completely automatic and fast event analysis, are being studied.

A more sophisticated approach to the intensity analysis, including peak fitting at each point along the tracks, is being investigated. Currently, this appears to be a very time-consuming method, and its usefulness has not been demonstrated; but the use of faster routines and/or more powerful computers might answer the first objection, and allow a more rigorous evaluation of the method.

5.2 Concluding Remarks.

In conclusion, the development of a CCD system to record heavy-ion collisions in a streamer chamber has been successfully accomplished. In the process of analysing the data collected with this system, much experience has been gained on streamer chamber operations, characteristics of our system, and what modifications and improvements are necessary for future experiments.

Only limited nuclear physics results were extracted from our data, because of the impossibility of obtaining a satisfactory particle identification. Nevertheless, interesting results were obtained about pion yields in intermediate-energy reactions, where information was lacking, and a complete momentum-flow analysis has been accomplished at one energy.

The particle identification was the main problem encountered in the analysis, and suggestions have been made that should help overcome this limitation.

It appears that the sensitivity of the system can be increased, and the streamer chamber performance improved. A successful solution to these problems should make our CCD system a useful tool for investigating heavy-ion collisions, especially in the low to intermediate energy region, where charged-particle multiplicities do not exceed 50-60. Interesting effects, such as a phase transition and changes in the reaction mechanism are predicted in this energy range, even for relatively low-mass systems (refer to figure 4.5.2). Experimental data are needed to verify the theoretical predictions and expand our understanding of nuclear matter in its various states.

APPENDIX A

Appendix A

PROGRAM CCDSTREAM

```
            SECTION 8
BKGND       EQU     $06E000     FIRST LOCATION OF BACKGND STORAGE AREA
DATA        EQU     $001500     FIRST LOCATION OF DATA STORAGE AREA
FFRAME      EQU     $106C08     FIRST LOC FOR PROCESSED FRAME
BITMSK      EQU     $100000     DUAL-PORTED MEM INITIAL ADDRESS (FOR BITMASK)
PIX         EQU     $00D7FF
PIXELS      EQU     $001800
COMND       EQU     $FFFC00
PHOTO       EQU     $FFFC02
CONTRIN     EQU     $FFFC06
CONTROUT    EQU     $FFFC04
ROC         EQU     $FF8000
COM         EQU     $0003               4 COMMANDS WILL BE ENTERED
NEWFRAME
            LEA     CONTRIN,A6
            LEA     COMND,A0
            LEA     PHOTO,A3
            LEA     DATA,A1
            MOVE.W  #$7FFF,D3           SET TIMER
FASTCL      MOVE.W  (A6),D4
            BTST.L  #13,D4              CHECK READY BIT
            DBNE    D3,FASTCL
            TST.W   D3
            BLT     ERROR
            MOVE.W  #$0007,(A0)         SEND 'FAST CLEAR'
            CLR.B   FIRST               Clear the first time flag.
            TST.B   FIRST               If first time then skip.
            BEQ     FIFOIN              ...
ENDTRIG     MOVE.W  CONTRIN,D7          Get trigger...
            BTST    #7,D7               if still on then...
            BEQ     ENDTRIG             Loop until it goes away...
FIFOIN
            MOVE.B  #-1,FIRST
            MOVE.W  (A6),D7             !Before taking a new picture,
            BTST.L  #0,D7               ! check if FIFO's are in
            BNE.S   ONE1                ! synchronism...
            BTST.L  #1,D7               !...first FIFO IN...
            BNE     ERRMESS
            BTST.L  #2,D7
            BNE     ERRMESS
            BRA     FIFOOUT
ONE1
            BTST.L  #1,D7
            BEQ     ERRMESS
            BTST.L  #2,D7
            BEQ     ERRMESS
FIFOOUT
            BTST.L  #3,D7               !...then FIFO OUT...
            BNE.S   ONE2
            BTST.L  #4,D7               !If they are not, print
            BNE     ERRMESS             ! error message.
            BTST.L  #5,D7
            BNE     ERRMESS
            BRA.S   CHECKSR             !If they are, start testing
ONE2
            BTST.L  #4,D7               ! for correct bit pattern.
            BEQ     ERRMESS
            BTST.L  #5,D7
            BEQ     ERRMESS
CHECKSR
```

```
        MOVE.W   (A6),D7          !Test bit pattern
        BTST.L   #12,D7
        BEQ.S    EXTRA
        BTST.L   #13,D7
        BEQ.S    EXTRA
        BTST.L   #14,D7
        BEQ.S    EXTRA
        BTST.L   #15,D7
        BNE.S    EXTRA            ! FIFO and test again...
        BRA      READY            ! else, take picture.
EXTRA
        MOVE.W   (A3),(A1)
        LEA      BJUNK,A5
        LEA      EJUNK,A6
        MOVE.B   #227,D7
        TRAP     #14
        BRA      FIFOIN
READY
        MOVE.W   #4,CONTROUT       SET READY LIGHT AND CLEAR BUSY
BEAMON
        MOVE.W   CONTRIN,D7        Look at beam...
        BTST     #6,D7
        BNE      BEAMON            Loop until on...
        MOVE.W   #2,CONTROUT       Set amber waves of lights.

        MOVE.W   #$7FFF,D3
        MOVE.W   #COM,D0
        LEA      TABLE,A2
EXPOSE
        MOVE.W   (A6),D4
        BTST.L   #13,D4
        DBNE     D3,EXPOSE
        TST.W    D3
        BLT      ERROR
        MOVE.W   (A2)+,(A0)
        DBRA     D0,EXPOSE

WTRIG
        MOVE.W   CONTRIN,D7        Look at beam..
        BTST     #7,D7             If EVENT there...
        BEQ.S    TAKE1             Take event.
        BTST     #6,D7             If spill gone then
        BNE      NEWFRAME          Wait for it to happen.
        BRA.S    WTRIG             Loop until state changes.
TAKE1
        MOVE.W   #$81,CONTROUT     Set red and busy.

        MOVE.L   #PIX,D1
        MOVE.L   #PIX,D2
        LEA      DATA,A1
        MOVE.L   #PIX,D6
        MOVE.L   #PIX,D5

        MOVE.W   #$7FFF,D3         Load timeout count.
WTREAD  MOVE.W   (A6),D4           Get status of camera ctller.
        BTST.L   #13,D4            Check the ready bit.
        DBNE     D3,WTREAD         Loop until timeout or change.
        TST.W    D3                Check for loop count expiration
        BLT      ERROR             And complain about timeouts.
        MOVE.W   #$2002,(A0)       Start read.
```

```
AREAD       MOVE      (A3),(A1)+          READ DATA FROM CCD
            DBRA      D1,AREAD
BREAD       MOVE.W    (A3),(A1)+
            DBRA      D2,BREAD
CREAD       MOVE.W    (A3),(A1)+
            DBRA      D6,CREAD
DREAD       MOVE.W    (A3),(A1)+
            DBRA      D5,DREAD
            MOVE.W    #$7FFF,D3
CLEAR
            MOVE.W    (A6),D4
            BTST.L    #13,D4
            DBNE      D3,CLEAR
            TST.W     D3
            BLT       ERROR
            MOVE.W    #$0007,COMND          START FAST CLEAR
            LEA       BKGND,A2
            LEA       DATA,A1
            LEA       FFRAME,A5
            LEA       BITMSK,A4
            LEA       ROC,A0
            MOVE.L    #PIXELS,D1
VAX
            MOVE.B    6(A0),D0
            BTST      #0,D0
            BEQ       VAX
            MOVE.W    #0,(A4)+
            MOVE.W    #0,(A4)+
            MOVE.W    #384,(A4)+    ARRAY SIZE
            MOVE.W    #576,(A4)+
INIT
            MOVE.L    #31,D5        BIT COUNTER
            CLR.L     D0            CLEAR BIT MASK
START
            MOVE.W    (A1)+,D7      LOAD DATA IN REGISTER
            SUB.W     (A2)+,D7      SUBTRACT BACKGROUND
            BLE       NEXTBIT       IF <THRESHOLD DISCARD
            MOVE.W    D7,(A5)+      OTHERWISE KEEP AND
            BSET      D5,D0         SET CORRESPONDING BIT

NEXTBIT     SUBQ.L    #1,D5         LAST PIXEL ?
            BGE       START
            MOVE.L    D0,(A4)+       IF BITMSK COMPLETED, LOAD IN MEM. AND
            SUBQ.L    #1,D1            DECREMENT BITMASK COUNTER
            BGT       INIT
            MOVE.L    A5,D0
            SUB.L     #$100000,D0
            ASR.L     #1,D0
            MOVE.L    D0,$1404
            MOVE.W    D0,(A0)
            MOVE.W    D0,$1400
            ASR.L     #8,D0
            ASR.L     #8,D0
            MOVE.B    D0,3(A0)
            MOVE.B    D0,$1403
            MOVE.W    #0,4(A0)
            MOVE.B    #0,7(A0)
            BRA       NEWFRAME
ERROR:
        LEA       MESS,A5
```

```
            LEA       MEND,A6
            MOVE.W    #227,D7
            TRAP      #14
            MOVE.W    #228,D7
            TRAP      #14
MESS:
            DC.L      'TIME'              TIME OUT ERROR MESSAGE
            DC.L      'OUT '
            DC.L      'ERRO'
            DC.L      'R   '
MEND:
ERRMESS:
            LEA       MBEG,A5
            LEA       MSTOP,A6
            MOVE.B    #227,D7
            TRAP      #14
            BRA.S     ERRMESS
MBEG:
            DC.L      'FIFO'
            DC.L      ' S O'
            DC.L      'UT O'
            DC.L      'F SY'
            DC.L      'NCH '
            DC.L      '!!!!'
            DC.L      'PLEA'
            DC.L      'SE R'
            DC.L      'ESET'
            DC.L      ' SYS'
            DC.L      'TEM.'
MSTOP:
BJUNK:
            DC.L      'READ'
            DC.L      ' ONE'
            DC.L      ' EXT'
            DC.L      'RA W'
            DC.L      'ORD '
EJUNK:
TABLE:
            DC.W      $0008               COMMAND TABLE
            DC.W      $0009
            DC.W      $08FA                  384/2-1
            DC.W      $08FB                  576/4-1
FIRST       DC.W      0                      First time through flag.
            END
```

APPENDIX B

Appendix B

Sources of Background Noise in CCD's

There are several sources of noise that can affect the performance of a CCD camera system.

One type of background is due to the production of thermal electrons (free electrons produced by thermal energy in the silicon lattice), which cannot be distinguished from electrons liberated by photons. The dependence of this 'dark current' on the temperature of the CCD is shown in figure B.1. While the dark current will saturate the CCD in about 1 second at a temperature of 25° C, it will take about 3 minutes to reach saturation at -40° C. Therefore, an almost insignificant amount of thermal background is generated during a 0.5 second exposure when the devices are cooled, as was the case during the experiment described here.

An invariant type of noise, which has the effect of somewhat reducing the dynamic range of the CCD's, is the system noise. This is produced in the preamplifier, and appears as an essentially constant background, independent of temperature or exposure time.

Figure B.2 shows the dark field per pixel (the digitized value, averaged over 512 pixels), as a function of exposure time, measured at two different temperatures. The contributions due to the system offset and the thermal background can be seen as the intercept and the slope of the lines. The graph also shows that, with cooled CCD's and an exposure time of 0.5 sec, the dark current constitutes a very small percentage of the total background.

Other sources of error in a photometric measurement are the presence of dead or saturated pixels, whose number is very small in a high-quality

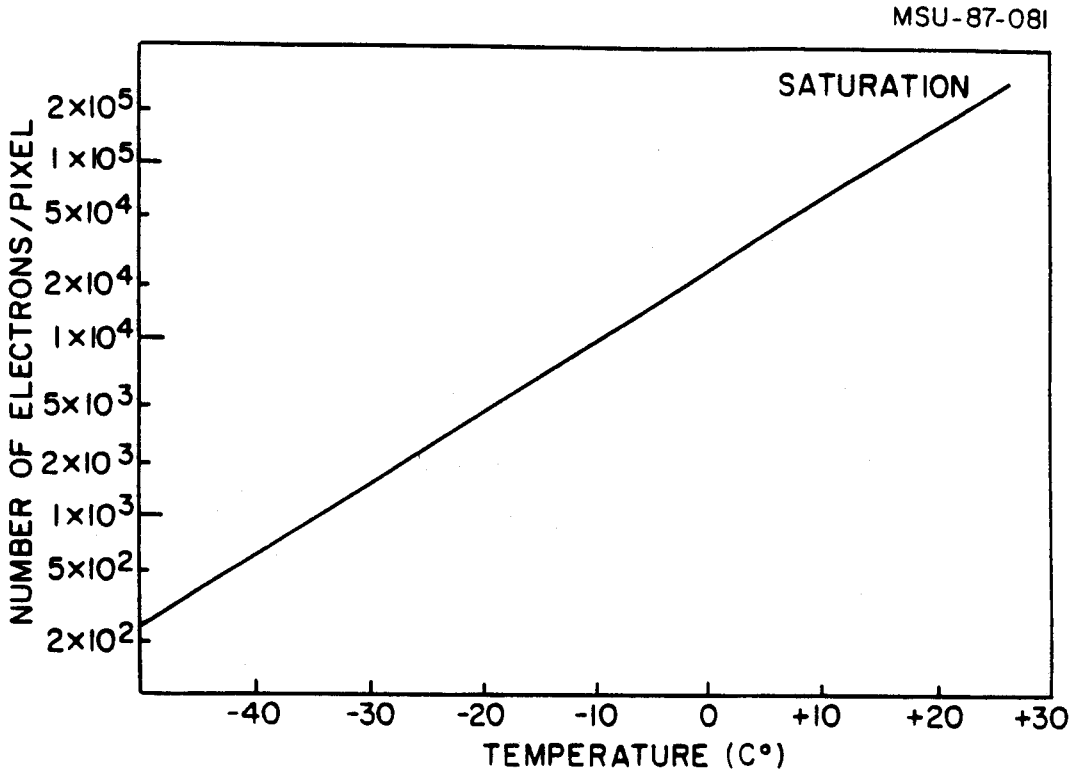

Figure B.1 Dark current vs. temperature.

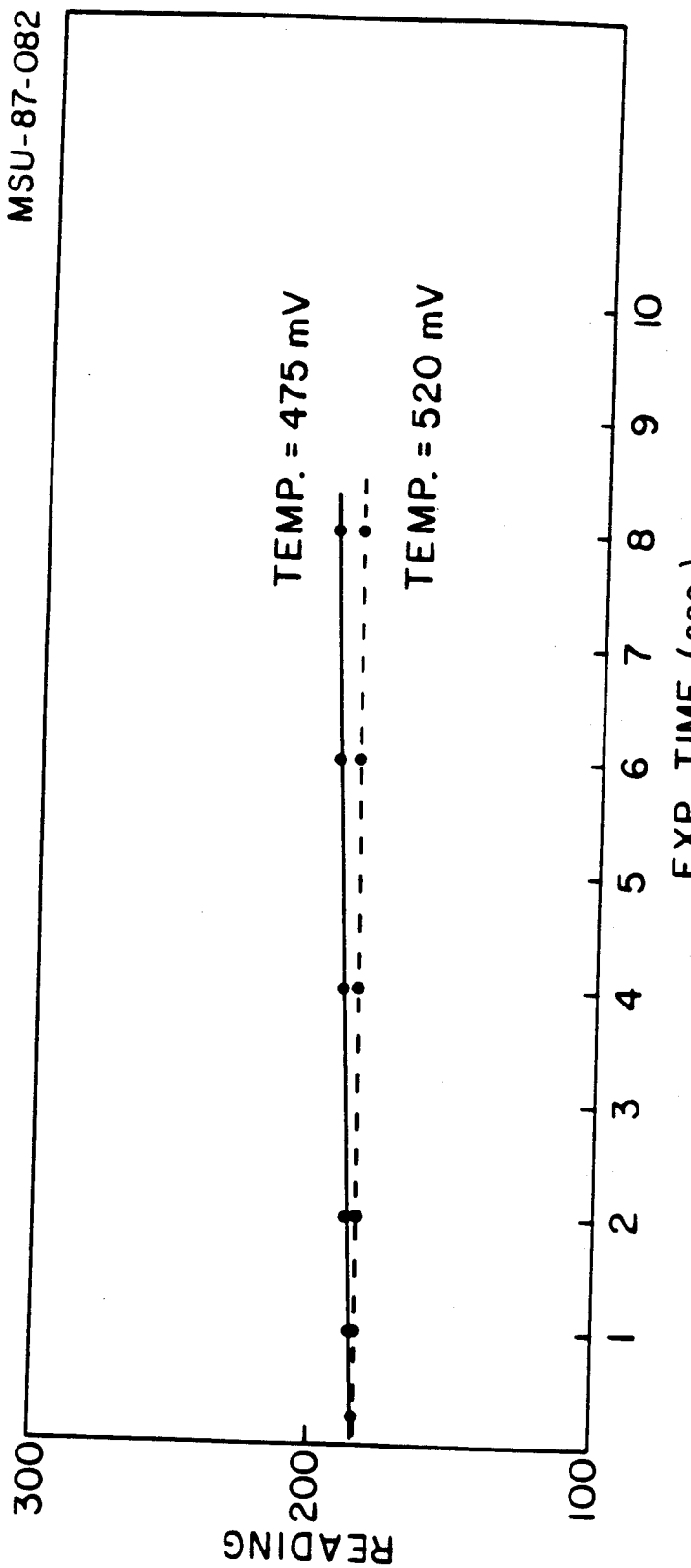

Figure B.2 Dark current vs. exposure time for different temperatures.

device, and which can, in any case, be ignored for our purposes, and the non-uniform response of the pixels to a uniform light source. This is due to differences in sensitivity from one pixel to another.

The background subtracted from each event as a part of the data acquisition process is a readout taken without illumination and allowing the CCD's to integrate in the dark for half a second. This background includes system offset and dark current, but does not correct for the sensitivity variations from pixel to pixel. This can be removed by dividing the exposed field (after subtracting the thermal plus offset background) by a so-called flat field, the picture of a uniformly illuminated surface.

APPENDIX C

Appendix C

STEPS OF THE ANALYSIS OF A CCD-RECORDED NUCLEAR COLLISION

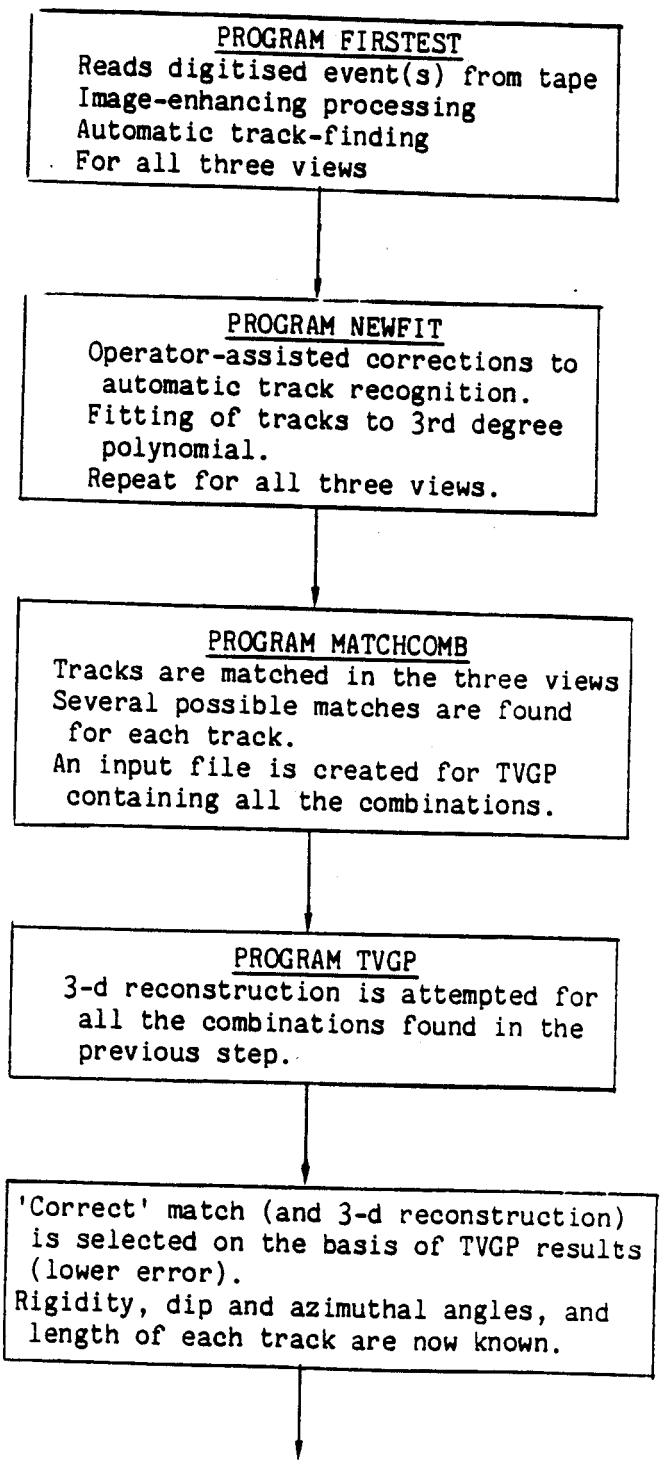

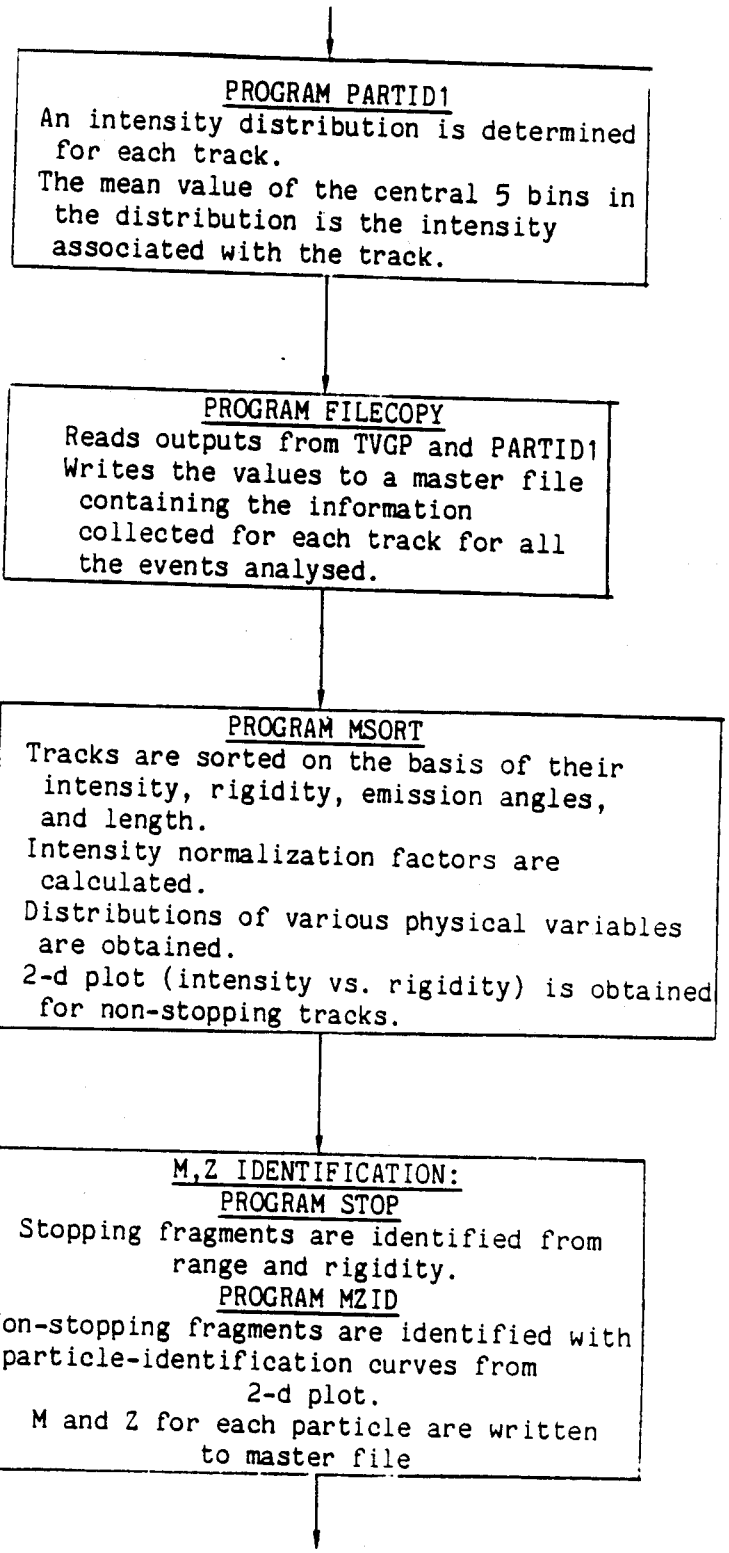
PROGRAM PARTID1
An intensity distribution is determined for each track.
The mean value of the central 5 bins in the distribution is the intensity associated with the track.
PROGRAM FILECOPY
Reads outputs from TVGP and PARTID1
Writes the values to a master file containing the information collected for each track for all the events analysed.
PROGRAM MSORT
Tracks are sorted on the basis of their intensity, rigidity, emission angles, and length.
Intensity normalization factors are calculated.
Distributions of various physical variables are obtained.
2-d plot (intensity vs. rigidity) is obtained for non-stopping tracks.
M,Z IDENTIFICATION:
PROGRAM STOP
Stopping fragments are identified from range and rigidity.
PROGRAM MZID
Non-stopping fragments are identified with particle-identification curves from 2-d plot.
M and Z for each particle are written to master file

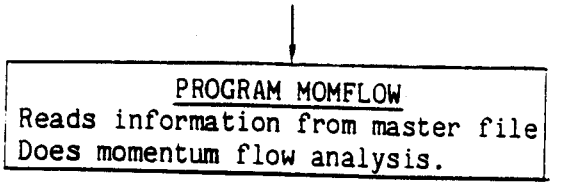
PROGRAM MOMFLOW
Reads information from master file
Does momentum flow analysis.

LIST OF REFERENCES

LIST OF REFERENCES

- A -

Ana 82 N. Anantaraman, H. Stöcker, and G.D. Westfall, Workshop on Phase II Apparatus, NSCL, Dec 82.

- B -

Bab 85 R. Babinet, Ecole Joliot-Curie de Physique Nucleaire, La Matiere Nucleaire dans Tout Ses Etats, 1985.

Bad 82 A. Baden, H.H. Gutbrod, H. Löhner, M.R. Maier, A.M. Poskanzer, T. Renner, H. Riedesel, H.G. Ritter, H. Spieler, A. Warwick, F. Weik, and H. Wieman, Nucl. Instr. and Methods 203 (1982), 189

Bal 84 N.L. Balazs, B. Schürmann, K. Dietrich, and L.P. Csernai, Nucl. Phys. A424 (1984) 605.

Bau 86 A.E. Baumbaugh, K.L. Knickerbocker, B. Baumbaugh, T. Rettig, and R. Ruchti, IEEE Nucl. Science Symposium, 1986.

Bea 83 D. Beavis, S.Y. Chu, S.Y. Fung, W. Gorn, A. Huie, D. Keane, J.J. Lu, R.T. Poe, B.C. Shen, and G. VanDalen, Phys. Rev. C27 (1983) 2443.

Bea 86 D. Beavis, S.Y. Chu, S.Y. Fung, W. Gorn, D. Keane, Y.M. Liu, G. VanDalen, and M. Vient, Phys. Rev. C33 (1986) 1113.

Ber 83 G.F. Bertsch, Nucl. Phys. A400 (1983) 221c.

Bet 79 H.A. Bethe, G.E. Brown, J. Applegate, and J.M. Lattimer, Nucl. Phys. A324, (1979) 487.

Bjo 70 J.D. Bjorken and S.J. Brodsky, Phys. Rev. D1 (1970) 1416.

Bon 86 A. Bonasera and L.P. Csernai, MSUCL-585, 1986

Bon 87 A. Bonasera, L.P. Csernai, and B. Schürmann, MSUCL-601, (1987)

Bon 87a A. Bonasera and A.R. Lampis, MSU Preprint (1987)

Buc 84 G. Buchwald, G. Graebner, J. Theis, J. Maruhn, W. Greiner, and H. Stöcker, Phys. Rev. Lett. 52 (1984) 1594.

- C -

Cse 81 L.P. Csernai and W. Greiner, Phys. Lett. 99B (1981) 85

Cse 82 L.P. Csernai, W. Greiner, H. Stocker, I. Tanihata, S. Nagamiya, and J. Knoll, Phys. Rev. C25 (1982) 2482.

Cse 86 L.P. Csernai, P. Freier, J. Mevissen, H. Nguyen, and L. Waters, Phys. Rev. C34 (1986) 1270.

Cse 86a L. Csernai, Private Communication.

Cug 80 J. Cugnon, Phys. Rev. C22 (1980) 1885.

Cug 81 J. Cugnon, T. Mizutani, and J. Van der Meulen, Nucl. Phys. A352 (1981) 505.

Cug 82 J. Cugnon, D. Kinet, and J. Van der Meulen, Nucl. Phys. A379 (1982) 553

Cug 85 J. Cugnon, Ecole Joliot-Curie de Physique Nucleaire, Proceedings (1985)

Cur 83 M. Curtin, H. Toki, and D.K. Scott, Phys. Lett. 123B (1983) 289.

- D -

Dan 83 P. Danielewicz and M. Gyulassy, Phys. Lett. 129B (1983) 283.

Dan 85 P. Danielewicz and G. Odyniec, Phys. Lett. 157B (1985) 146.

Dea 87 F. Deák, A. Kiss, Z Seres, G. Caskey, A. Galonsky, C.K. Gelbke, B. Remington, M.B. Tsang, and J.J. Kolata, Nucl. Phys. A464 (1987) 133.

Djo 84 S. Djorgovski, Proceedings of the NASA/SDSU Workshop on Improvements in Photometry, eds. W. Borucki and A. Young, San Diego, Ca, 1984.

Dos 86 K.G.R. Doss, H.A. Gustafsson, H.H. Gutbrod, K.H. Kampert, B. Kolb, H. Löhner, B. Ludewigt, A.M. Poskanzer, H.G. Ritter, H.R. Schmidt, and H. Wieman, Phy. Rev. Lett. 57 (1986) 302.

- E -

Ecc 83 M.J. Eccles, M. Elizabeth Sim, and K.P. Tritton, Low Light Level Detectors in Astronomy, Cambridge University Press, 1983.

- F -

Fai 83 G. Fai and J. Randrup, Nucl. Phys. A404 (1983) 551.

Fai 86 G. Fai and J. Randrup, preprint LBL-21573, August 1986.

Fox 87 D. Fox, D.A. Cebra, J. Karn, C. Parks, G.D. Westfall, and W.K. Wilson, to be published in Phys. Rev. C (1987).

Fun 78 S.Y. Fung, W. Gorn, G.P. Kiernan, F.F. Liu, J.J. Lu, Y.T. Oh, J. Ozawa, R.T. Poe, L. Schroeder, and H. Steiner, Phys. Rev. Lett. 40 (1978) 292.

- G -

Gos 77 J. Gosset, H.H. Gutbrod, W.G. Meyer, A.M. Poskanzer, A. Sandoval, R. Stock, and G.D. Westfall, Phys. Rev. C16 (1977) 629.

Gus 84 H.A. Gustafsson, H.H. Gutbrod, B. Kolb, H. Löhner, B. Ludewigt, A.M. Poskanzer, T. Renner, H. Riedesel, H.G. Ritter, A. Warwick, F. Weick, and H. Wieman, Phys. Rev. Lett. 52 (1984) 1590.

Gyu 82 M. Gyulassy, Phys. Rev. Lett. 48 (1982) 454.

- H -

Har 85 J.W. Harris, R. Bock, R. Brockmann, A. Sandoval, R. Stock, H. Ströbele, G. Odyniec, H.G. Pugh, L.S. Schroeder, R.E. Renfordt, D. Schall, D. Bangert, W. Rauch, and K.L. Wolf, Phys. Lett. 153B (1985) 377.

Har 87 J.W. Harris, G. Odyniec, H.G. Pugh, L.S. Schroeder, M.L. Tincknell, W. Rauch, R. Stock, R. Brock, R. Brockmann, A. Sandoval, H. Ströbele, R.E. Renfordt, D. Shall, D. Bangert, J.P. Sullivan, K.L. Wolf, A. Dacal, C. Guerra, and M.E. Ortiz, Phys. Rev. Lett. 58 (1987) 463.

Hui 83 A. Huie, D. Beavis, S.Y. Fung, W. Gorn, D. Keane, J.J. Lu, R.T. Poe, B.C. Shen, and G. VanDalen, Phys. Rev. C27 (1983) 439.

- I -

Igo 53 G.J. Igo, D.D. Clark, and R.M. Eisberg, Phys. Rev. 89 (1953) 879.

Irv 81 J.M. Irvine, Progress in Particle and Nuclear Physics, Vol.6 (1981) p.204, Pergamon Press, Oxford.

- K -

Kea 86 D. Keane, D. Beavis, S.Y. Chu, S.Y. Fung, W. Gorn, Y.M. Liu, G. VanDalen, M. Vient, J.J. Molitoris, and H. Stöcker, Proceedings of the 2nd Conference on the Interactions between Particle and Nuclear Physics, Lake Louise, Alberta, May 1986.

- L -

Lan 58 L.D. Landau and E.M. Lifshitz, Statistical Physics, Pergamon Press, Oxford (1958).

Lu 81 J.J. Lu, D. Beavis, S.Y. Fung, W. Gorn, A. Hiue, G.P. Kierman, R.T. Poe, and G. VanDalen, Phys. Rev. Lett. 46 (1981) 898.

- M -

Mey 80 W.G. Meyer, H.H. Gutbrod, Ch. Lukner, and A. Sandoval, Phys. Rev. C22 (1980) 179.

Mol 85 J.J. Molitoris, D. Hahn, and H. Stocker, Progress in Particle and Nuclear Physics, Vol.15 (1985) p.239, Pergamon Press, Oxford.

Mol 86 J.J. Molitoris, H. Stöcker, H.A. Gustafsson, J. Cugnon, and D. L'Hôte, Phys. Rev. C33 (1986) 867.

- N -

Nag 79 S. Nagamiya, L. Anderson, W. Brückner, O. Chamberlain, M.-C. Lemaire, S. Schnetzer, G. Shapiro, H. Steiner, and I. Tanihata, Phys. Lett. 81B (1979) 147.

- P -

Poc 85 J. Pochodzalla, W.A. Friedman, C.K. Gelbke, K.G. Lynch, M. Maier, D. Ardouin, H. Delagrange, H. Doubre, C. Gregoire, A. Kyanowski, W. Mittig, H. Peghaire, J. Petier, F. Saint-Laurent, Y.P. Viyogi, B. Zwieglinski, G. Bizard, F. Lefebvres, and B. Tamain, MSUCL-518 April 85.

- R -

Ren 84 R.E. Renfordt, D. Schall, R. Bock, R. Brockmann, J.W. Harris, A. Sandoval, R. Stock, H Ströbele, D. Bangert, W. Rauch, G. Odyniec, H.G. Pugh, and L.S. Schroeder, Phys. Rev. Lett. 53 (1984) 763.

Ric 74 P. Rice-Evans, Spark, Streamer, Proportional and Drift Chambers, The Richelieu Press, London 1974

Rit 85 H.G. Ritter, K.G.R. Doss, H.A. Gustafsson, H.H. Gutbrod, K.H. Kampert, B. Kolb, H. Löhner, B. Ludewigt, A.M. Poskanzer, A. Warwick, and H. Wieman, Nucl. Phys. A447 (1985) 3c.

- S -

San 80 A. Sandoval, R. Stock, H.E. Stelzer, R.E. Renfordt, J.W. Harris, J.P. Brannigan, J.V. Geaga, L.J. Rosenberg, L.S. Schroeder, and K.L. Wolf, Phys. Rev. Lett. 45 (1980) 874.

Sch 79 L.S. Schroeder, Nucl. Inst. and Methods 162 (1979) 395.

Sch 81 D.N. Schramm, Progress in Particle and Nuclear Physics, Vol.6 (1981) p.69, Pergamon Press, Oxford.

Seg 64 E. Segre', Nuclei and Particles, W.A. Benjamin, Inc., New York (1964).

Som 66 F.J. Somitz, A.D. Johnson, and T.B. Day, Alvarez Group Programming Note P-117, 2nd ed. (1966).

Sto 82 R. Stock, R. Bock, R. Brockman, J.W. Harris, A. Sandoval, H. Stroebele, K.L. Wolf, H.G. Pugh, L.S. Schroeder, A. Dacal, and M.E. Ortiz, Phys. Rev. Lett. 49 (1982) 1236.

Stö 78 H. Stöcker, W. Greiner, and W. Scheid, Z. Phys. A286 (1978) 121.

Stö 80 H. Stöcker, J.A. Maruhn, and W. Greiner, Phys. Rev. Lett. 44 (1980) 725.

Stö 81 H. Stöcker, A.A. Oglobin, and W. Greiner, Z. Phys. A303 (1981) 259.

Stö 82 H. Stöcker, G. Buchwald, L.P. Csernai, G. Graebner, J.A. Maruhn, and W. Greiner, Nucl. Phys. A387 (1982) 205c.

Str 83 H. Ströbele, R. Brockmann, J.W. Harris, F. Riess, A. Sandoval, R. Stock, K.L. Wolf, H.G. Pugh, L.S. Schroeder, R.E. Renfordt, K. Tittel, and M. Maier, Phys. Rev. C27 (1983) 1349.

Str 84 H. Ströbele, Nucl. Inst. and Methods 221 (1984) 523.

- T -

Tsa 86 M.B. Tsang, R.M. Ronningen, G. Bertsch, Z. Chen, C.B. Chitwood, D.J. Fields, C.K. Gelbke, W.J. Lynch, T. Nayak, J. Pochodzalla, T. Shea, and W. Trautmann, Phys. Rev. Lett. 57 (1986) 559

- V -

Van 82 K. Van Bibber and Andres Sandoval, Streamer Chambers for Heavy Ions, from Heavy Ion Science, Plenum Press, New York, 1982

- W -

Wes 76 G.D. Westfall, J. Gosset, P.J. Johansen, A.M. Poskanzer, W.G. Meyer, H.H. Gutbrod, A. Sandoval, and R. Stock, Phys. Rev. Lett. 37 (1976) 1202.

Wes 85 G.D. Westfall, J.E. Yurkon, J. Van der Plicht, Z.M. Koenig, B.V. Jacak, R. Fox, G.M. Crawley, M.R. Maier, B.E. Hasselquist, R.S. Tickle, D. Horn, Nucl. Instr. and Methods in Phys. Res. A283 (1985), 347.

Wol 81 K.L. Wolf Proceedings of the 5th High-Energy Heavy-Ion Study, LBL, (1981) p.1

- Y -

Yar 79 Y. Yariv and Z. Fränkel, Phys. Rev. C20 (1979) 2227.

Yar 81 Y. Yariv and Z. Fränkel, Phys. Rev. C24 (1981) 488.